Instituto Tecnológico de Costa Rica

Proyecto de investigación

Documento 1

Análisis y diseño de unidades de procesamiento de potencia para sistemas fotovoltaicos

Código de proyecto VIE: 5402-1360-2901

Investigadores participantes: Sergio Morales (coordinador), Carlos Meza, Javier Pérez.

Octubre del 2015

1. Introducción

Con base en el artículo *"6.8 Presentación y evaluación del informe final de proyectos o actividades de fortalecimiento de la investigación y extensión"* de la *"Guía para la gestión interna de la investigación y la extensión en el Instituto Tecnológico de Costa Rica"* cuyo inciso c) establece que *"...se podrán aceptar como alternativos al documento 1 del informe final, otros productos tales como Artículos científicos en proceso de aprobación por una revista indexada o ya publicados"*, se decidió presentar como parte del informe final los siguientes artículos ya publicados:

- Morales, S.; Meza, C. *Herramientas de simulación libres y abiertas para el diseño de unidades de procesamiento de potencia para sistemas fotovoltaicos*, Tecnología en Marcha, Abril-Junio 2015.
- Chavarria, X.; Biel, D. ; Guinjoan, F. ; Meza, C. ; Negroni, J. *Energy-Balance Control of PV Cascaded Multilevel Grid-Connected inverters for Phase-Shifted and Level-Shifted Pulse-Width Modulations*, **IEEE Transaction on Industrial Electronics**, Enero 2013
- Meza, C.; Biel, D. ; Jeltsema, D. ; Scherpen, J.M.A., *Lyapunov-Based Control Scheme for Single-Phase Grid-Connected PV Central Inverters*, **IEEE Transactions on Control Systems Technology**, Marzo 2012

Además, se presenta un documento en desarrollo que, pretender ser utilizado para fines educativos, con modelos matemáticos de los principales UPP utilizados para convertir distintos niveles y formas de onda de corriente continua a niveles y formas de onda deseadas en corriente continua.

Los artículos y documento antes mencionados permiten verificar que se cumplieron con los objetivos del proyecto propuestos, a saber,

- se estudiaron distintas topologías de convertidores de potencia o UPP para sistemas fotovoltaicos,
- se desarrollaron distintas técnicas de controla para convertidores de potencia de sistemas fotovoltaicos,
- se evaluaron y utilizaron distintas herramientas de simulación para analizar el comportamiento dinámico de convertidores de potencia asociados a sistemas fotovoltaicos,
- para obtener los resultados experimentales publicados, se dearrollaron plataformas de hardware con convertidores de potencia.

2. Agradecimientos

Además de los investigadores que participaron en este proyecto contribuyeron también las siguientes personas

- Ing. Jeiner Alvarado (egresado de la carrera de Ing. Electrónica, ITCR),
- Ing. Adrían Gómez (egresado de la carrera de Ing. Electrónica, ITCR),
- Ing. Karla Obando (egresada de la carrera de Ing. Electrónica, ITCR).

3. Anexos

3.1. Modelos matemáticos de unidades de procesamiento de potencia para su control (Documento en desarrollo para fines educativos)

Una unidad de procesamiento de potencia es un elemento de acople de potencia entre dos subsistemas que tiene como fin de establecer una forma o nivel de tensión y corriente deseado en sus terminales de interconexión. Esta función se ilustra en la Figura 1, en donde, para este caso concreto, la unidad de acondicionamiento de potencia debe ser capaz de lograr que las tensiones v_1 y v_2 y las corrientes i_1 e i_2 tengan una forma o nivel deseados.

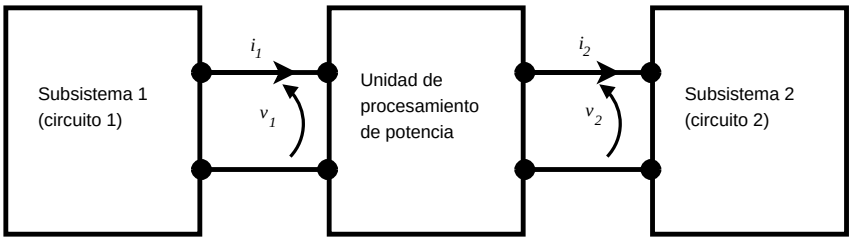

Figura 1: Diagrama de bloques de una unidad de procesamiento de potencia que sirve de acople eléctrico entre dos subcircuitos.

Las unidades de procesamiento de potencia (UPP) más eficientes son aquellas que utilizan dispositivos semiconductores conmutados. Existen numerosas topologías de UPP que difieren en la cantidad y ubicación de los interruptores y los elementos pasivos de almacenamiento de energía (e.g. inductores y condensadores) que contienen.

Es posible obtener un comportamiento dinámico deseado en la UPP por medio de un algoritmo que conmute los interruptores de silicio (e.g. MOSFET) en un momento dado. El punto de partida para el desarrollo de este algoritmo es un modelo matemático válido de la UPP.

En el presente documento se presenta el diagrama y el modelo matemático de las principales topologías de UPP utilizadas para conversión de corriente continua a corriente continua.

3.1.1. Convertidor Reductor o convertidor *"buck"*

En la Fig. 2 se muestra la topología de potencia conocida como *"Convertidor buck"*. Se identificará como P_1. Así mismo, el modelo basado en interruptores ideales se muestra en la Fig. 3.
Por otro lado, considerando $u \in \{0, 1\}$, la ecuación (1) representa el modelo del convertidor

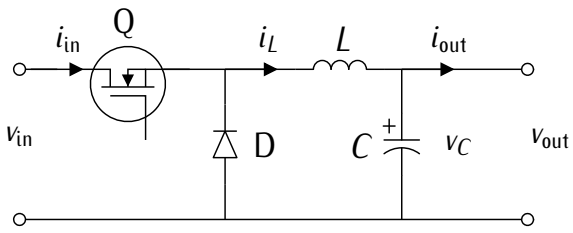

Figura 2: Convertidor tipo *"buck"*

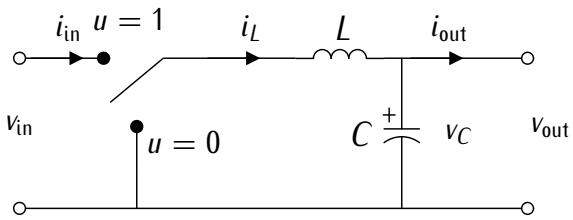

Figura 3: Representación del convertidor tipo *"buck"* mediante interruptores ideales

$$\mathrm{P}_1 : \begin{cases} \dfrac{di_L}{dt} = \dfrac{v_{in} - v_C}{L} \\ \dfrac{dv_C}{dt} = \dfrac{i_L - i_{out}}{C} \end{cases} \quad \text{cuando} \quad u = 1$$
$$\begin{cases} \dfrac{di_L}{dt} = \dfrac{-v_C}{L} \\ \dfrac{dv_C}{dt} = \dfrac{i_L - i_{out}}{C} \end{cases} \quad \text{cuando} \quad u = 0 \tag{1}$$

Generalizando se obtiene

$$\mathrm{P}_1 : \begin{cases} \dfrac{di_L}{dt} = u\dfrac{v_{in}}{L} - \dfrac{v_C}{L} \\ \dfrac{dv_C}{dt} = \dfrac{i_L}{C} - \dfrac{i_{out}}{C} \end{cases} \tag{2}$$

$$x = \begin{bmatrix} x_1 \\ x_2 \end{bmatrix} = \begin{bmatrix} \overline{i_L} \\ \overline{v_C} \end{bmatrix} \tag{3}$$

$$\dot{x} = \begin{bmatrix} 0 & -\frac{1}{L} \\ \frac{1}{C} & 0 \end{bmatrix} x + \begin{bmatrix} 0 \\ \frac{\overline{i_{out}}}{C} \end{bmatrix} + \begin{bmatrix} \frac{\overline{v_{in}}}{L} \\ 0 \end{bmatrix} d \tag{4}$$

Este sistema tiene los siguentes puntos de equilibrio

$$x_1^* = \overline{i_{out}} \tag{5}$$

$$x_2^* = d\,\overline{v_{in}} \tag{6}$$

3.1.2. Convertidor Elevador o convertidor *"boost"*

En la Fig. 4 se muestra la topología de potencia conocida como *"Convertidor boost"*. Se identificará como P_2.

Circuito esquemático

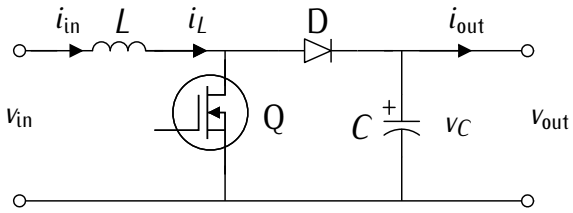

Figura 4: Convertidor tipo *"boost"*

Modelo simplificado

El modelo basado en interruptores ideales se muestra en la Fig. 5.

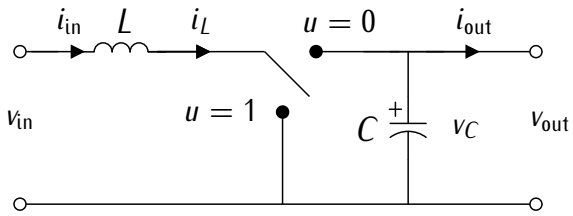

Figura 5: Representación del convertidor tipo *"boost"* mediante interruptores ideales

Modelo promediado

Considerando $u \in \{0, 1\}$, tenemos

$$P_2 : \begin{cases} \dfrac{di_L}{dt} = \dfrac{v_{in}}{L} \\ \dfrac{dv_C}{dt} = \dfrac{-i_{out}}{C} \end{cases} \quad \text{cuando } u = 1$$

$$P_2 : \begin{cases} \dfrac{di_L}{dt} = \dfrac{v_{in} - v_C}{L} \\ \dfrac{dv_C}{dt} = \dfrac{i_L - i_{out}}{C} \end{cases} \quad \text{cuando } u = 0 \tag{7}$$

Generalizando se obtiene

$$P_2 : \begin{cases} \dfrac{di_L}{dt} = \dfrac{v_{in}}{L} - (1-u)\dfrac{v_C}{L} \\ \dfrac{dv_C}{dt} = (1-u)\dfrac{i_L}{C} - \dfrac{i_{out}}{C} \end{cases} \tag{8}$$

$$x = \begin{bmatrix} \bar{i}_L \\ \bar{v}_C \end{bmatrix} \tag{9}$$

$$\dot{x} = \begin{bmatrix} 0 & -\frac{(1-d)}{L} \\ \frac{1-d}{C} & 0 \end{bmatrix} x + \begin{bmatrix} \frac{\overline{v_{in}}}{L} \\ \frac{-i_{out}}{C} \end{bmatrix} \tag{10}$$

Este sistema tiene los siguentes puntos de equilibrio

$$x_1^* = \frac{\overline{i_{out}}}{1-d} \tag{11}$$

$$x_2^* = \frac{\overline{v_{in}}}{1-d} \tag{12}$$

3.1.3. Convertidor Reductor-Elevador o convertidor tipo *"buck-boost"*

En la Fig. 6 se muestra la topología de potencia conocida como *"Convertidor buck-boost"*. Se identificará como P_3. El modelo basado en interruptores ideales para esta topología se muestra en la Fig. 7.

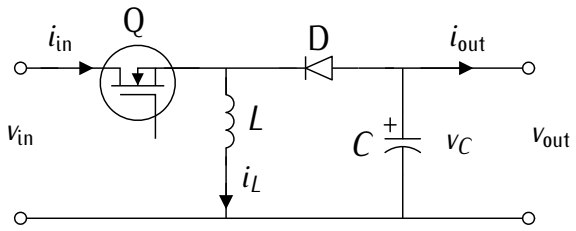

Figura 6: Convertidor tipo *"buck-boost"*

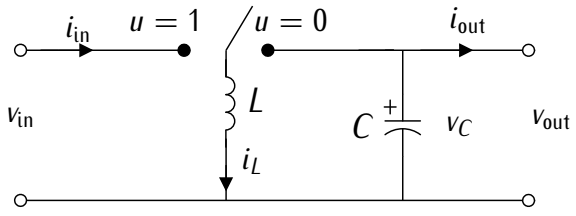

Figura 7: Representación del convertidor tipo *"buck-boost"* mediante interruptores ideales

Modelo promediado

Considerando $u \in \{0, 1\}$, tenemos

$$\mathrm{P}_3 : \begin{cases} \frac{di_L}{dt} = \frac{v_{in}}{L} \\ \frac{dv_C}{dt} = \frac{-i_{out}}{C} \end{cases} \quad \text{cuando } u = 1$$

$$\begin{cases} \frac{di_L}{dt} = \frac{v_C}{L} \\ \frac{dv_C}{dt} = \frac{-i_L - i_{out}}{C} \end{cases} \quad \text{cuando } u = 0 \tag{13}$$

Generalizando se obtiene

$$\mathrm{P}_3 : \begin{cases} \dfrac{di_L}{dt} &= u\dfrac{v_{\text{in}}}{L} + (1-u)\dfrac{v_C}{L} \\ \dfrac{dv_C}{dt} &= -(1-u)\dfrac{i_L}{C} - \dfrac{i_{\text{out}}}{C} \end{cases} \tag{14}$$

$$x = \begin{bmatrix} \bar{i}_L \\ \bar{v}_C \end{bmatrix} \tag{15}$$

$$\dot{x} = \begin{bmatrix} 0 & \frac{(1-d)}{L} \\ -\frac{1-d}{C} & 0 \end{bmatrix} x + \begin{bmatrix} \frac{\overline{v_{\text{in}}}}{L} \\ 0 \end{bmatrix} d + \begin{bmatrix} 0 \\ \frac{-\overline{i_{\text{out}}}}{C} \end{bmatrix} \tag{16}$$

Este sistema tiene los siguentes puntos de equilibrio

$$x_1^* = -\frac{\overline{i_{\text{out}}}}{1-d} \tag{17}$$

$$x_2^* = -d\,\frac{\overline{v_{\text{in}}}}{1-d} \tag{18}$$

3.1.4. Convertidor Reductor-Elevador no inversor o convertidor tipo *"non-inverting buck-boost"*

En la Fig. 8 se muestra la topología de potencia conocida como *"Convertidor buck-boost no inversor"*. Se identificará como P_4.

Circuito esquemático

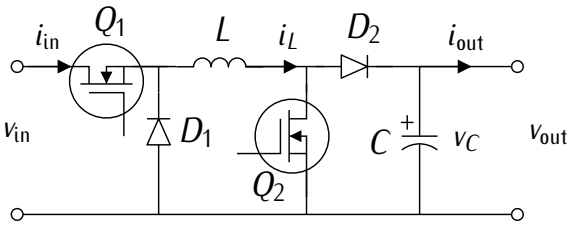

Figura 8: Convertidor tipo *"buck-boost no inversor"*

Modelo simplificado

El modelo basado en interruptores ideales se muestra en la Fig. 9.

Modelo promediado

Considerando $u \in \{0, 1\}$, tenemos

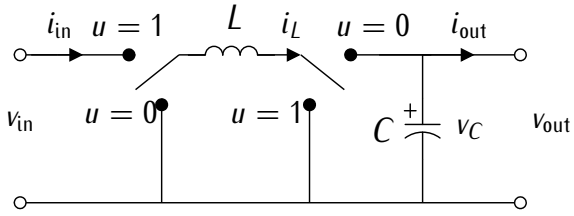

Figura 9: Representación del convertidor tipo *"buck-boost no inversor"* mediante interruptores ideales

$$\mathrm{P}_4 : \begin{cases} \dfrac{di_L}{dt} = \dfrac{v_{in}}{L} \\ \dfrac{dv_C}{dt} = \dfrac{-i_{out}}{C} \end{cases} \text{cuando } u = 1 \qquad \begin{cases} \dfrac{di_L}{dt} = -\dfrac{v_C}{L} \\ \dfrac{dv_C}{dt} = \dfrac{i_L - i_{out}}{C} \end{cases} \text{cuando } u = 0 \tag{19}$$

Generalizando se obtiene

$$\mathrm{P}_4 : \begin{cases} \dfrac{di_L}{dt} = u\dfrac{v_{in}}{L} - (1-u)\dfrac{v_C}{L} \\ \dfrac{dv_C}{dt} = (1-u)\dfrac{i_L}{C} - \dfrac{i_{out}}{C} \end{cases} \tag{20}$$

$$x = \begin{bmatrix} \bar{i}_L \\ \bar{v}_C \end{bmatrix} \tag{21}$$

$$\dot{x} = \begin{bmatrix} 0 & -\frac{(1-d)}{L} \\ \frac{1-d}{C} & 0 \end{bmatrix} x + \begin{bmatrix} \frac{\overline{v_{in}}}{L} \\ 0 \end{bmatrix} d + \begin{bmatrix} 0 \\ -\frac{\overline{i_{out}}}{C} \end{bmatrix} \tag{22}$$

Este sistema tiene los siguentes puntos de equilibrio

$$x_1^* = \frac{\overline{i_{out}}}{1-d} \tag{23}$$

$$x_2^* = d\,\frac{\overline{v_{in}}}{1-d} \tag{24}$$

3.1.5. Convertidor *"Ćuk"*

En la Fig. 10 se muestra la topología de potencia conocida como *"Convertidor Ćuk"*. Se identificará como P_5.

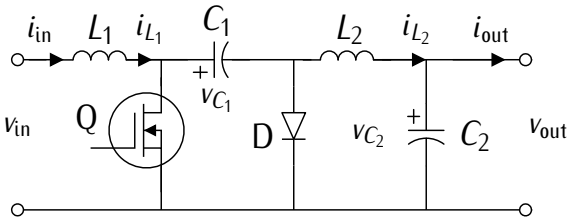

Figura 10: Convertidor tipo *"Ćuk"*

Circuito esquemático

Modelo simplificado

El modelo basado en interruptores ideales se muestra en la Fig. 11.

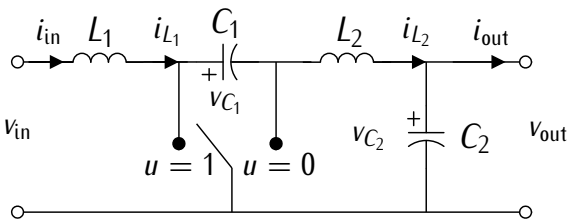

Figura 11: Representación del convertidor tipo *"Ćuk"* mediante interruptores ideales

Modelo promediado

Considerando $u \in \{0, 1\}$, tenemos

$$
\mathrm{P}_5 : \begin{cases}
\dfrac{di_{L_1}}{dt} = \dfrac{v_{in}}{L_1} & \\
\dfrac{di_{L_2}}{dt} = \dfrac{-v_{C_1} - v_{C_2}}{L_2} & \text{cuando } u = 1 \\
\dfrac{dv_{C_1}}{dt} = \dfrac{i_{L_2}}{C_1} & \\
\dfrac{dv_{C_2}}{dt} = \dfrac{i_{L_2} - i_{out}}{C_2} & \\
\dfrac{di_{L_1}}{dt} = \dfrac{v_{in} - v_{C_1}}{L_1} & \\
\dfrac{di_{L_2}}{dt} = \dfrac{-v_{C_2}}{L_2} & \text{cuando } u = 0 \\
\dfrac{dv_{C_1}}{dt} = \dfrac{i_{L_1}}{C_1} & \\
\dfrac{dv_{C_2}}{dt} = \dfrac{i_{L_2} - i_{out}}{C_2} &
\end{cases} \tag{25}
$$

Generalizando se obtiene

$$\mathrm{P}_5 : \begin{cases} \frac{di_{L_1}}{dt} &= \frac{v_{\text{in}}}{L_1} - (1-u)\frac{v_{C_1}}{L_1} \\ \frac{di_{L_2}}{dt} &= -u\frac{v_{C_1}}{L_2} - \frac{v_{C_2}}{L_2} \\ \frac{dv_{C_1}}{dt} &= (1-u)\frac{i_{L_1}}{C_1} + d\frac{i_{L_2}}{C_1} \\ \frac{dv_{C_2}}{dt} &= \frac{i_{L_2}}{C_2} - \frac{i_{\text{out}}}{C_2} \end{cases} \tag{26}$$

$$x = \begin{bmatrix} \bar{i}_{L_1} \\ \bar{i}_{L_2} \\ \bar{v}_{C_1} \\ \bar{v}_{C_2} \end{bmatrix} \tag{27}$$

$$\dot{x} = \begin{bmatrix} 0 & 0 & -\frac{(1-d)}{L_1} & 0 \\ 0 & 0 & -d & \frac{-1}{L_2} \\ \frac{(1-d)}{C_1} & \frac{d}{C_1} & 0 & 0 \\ 0 & \frac{1}{C_2} & 0 & 0 \end{bmatrix} x + \begin{bmatrix} \frac{\overline{v_{\text{in}}}}{L_1} \\ 0 \\ 0 \\ \frac{-\overline{i_{\text{out}}}}{C_2} \end{bmatrix} \tag{28}$$

Este sistema tiene los siguentes puntos de equilibrio

$$x_1^* = \frac{-d\,\overline{i_{\text{out}}}}{1-d} \tag{29}$$

$$x_2^* = \overline{i_{\text{out}}} \tag{30}$$

$$x_3^* = \frac{\overline{v_{\text{in}}}}{1-d} \tag{31}$$

$$x_4^* = d\,\frac{\overline{v_{\text{in}}}}{1-d} \tag{32}$$

3.1.6. Convertidor *"Sepic"*

En la Fig. 12 se muestra la topología de potencia conocida como *"Convertidor Sepic"*. Se identificará como P_6. Así mismo, en la Fig. 13 se muestra el modelo basado en interruptores ideales.

Considerando $u \in \{0, 1\}$ se puede derivar el modelo matemático de esta topología, tal y como se indica en la ecuación (33).

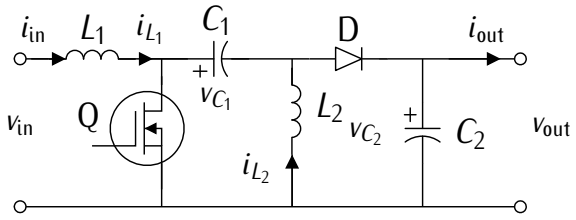

Figura 12: Convertidor tipo *"Sepic"*

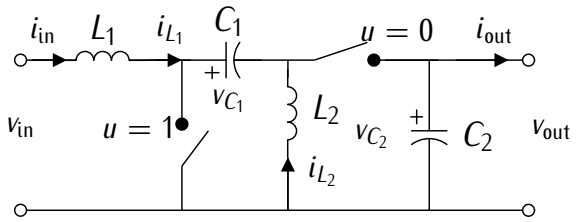

Figura 13: Representación del convertidor tipo *"Sepic"* mediante interruptores ideales

$$
\mathrm{P}_6 : \begin{cases}
\dfrac{di_{L_1}}{dt} = \dfrac{v_{in}}{L_1} & \\
\dfrac{di_{L_2}}{dt} = \dfrac{v_{C_1}}{L_2} & \\
\dfrac{dv_{C_1}}{dt} = \dfrac{-i_{L_2}}{C_1} & \text{cuando } u = 1 \\
\dfrac{dv_{C_2}}{dt} = \dfrac{-i_{out}}{C_2} & \\
\dfrac{di_{L_1}}{dt} = \dfrac{v_{in} - v_{C_1} - v_{C_2}}{L_1} & \\
\dfrac{di_{L_2}}{dt} = \dfrac{-v_{C_2}}{L_2} & \\
\dfrac{dv_{C_1}}{dt} = \dfrac{i_{L_1}}{C_1} & \text{cuando } u = 0 \\
\dfrac{dv_{C_2}}{dt} = \dfrac{i_{L_1} + i_{L_2} - i_{out}}{C_2} &
\end{cases} \tag{33}
$$

Generalizando se obtiene

$$
\mathrm{P}_6 : \begin{cases}
\dfrac{di_{L_1}}{dt} = \dfrac{v_{in}}{L_1} - (1-u)\dfrac{v_{C_1} + v_{C_2}}{L_1} \\
\dfrac{di_{L_2}}{dt} = u\dfrac{v_{C_1}}{L_2} - (1-u)\dfrac{v_{C_2}}{L_2} \\
\dfrac{dv_{C_1}}{dt} = -u\dfrac{i_{L_2}}{C_1} + (1-d)\dfrac{i_{L_1}}{C_1} \\
\dfrac{dv_{C_2}}{dt} = (1-u)\dfrac{i_{L_1} + i_{L_2}}{C_2} - \dfrac{i_{out}}{C_2}
\end{cases} \tag{34}
$$

$$x = \begin{bmatrix} \bar{i}_{L_1} \\ \bar{i}_{L_2} \\ \bar{v}_{C_1} \\ \bar{v}_{C_2} \end{bmatrix} \tag{35}$$

$$\dot{x} = \begin{bmatrix} 0 & 0 & -\frac{(1-d)}{L_1} & -\frac{(1-d)}{L_1} \\ 0 & 0 & \frac{d}{L_2} & -\frac{(1-d)}{L_2} \\ \frac{(1-d)}{C_1} & \frac{-d}{C_1} & 0 & 0 \\ \frac{(1-d)}{C_2} & \frac{(1-d)}{C_2} & 0 & 0 \end{bmatrix} x + \begin{bmatrix} \frac{\overline{v_{in}}}{L_1} \\ 0 \\ 0 \\ \frac{-\overline{i_{out}}}{C_2} \end{bmatrix} \tag{36}$$

Este sistema tiene los siguentes puntos de equilibrio

$$x_1^* = \frac{d\,\overline{i_{out}}}{1-d} \tag{37}$$

$$x_2^* = \overline{i_{out}} \tag{38}$$

$$x_3^* = \overline{v_{in}} \tag{39}$$

$$x_4^* = d\,\frac{\overline{v_{in}}}{1-d} \tag{40}$$

3.1.7. Convertidor *zeta*

En la Fig. 14 se muestra la topología de potencia conocida como *"Convertidor zeta"*. Se identificará como P_7.

Circuito esquemático

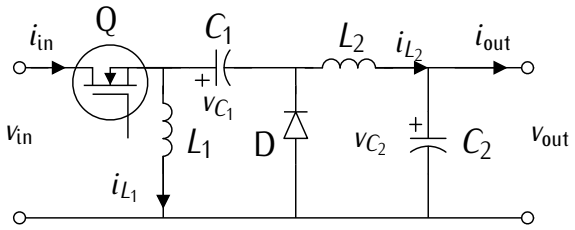

Figura 14: Convertidor tipo *"zeta"*

Modelo simplificado

El modelo basado en interruptores ideales se muestra en la Fig. 15.

Modelo promediado

Considerando $u \in \{0, 1\}$, tenemos

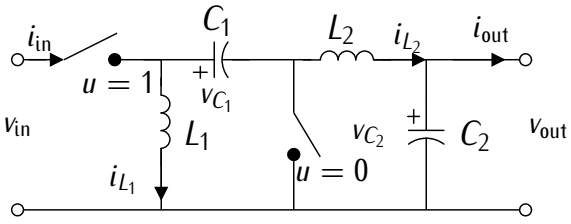

Figura 15: Representación del convertidor tipo *"zeta"* mediante interruptores ideales

$$
\mathrm{P}_7 : \begin{cases}
\dfrac{di_{L_1}}{dt} = \dfrac{v_{in}}{L_1} & \\
\dfrac{di_{L_2}}{dt} = \dfrac{v_{in} - v_{C_1} - v_{C_2}}{L_2} & \text{cuando } u = 1 \\
\dfrac{dv_{C_1}}{dt} = \dfrac{i_{L_2}}{C_1} & \\
\dfrac{dv_{C_2}}{dt} = \dfrac{i_{L_2} - i_{out}}{C_2} & \\
\dfrac{di_{L_1}}{dt} = \dfrac{v_{C_1}}{L_1} & \\
\dfrac{di_{L_2}}{dt} = \dfrac{-v_{C_2}}{L_2} & \text{cuando } u = 0 \\
\dfrac{dv_{C_1}}{dt} = \dfrac{-i_{L_1}}{C_1} & \\
\dfrac{dv_{C_2}}{dt} = \dfrac{i_{L_2} - i_{out}}{C_2} &
\end{cases} \tag{41}
$$

Generalizando se obtiene

$$
\mathrm{P}_7 : \begin{cases}
\dfrac{di_{L_1}}{dt} = u\dfrac{v_{in}}{L_1} + (1-u)\dfrac{v_{C_1}}{L_1} \\
\dfrac{di_{L_2}}{dt} = u\dfrac{v_{in} - v_{C_1}}{L_2} - \dfrac{v_{C_2}}{L_2} \\
\dfrac{dv_{C_1}}{dt} = u\dfrac{i_{L_2}}{C_1} - (1-d)\dfrac{i_{L_1}}{C_1} \\
\dfrac{dv_{C_2}}{dt} = \dfrac{i_{L_2} - i_{out}}{C_2}
\end{cases} \tag{42}
$$

$$
x = \begin{bmatrix} \bar{i}_{L_1} \\ \bar{i}_{L_2} \\ \bar{v}_{C_1} \\ \bar{v}_{C_2} \end{bmatrix} \tag{43}
$$

$$\dot{x} = \begin{bmatrix} 0 & 0 & \frac{(1-d)}{L_1} & 0 \\ 0 & 0 & -\frac{d}{L_2} & -\frac{1}{L_2} \\ -\frac{(1-d)}{C_1} & \frac{d}{C_1} & 0 & 0 \\ 0 & \frac{1}{C_2} & 0 & 0 \end{bmatrix} x + \begin{bmatrix} \frac{\overline{v_{in}}}{L_1} \\ \frac{\overline{v_{in}}}{L_2} \\ 0 \\ 0 \end{bmatrix} d + \begin{bmatrix} 0 \\ 0 \\ 0 \\ \frac{-\overline{i_{out}}}{C_2} \end{bmatrix} \tag{44}$$

Este sistema tiene los siguentes puntos de equilibrio

$$x_1^* = \frac{d\,\overline{i_{out}}}{1-d} \tag{45}$$

$$x_2^* = \overline{i_{out}} \tag{46}$$

$$x_3^* = \frac{d\,\overline{v_{in}}}{(1-d)} \tag{47}$$

$$x_4^* = -d^2\frac{\overline{v_{in}}}{1-d} \tag{48}$$

3.1.8. Convertidor Cuádruple Reductor o convertidor tipo *"Quad-buck"*

En la Fig. 16 se muestra la topología de potencia conocida como *"Convertidor Quad-buck"*. Se identificará como P_8.

Circuito esquemático

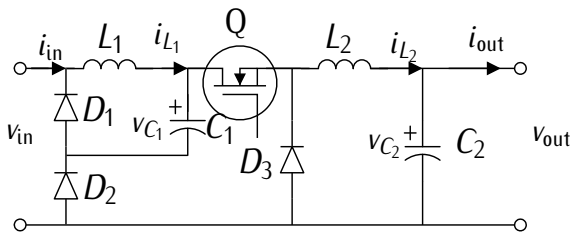

Figura 16: Convertidor tipo *"Quad-buck"*

Modelo simplificado

El modelo basado en interruptores ideales se muestra en la Fig. 17.

Modelo promediado

Considerando $u \in \{0, 1\}$, tenemos

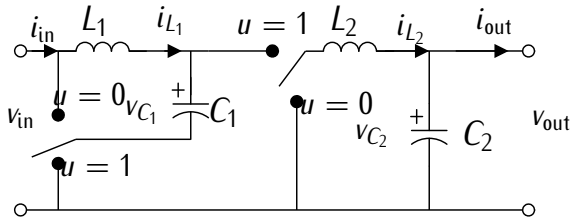

Figura 17: Representación del convertidor tipo *"Quad-buck"* mediante interruptores ideales

$$
\mathrm{P}_8 : \begin{cases}
\dfrac{di_{L_1}}{dt} = \dfrac{v_{in} - v_{C_1}}{L_1} \\
\dfrac{di_{L_2}}{dt} = \dfrac{v_{C_1} - v_{C_2}}{L_2} \\
\dfrac{dv_{C_1}}{dt} = \dfrac{i_{L_1} - i_{L_2}}{C_1} \\
\dfrac{dv_{C_2}}{dt} = \dfrac{i_{L_2} - i_{out}}{C_2}
\end{cases} \quad \text{cuando} \quad u = 1
$$

$$
\begin{cases}
\dfrac{di_{L_1}}{dt} = \dfrac{-v_{C_1}}{L_1} \\
\dfrac{di_{L_2}}{dt} = \dfrac{-v_{C_2}}{L_2} \\
\dfrac{dv_{C_1}}{dt} = \dfrac{i_{L_1}}{C_1} \\
\dfrac{dv_{C_2}}{dt} = \dfrac{i_{L_2} - i_{out}}{C_2}
\end{cases} \quad \text{cuando} \quad u = 0 \tag{49}
$$

Generalizando se obtiene

$$
\mathrm{P}_8 : \begin{cases}
\dfrac{di_{L_1}}{dt} = u\dfrac{v_{in}}{L_1} - \dfrac{v_{C_1}}{L_1} \\
\dfrac{di_{L_2}}{dt} = u\dfrac{v_{C_1}}{L_2} - \dfrac{v_{C_2}}{L_2} \\
\dfrac{dv_{C_1}}{dt} = -u\dfrac{i_{L_2}}{C_1} + \dfrac{i_{L_1}}{C_1} \\
\dfrac{dv_{C_2}}{dt} = \dfrac{i_{L_2} - i_{out}}{C_2}
\end{cases} \tag{50}
$$

$$
x = \begin{bmatrix} \bar{i}_{L_1} \\ \bar{i}_{L_2} \\ \bar{v}_{C_1} \\ \bar{v}_{C_2} \end{bmatrix} \tag{51}
$$

$$\dot{x} = \begin{bmatrix} 0 & 0 & \frac{-1}{L_1} & 0 \\ 0 & 0 & \frac{d}{L_2} & \frac{-1}{L_2} \\ \frac{1}{C_1} & \frac{-d}{C_1} & 0 & 0 \\ 0 & \frac{1}{C_2} & 0 & 0 \end{bmatrix} x + \begin{bmatrix} \frac{\overline{v_{in}}}{L_1} \\ 0 \\ 0 \\ 0 \end{bmatrix} d + \begin{bmatrix} 0 \\ 0 \\ 0 \\ \frac{-\overline{i_{out}}}{C_2} \end{bmatrix} \tag{52}$$

Este sistema tiene los siguentes puntos de equilibrio

$$x_1^* = d\,\overline{i_{out}} \tag{53}$$

$$x_2^* = \overline{i_{out}} \tag{54}$$

$$x_3^* = d\,\overline{v_{in}} \tag{55}$$

$$x_4^* = -d^2\overline{v_{in}} \tag{56}$$

3.1.9. Convertidor Elevador-Elevador o convertidor tipo *"Boost-boost"*

En la Fig. 18 se muestra la topología de potencia conocida como *"Convertidor Boost-boost"*. Se identificará como P_9.

Circuito esquemático

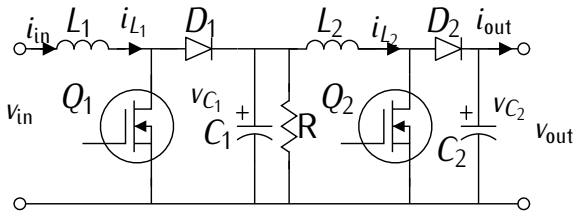

Figura 18: Convertidor tipo *"Boost-boost"*

Modelo simplificado

El modelo basado en interruptores ideales se muestra en la Fig. 19.

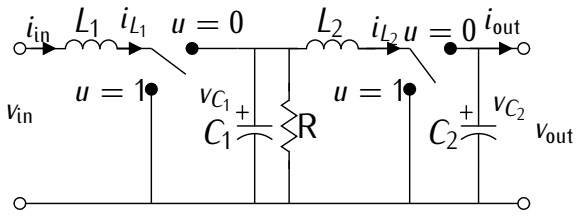

Figura 19: Representación del convertidor tipo *"Boost-boost"* mediante interruptores ideales

Modelo promediado

Considerando $u \in \{0, 1\}$, tenemos

$$\mathrm{P}_9 : \begin{cases} \dfrac{di_{L_1}}{dt} = \dfrac{v_{\text{in}}}{L_1} \\ \dfrac{di_{L_2}}{dt} = \dfrac{v_{C_1}}{L_2} \\ \dfrac{dv_{C_1}}{dt} = \dfrac{-i_{L_2}}{C_1} - \dfrac{v_{C_1}}{RC_1} \\ \dfrac{dv_{C_2}}{dt} = \dfrac{-i_{\text{out}}}{C_2} \end{cases} \text{cuando } u = 1 \qquad \begin{cases} \dfrac{di_{L_1}}{dt} = \dfrac{v_{\text{in}} - v_{C_1}}{L_1} \\ \dfrac{di_{L_2}}{dt} = \dfrac{v_{C_1} - v_{C_2}}{L_2} \\ \dfrac{dv_{C_1}}{dt} = \dfrac{i_{L_1} - i_{L_2}}{C_1} - \dfrac{v_{C_1}}{RC_1} \\ \dfrac{dv_{C_2}}{dt} = \dfrac{i_{L_2} - i_{\text{out}}}{C_2} \end{cases} \text{cuando } u = 0 \tag{57}$$

Generalizando se obtiene

$$\mathrm{P}_9 : \begin{cases} \dfrac{di_{L_1}}{dt} = \dfrac{v_{\text{in}}}{L_1} - (1-u)\dfrac{v_{C_1}}{L_1} \\ \dfrac{di_{L_2}}{dt} = \dfrac{v_{C_1}}{L_2} - (1-u)\dfrac{v_{C_2}}{L_2} \\ \dfrac{dv_{C_1}}{dt} = (1-u)\dfrac{i_{L_1}}{C_1} - \dfrac{i_{L_2}}{C_1} - \dfrac{v_{C_1}}{RC_1} \\ \dfrac{dv_{C_2}}{dt} = (1-u)\dfrac{i_{L_2}}{C_2} - \dfrac{i_{\text{out}}}{C_2} \end{cases} \tag{58}$$

$$x = \begin{bmatrix} \bar{i}_{L_1} \\ \bar{i}_{L_2} \\ \bar{v}_{C_1} \\ \bar{v}_{C_2} \end{bmatrix} \tag{59}$$

$$\dot{x} = \begin{bmatrix} 0 & 0 & \frac{-(1-d)}{L_1} & 0 \\ 0 & 0 & \frac{1}{L_2} & \frac{-(1-d)}{L_2} \\ \frac{(1-d)}{C_1} & \frac{-1}{C_1} & \frac{-1}{RC_1} & 0 \\ 0 & \frac{(1-d)}{C_2} & 0 & 0 \end{bmatrix} x + \begin{bmatrix} \frac{\overline{v_{\text{in}}}}{L_1} \\ 0 \\ 0 \\ \frac{-\overline{i_{\text{out}}}}{C_2} \end{bmatrix} \tag{60}$$

Este sistema tiene los siguentes puntos de equilibrio

$$x_1^* = \frac{\overline{v_{\text{in}}}}{R(1-d)^2} + \frac{\overline{i_{\text{out}}}}{(1-d)^2} \tag{61}$$

$$x_2^* = \frac{\overline{i_{\text{out}}}}{(1-d)} \tag{62}$$

$$x_3^* = \frac{\overline{v_{\text{in}}}}{(1-d)} \tag{63}$$

$$x_4^* = \frac{\overline{v_{\text{in}}}}{(1-d)^2} \tag{64}$$

3.1.10. Convertidor Doble Reductor-Elevador o convertidor tipo *"Double buck-boost"*

En la Fig. 20 se muestra la topología de potencia conocida como *"Convertidor Double buck-boost"*. Se identificará como P_{10}.

Circuito esquemático

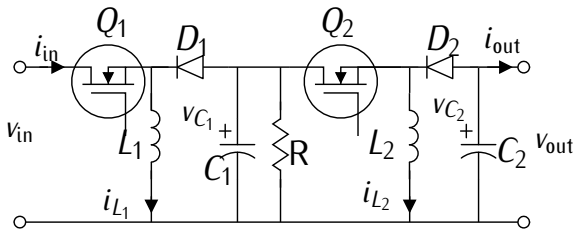

Figura 20: Convertidor tipo *"Double buck-boost"*

Modelo simplificado

El modelo basado en interruptores ideales se muestra en la Fig. 21.

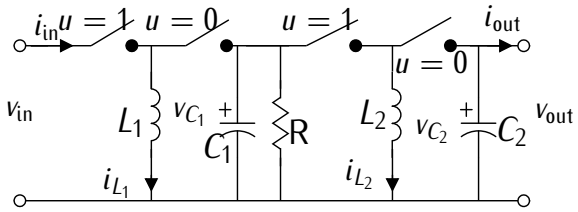

Figura 21: Representación del convertidor tipo *"Double buck-boost"* mediante interruptores ideales

Modelo promediado

Considerando $u \in \{0, 1\}$, tenemos

$$
\mathrm{P}_{10}:\begin{cases}
\dfrac{di_{L_1}}{dt} &= \dfrac{v_{\text{in}}}{L_1} \\
\dfrac{di_{L_2}}{dt} &= \dfrac{v_{C_1}}{L_2} \\
\dfrac{dv_{C_1}}{dt} &= \dfrac{-i_{L_2}}{C_1} - \dfrac{v_{C_1}}{RC_1} \\
\dfrac{dv_{C_2}}{dt} &= \dfrac{-i_{\text{out}}}{C_2}
\end{cases} \quad \text{cuando} \quad u = 1
$$

$$
\mathrm{P}_{10}:\begin{cases}
\dfrac{di_{L_1}}{dt} &= \dfrac{v_{C_1}}{L_1} \\
\dfrac{di_{L_2}}{dt} &= \dfrac{v_{C_2}}{L_2} \\
\dfrac{dv_{C_1}}{dt} &= \dfrac{-i_{L_1}}{C_1} - \dfrac{v_{C_1}}{RC_1} \\
\dfrac{dv_{C_2}}{dt} &= \dfrac{-i_{L_2} - i_{\text{out}}}{C_2}
\end{cases} \quad \text{cuando} \quad u = 0 \tag{65}
$$

Generalizando se obtiene

$$
\mathrm{P}_{10}:\begin{cases}
\dfrac{di_{L_1}}{dt} &= u\dfrac{v_{\text{in}}}{L_1} + (1-u)\dfrac{v_{C_1}}{L_1} \\
\dfrac{di_{L_2}}{dt} &= u\dfrac{v_{C_1}}{L_2} + (1-u)\dfrac{v_{C_2}}{L_2} \\
\dfrac{dv_{C_1}}{dt} &= -(1-u)\dfrac{i_{L_1}}{C_1} - u\dfrac{i_{L_2}}{C_1} - \dfrac{v_{C_1}}{RC_1} \\
\dfrac{dv_{C_2}}{dt} &= -(1-u)\dfrac{i_{L_2}}{C_2} - \dfrac{i_{\text{out}}}{C_2}
\end{cases} \tag{66}
$$

$$
x = \begin{bmatrix} \bar{i}_{L_1} \\ \bar{i}_{L_2} \\ \bar{v}_{C_1} \\ \bar{v}_{C_2} \end{bmatrix} \tag{67}
$$

$$
\dot{x} = \begin{bmatrix}
0 & 0 & \frac{(1-d)}{L_1} & 0 \\
0 & 0 & \frac{d}{L_2} & \frac{(1-d)}{L_2} \\
\frac{-(1-d)}{C_1} & \frac{-d}{C_1} & \frac{-1}{RC_1} & 0 \\
0 & \frac{-(1-d)}{C_2} & 0 & 0
\end{bmatrix} x + \begin{bmatrix} \frac{\overline{v_{\text{in}}}}{L_1} \\ 0 \\ 0 \\ 0 \end{bmatrix} d + \begin{bmatrix} 0 \\ 0 \\ 0 \\ \frac{-\overline{i_{\text{out}}}}{C_2} \end{bmatrix} \tag{68}
$$

Este sistema tiene los siguentes puntos de equilibrio

$$
x_1^* = \frac{d\,\overline{v_{\text{in}}}}{R\,(1-d)^2} + \frac{\overline{i_{\text{out}}}}{(1-d)^2} \tag{69}
$$

$$
x_2^* = \frac{-\overline{i_{\text{out}}}}{(1-d)} \tag{70}
$$

$$x_3^* = \frac{-d\,\overline{v_{in}}}{(1-d)} \tag{71}$$

$$x_4^* = \frac{d^2\overline{v_{in}}}{(1-d)^2} \tag{72}$$

Herramientas de simulación libres y abiertas para el diseño de unidades de procesamiento de potencia para sistemas fotovoltaicos

Free and open source simulation tools for the design of power processing units for photovoltaic systems

Sergio Morales-Hernández[1], Carlos Meza-Benavides[2]

Fecha de recepción: 18 de setiembre del 2014
Fecha de aprobación: 10 de diciembre del 2014

Morales-Hernández, S; Meza-Benavides, C. Herramientas de simulación libres y abiertas para el diseño de unidades de procesamiento de potencia para sistemas fotovoltaicos. *Tecnología en Marcha*. Vol. 28, Nº 2, Abril-Junio. Pág 44-60.

1 Profesor Adjunto, Escuela de Ingeniería en Electrónica, Instituto Tecnológico de Costa Rica
Correo electrónico: smorales@itcr.ac.cr
2 Profesor Adjunto, Escuela de Ingeniería en Electrónica, Instituto Tecnológico de Costa Rica
Correo electrónico: cmeza@itcr.ac.cr

Palabras clave

Sistemas fotovoltaicos; herramientas de simulación; convertidores de potencia.

Resumen

Las fuentes de energía renovable, entre ellas la solar fotovoltaica, requieren de circuitos electrónicos que sirvan de interface entre el dispositivo transductor y el dispositivo o sistema que utilizará la energía. Más aún, la eficiencia energética y el costo del sistema se pueden ver comprometidos si este circuito electrónico no ha sido diseñado de forma apropiada. Dado que, por un lado, las características eléctricas de los dispositivos fotovoltaicos son no lineales y, por otro, los circuitos electrónicos más eficientes son naturalmente discontinuos, se requiere un análisis dinámico detallado que permita optimizar el diseño. Dicho análisis debe ser apoyado por herramientas informáticas de simulación. En este artículo se hace una comparación entre dos herramientas informáticas de simulación de sistemas dinámicos para determinar su utilidad en el proceso de diseño de sistemas fotovoltaicos, principalmente en lo que corresponde a las unidades de procesamiento de potencia. Utilizando como caso de estudio un sistema fotovoltaico para la carga de una batería, se determinó que la herramienta Scicoslab facilita la simulación de sistemas dinámicos complejos, presentes en las unidades de procesamiento de potencia de los sistemas fotovoltaicos.

Keywords

Photovoltaic systems; simulation tools; power converters.

Abstract

Renewable energy sources, including solar photovoltaic, require electronic circuits that serve as interface between the transducer device and the device or system that uses energy. Moreover, the energy efficiency and the cost of the system can be compromised if such electronic circuit is not designed properly. Given that the electrical characteristics of the photovoltaic devices are nonlinear and that the most efficient electronic circuits for power processing are naturally discontinuous, a detailed dynamic analysis to optimize the design is required. This analysis should be supported by computer simulation tools. In this paper a comparison between two software tools for dynamic system simulation is performed to determinate its usefulness in the design process of photovoltaic systems, mainly in what corresponds to the power processing units. Using as a case of study a photovoltaic system for battery charging it was determined that Scicoslab tool was the most suitable.

Introducción

La energía solar es abundante y el proceso de conversión a energía eléctrica puede llegar a tener un impacto ambiental muy bajo. Los sistemas solares fotovoltaicos permiten el aprovechamiento de la radiación electromagnética producida por el sol por medios eléctricos. La tecnología fotovoltaica es hoy en día bastante madura y en muchas regiones del mundo su costo es comparable con el de las fuentes de energía tradicional.

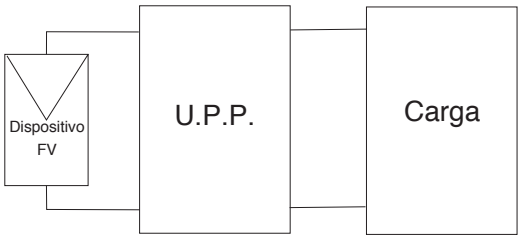

Figura 1. Diagrama de bloques representativo de un sistema fotovoltaico (U.P.P.: Unidad de Procesamiento de Potencia).

Un sistema fotovoltaico está conformado por uno o varios dispositivos fotovoltaicos (celda, panel o conjunto de paneles) y una unidad de procesamiento de potencia (ver figura 1). Las características eléctricas de un dispositivo fotovoltaico hacen necesario el uso de un circuito electrónico, denominado unidad de procesamiento de potencia (UPP), para aprovechar de forma óptima la energía que éste genera. Sin la UPP, el dispositivo fotovoltaico generaría menos energía de la que potencialmente puede producir. Esto se debe a que un dispositivo fotovoltaico presenta un punto de máxima generación de potencia definido por un par de valores de tensión y corriente determinados, tal y como se puede apreciar en la figura 2. Una de las tareas de la UPP es posicionar en todo momento el punto de operación del dispositivo fotovoltaico en su punto de máxima potencia. La otra tarea de la unidad de procesado de potencia es lograr que la carga que está siendo alimentada por el dispositivo fotovoltaico reciba un nivel de tensión y corriente adecuado (ver figura 1). Cargas típicas en sistemas fotovoltaicos son baterías, motores, luminarias o la misma red eléctrica.

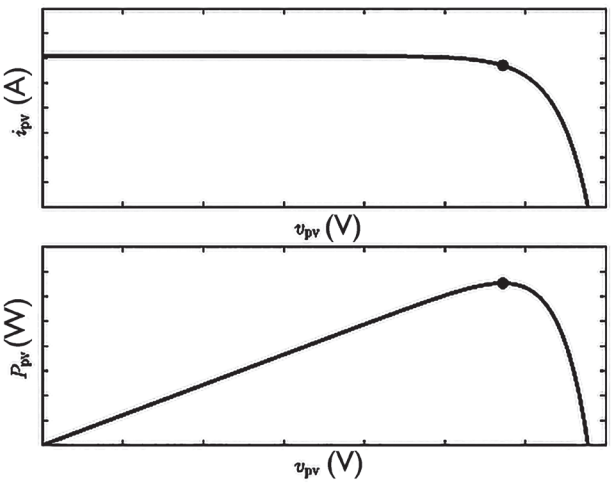

Figura 2. Curvas de voltaje vs. corriente y voltaje vs. potencia de un dispositivo fotovoltaico típico a temperatura e insolación constantes. El círculo rojo indica el punto de máxima generación de potencia.

Como se puede deducir de la figura 2, las características eléctricas de un dispositivo fotovoltaico son no lineales y en algunos casos la unidad de procesamiento de potencia también puede tener características eléctricas no solo no lineales sino también discontinuas. Esta situación requiere de un análisis detallado del sistema que, dada su complejidad, debe ser apoyado

por simulaciones numéricas. El uso de simulaciones numéricas permite realizar experimentos virtuales para probar potenciales soluciones y sistemas, reduciendo significativamente el tiempo de diseño y los errores en la implementación final.

El presente artículo tiene como objetivo identificar un conjunto de herramientas de simulación que pueden apoyar el proceso de diseño de sistemas fotovoltaicos, con un especial enfoque en el diseño de las unidades de procesamiento de potencia. Como se comentará más adelante, enfocarse en el análisis del comportamiento eléctrico de las UPP implica estudiar los transitorios del sistema que normalmente tienen una duración en el orden de los milisegundos. En consecuencia, las herramientas de simulación que se desean identificar no son aquellas que se utilizan para determinar el desempeño de un sistema fotovoltaico en períodos de meses o años, en estos casos ya hay varias herramientas maduras que logran obtener excelentes resultados (Turcotte et al., 2001). Por otro lado, este documento se concentra únicamente en herramientas que sean de acceso libre y abierto, no solo porque representan una opción más económica que las pocas alternativas comerciales existentes, sino porque, dado el carácter particular y reciente del sistema que se quiere estudiar, es necesario contar con herramientas lo suficientemente flexibles que permitan la modificación y alteración de algunas de sus rutinas y modelos.

El presente artículo está estructurado de la siguiente forma: primero se presentan las características eléctricas de los principales sistemas que se quieren simular, esto es, el generador fotovoltaico y la unidad de procesamiento de potencia. A partir de la caracterización de dichos sistemas se obtiene un conjunto de requerimientos que la herramienta de simulación de *software* debe cumplir. Luego, se presenta un conjunto de herramientas de *software* que cumplen de forma total o parcial los requerimientos identificados en la sección anterior. Finalmente, se muestran los resultados de una simulación prueba de sistemas fotovoltaicos con las herramientas seleccionadas y se discutirá cuál es la más apropiada para el enfoque planteado.

Características eléctricas de los principales componentes de un sistema fotovoltaico

Generador fotovoltaico

El efecto fotovoltaico convierte la radiación electromagnética en energía eléctrica. Un dispositivo fotovoltaico es aquel elemento que se diseña y construye con el objetivo de aprovechar al máximo el efecto fotovoltaico. Una de las características más útiles de estos dispositivos es su alta escalabilidad en potencia, esto es, que es posible generar potencias en un amplio rango desde unas decenas de miliwatts hasta gigawatts. Por ejemplo, la celda fotovoltaica más común es una oblea de silicio dopada de forma especial que puede generar entre 100 mW a 1 W. Es posible obtener potencias de entre 10 a 250 W construyendo matrices de celdas eléctricamente conectadas, normalmente en serie, conformando lo que se denomina un módulo o panel fotovoltaico. De igual forma, es posible conformar matrices de paneles fotovoltaicos para llegar a generar hasta decenas de gigawatts.

Existen distintos tipos de tecnologías de celdas fotovoltaicas, las cuales, tal y como se menciona, por ejemplo, en Zinsser, Makrides, Schmitt, Georghiou y Werner (2007), Cereghetti, Realini, Chianese y Rezzonico (2003), Friesen y colaboradores (2007a), Friesen y colaboradores (2007b), Chianese y colaboradores (2007) y Friesen y colaboradores (2010), responden eléctricamente de forma distinta a condiciones ambientales, y por lo tanto su comportamiento eléctrico responde a modelos matemáticos distintos. Por otro lado, el modelo general presentado en Meza y Ortega (2013) es lo suficientemente amplio para abarcar la mayoría de las tecnologías fotovoltaicas disponibles en la actualidad. La expresión matemática de este modelo es la siguiente:

$$i_{pv} = \Lambda(S, T, \rho_{pv}) - \Phi(S, T, v_{PV}, \rho_{PV}) \quad (1)$$

En donde

- i_{pv} es la corriente del generador fotovoltaico.
- v_{pv} es la tensión del generador fotovoltaico.
- S es la intensidad de radiación solar.
- T es la temperatura.
- ρ_{pv} es un conjunto de *n* parámetros que dependen de las características constructivas del dispositivo.

El modelo descrito en la ecuación (1) se puede adecuar a distintas tecnologías por medio de los siguientes parámetros:

- $\rho_{pv} = \{\rho_{pv1}, \rho_{pv2}, \ldots\}$ cada tecnología tiene un valor de ρ_{pvi} y un número de parámetros determinados.
- la función y la función pueden ser distintas para cada tecnología.

Es importante destacar que el anterior modelo pretende representar propiedades comunes que tienen las distintas tecnologías fotovoltaicas en su comportamiento eléctrico, esto es,

- la función $\Phi(S, T, v_{PV}, \rho_{PV})$ es siempre positiva y estrictamente creciente con respecto a v_{pv}.
- $\Lambda(S, T, \rho_{pv})$ es siempre positiva y mayor que $\Phi(S, T, v_{PV}, \rho_{PV})$.

Existen tecnologías fotovoltaicas que tienen asociadas capacitancias parásitas (Friesen et al., 2007). En este caso, es necesario agregar al anterior modelo un componente dinámico de la siguiente forma, tal y como se indica en Meza, Virtuani y Chianese (2010):

$$i_{pv} = \Lambda(S, T, \rho_{pv}) - \Phi(S, T, v_{PV}, \rho_{PV}) - C(v_{PV}, \rho_{PV})\dot{v}_{pv} \quad (2)$$

La función $C(v_{PV}, \rho_{PV})$ es normalmente no lineal y dependiente de v_{pv}.

Con base en los anteriores modelos, podemos afirmar que la simulación del transiente eléctrico de un sistema que utilice un dispositivo fotovoltaico debería ser capaz de:

- Resolver funciones matemáticas no lineales.
- Preferiblemente resolver funciones implícitas. Nótese que según la ecuación (1), existe la posibilidad de que la corriente del dispositivo fotovoltaico aparezca tanto en la parte derecha como en la parte izquierda de la ecuación. Dependiendo de cómo sea la forma de , será posible despejar o no la corriente con funciones matemáticas fundamentales. En algunos casos, utilizando funciones matemáticas como la función de Lambert W (Sharma, 2009) se puede despejar la corriente. En este caso, el sistema de simulación debería ser capaz de resolver esta función o permitir su programación.
- Resolver ecuaciones diferenciales no lineales, en el caso en que se utilice el modelo dinámico de la ecuación (2).

Unidad de procesamiento de potencia

Como se mencionó anteriormente, una unidad de procesamiento de potencia de un sistema fotovoltaico tiene dos objetivos principales:

1. Lograr que el dispositivo fotovoltaico esté siempre posicionado en el punto de operación de máxima potencia.
2. Lograr que la carga tenga un nivel de tensión y corriente determinados.

Dichos objetivos se obtienen por medio de dos elementos: el convertidor de potencia y el subsistema de control. El convertidor de potencia se entiende en este documento como el circuito electrónico conformado por componentes pasivos (inductores y capacitores) y activos (transistores, diodos, etc.), que permiten convertir niveles de tensión y de corriente. Algunos de los dispositivos activos del convertidor de potencia son controlados por medio del subsistema de control, el cual, con las mediciones de las variables eléctricas del convertidor de potencia, los valores de referencia y un algoritmo de control, genera las señales de control. La figura 3 muestra el diagrama de bloques de una unidad de potencia.

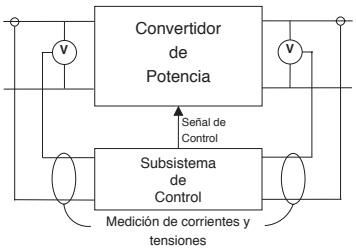

Figura 3. Diagrama de bloques de una unidad de procesamiento de potencia.

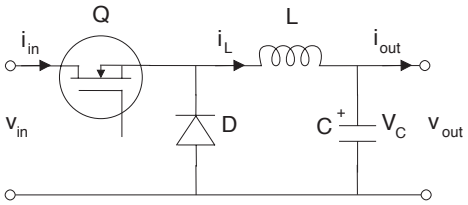

Figura 4. Circuito de un convertidor de potencia tipo reductor.

La gran mayoría de los sistemas fotovoltaicos utiliza convertidores de potencia conmutados. Estos convertidores consisten de capacitores, inductores, diodos y transistores (usualmente MOSFET). Estos últimos operan de forma conmutada con el fin de obtener menores pérdidas en el proceso de conversión. Un convertidor de potencia se puede modelar matemáticamente por medio de un conjunto de ecuaciones diferenciales que describen el proceso de carga y descarga de los elementos que almacenan energía dentro del circuito, esto es, el inductor y el capacitor. Por ejemplo, las ecuaciones que describen el comportamiento dinámico del convertidor reductor que se muestra en la figura 4 son las siguientes:

$$\frac{di_L}{dt} = u\frac{v_{in}}{L} - \frac{v_C}{L}$$

$$\frac{dv_C}{dt} = \frac{i_L}{C} - \frac{i_{out}}{C}$$

En donde

- i_L es la corriente en el inductor L.
- v_c es la tensión en el capacitor C.
- v_{in} es la tensión de entrada al convertidor.
- i_{out} es la corriente de salida del convertidor.
- u es la señal de conmutación del convertidor.

Nótese que en este caso *u* es discontinua, esto es, solo puede tomar los valores 0 o 1. En algunos casos es conveniente utilizar el modelo promediado del convertidor, descrito por las siguientes ecuaciones:

$$x = \begin{bmatrix} x_1 \\ x_2 \end{bmatrix} = \begin{bmatrix} \bar{i}_L \\ \bar{v}_C \end{bmatrix}$$

$$\dot{x} = \begin{bmatrix} 0 & -\frac{1}{\mathrm{L}} \\ \frac{1}{\mathrm{C}} & 0 \end{bmatrix} x + \begin{bmatrix} 0 \\ \frac{\bar{i}_{out}}{\mathrm{C}} \end{bmatrix} + \begin{bmatrix} \frac{\bar{v}_{in}}{\mathrm{L}} \\ 0 \end{bmatrix} d$$

En este caso *d* sustituye a *u*, en donde *d* es una señal continua comprendida entre 0 y 1. Es importante destacar que la simulación del modelo promediado no permite ver los efectos del rizado de conmutación en el sistema.

El subsistema de control es el encargado de conmutar los transistores del convertidor de potencia o equivalentemente de generar la señal *u*. La señal *u* también puede obtenerse a la salida de un generador de anchura de pulso en el caso en el cual el subsistema de control genere la señal *d*. Para generar esta señal, el subsistema de control puede utilizar un algoritmo empírico, ecuaciones diferenciales lineales o no lineales o ecuaciones en diferencia (sistemas discretos).

De esta forma, para la UPP, el sistema de simulación debe ser capaz de:

- Resolver numéricamente ecuaciones diferenciales lineales, no lineales, continuas y con discontinuidades.
- Resolver ecuaciones en diferencia.
- Permitir programar algoritmos empíricos (redes neuronales, lógica difusa, entre otros).

Finalmente, sería de mucha utilidad que el algoritmo o las ecuaciones dinámicas del subsistema de control pudieran exportarse de forma sencilla, para ser implementados en un microcontrolador o un sistema de prototipado rápido.

Herramientas de simulación

Scilab/Scicoslab: Scilab es un programa computacional científico para cálculos numéricos, que provee un poderoso entorno de computación abierta para aplicaciones científicas y de ingeniería. Scicos permite realizar modelados y simulaciones en forma gráfica de sistemas dinámicos, lo cual se ejecuta bajo Scilab. Scilab y Scicos han sido desarrollados por el Instituto Nacional Francés para la Investigación en Ciencias de la Computación (INRIA), desde 1990. Además del conjunto de funciones predefinidas de Scilab, un grupo de investigadores ha desarrollado nuevas e importantes funciones con propósitos educativos (por ej., Pendharkar,

2005 y Meza, Andrade-Romero, Alavarez y Coelho, 2010) y para el diseño de sistemas de control avanzados (por ej., Delebecque, 2000). Scilab ha sido utilizado en una amplia variedad de aplicaciones en investigación, tales como la identificación de fuentes de contaminación en ríos, descrita en Chancelier, Cohen, Maldinery y Pacard (1996) y en la mejora de las máquinas de prueba para fricción, mencionado en Dongping, Dongjie y Qiang (2007). Siendo un *software* científico altamente sofisticado y gratuito, ha podido ser utilizado ampliamente para propósitos educativos, tanto en países industrialmente desarrollados como en vías de desarrollo.

Python: es un lenguaje de programación de propósito general orientado a objetos diseñado para ser interpretado, esto es, está compuesto de un conjunto de instrucciones que deben ser convertidas a operaciones ejecutables por el computador. Esto hace que el lenguaje se pueda aprender de forma sencilla ya que el código creado se puede probar y depurar de forma rápida y fácil.

Python se ha extendido ampliamente en los últimos años debido sobre todo a las siguientes ventajas:

- Es libre y abierto y está incluido en la gran mayoría de las distribuciones de Linux.
- Está disponible para la mayoría de los sistemas operativos (Linux, Unix, Windows, Mac OS). Un programa escrito para un sistema se ejecuta en los otros sin necesidad de modificarlo.
- Es más fácil de aprender y produce código más fácilmente entendible que otros lenguajes de programación.
- Python y sus extensiones son fáciles de instalar.

Existen numerosas librerías y extensiones para Python. Una de las más útiles para la simulación de sistemas dinámicos es SciPy, que es una colección de algoritmos para el cálculo numérico, procesamiento de datos y operaciones matriciales, optimización y estadística, entre otros. El usuario puede utilizar estos algoritmos de una forma sencilla e intuitiva y de modo muy similar a otros lenguajes comerciales para uso científico, como Matlab.

Una de las grandes ventajas de usar Python con SciPy es, además de las ventajas de Python anteriormente mencionadas, que funciona como una forma flexible y útil de integrar librerías compiladas en otros programas como C, C++ y Fortran. Por estas razones, Python y SciPy se han usado para el modelado de sistemas dinámicos en múltiples y variadas aplicaciones, como el modelado de sistemas celulares (Olivier, Rohwer y Hofmeyr, 2005) y convertidores de potencia (Meza y Ortega, 2013).

Prueba de simulación y discusión

Con el fin de probar las herramientas de simulación identificadas, se utilizó un caso de estudio de un sistema fotovoltaico para la carga de una batería. Este sistema se muestra en la figura 5 y consiste de un panel fotovoltaico que alimenta a una batería por medio de un convertidor de potencia reductor. Las ecuaciones dinámicas que describen el comportamiento eléctrico de este sistema son las siguientes:

$$\begin{aligned} \dot{x_1} &= \frac{i_{pv}(x_1)}{\mathrm{C}} - \frac{ux_2}{\mathrm{C}} \\ \dot{x_2} &= \frac{ux_1}{\mathrm{L}} - \frac{E}{\mathrm{L}} \\ i_{pv}(x_1) &= \Lambda - \Phi(x_1) \end{aligned} \quad (3)$$

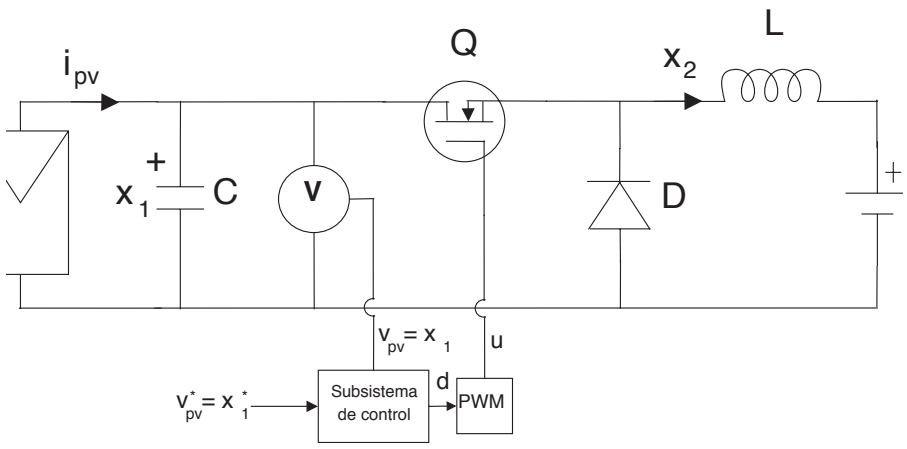

Figura 5. Circuito esquemático del caso de estudio utilizado para evaluar las herramientas de simulación.

en donde $\Phi(\cdot) = \psi e^{\alpha v_{pv}}$ y se considera que la radiación *S* y la temperatura *T* son constantes. El cuadro 1 muestra el valor de los parámetros utilizados para la simulación.

Cuadro 1. Parámetros del sistema descrito por la ecuación (3) para su simulación.

Parámetro	Valor	Unidades
ψ	0.0022	A
Λ	1.2	A
α	0.2	1/V
E	12	V
L	47	mH
C	0.1	mF

Como se puede observar en la figura 5, existe un subsistema de control que genera un ciclo de trabajo *d* que luego es es utilizado por un modulador de anchura de pulsos para generar la señal *u* que controla la activación del transistor. El subsistema de control también está definido por medio de un conjunto de ecuaciones diferenciales que se muestra a continuación.

$$u = K_P \tilde{x}_1 + K_I \omega$$
$$\dot{\omega} = \tilde{x}_1$$
$$\tilde{x}_1 = x_1 - x_1^* \qquad (4)$$

en donde los parámetros K_P y K_I se utilizan para ajustar el comportamiento dinámico del sistema en lazo cerrado.

El subsistema de control debe asegurar que $d \in [0,1]$. De esta forma, el modulador de anchura de pulsos, comparando *d* con una señal moduladora triangular o diente de sierra con una amplitud de 1, puede generar *u*. La expresión matemática que describe la operación del modulador de anchura de pulsos es la siguiente:

$$m = \frac{1}{T_S} - \left[\frac{1}{2} + \frac{t}{T_S}\right] + \frac{1}{2} \quad (5)$$
$$u = \begin{cases} 1 \text{ si } d > m \\ 0 \text{ si } d < m \end{cases}$$

en donde representa la función máximo entero (*floor*) que se define de la siguiente forma:

$$\lfloor x \rfloor = max\{k \in Z \vee k \leq x\}$$

esto es, la función máximo entero aplicado a una variable *x* devuelve el máximo número entero *k* no superior a *x.*

Llegados a este punto, es importante destacar que existen dos sistemas que se pueden analizar y estudiar. Uno que considera únicamente el comportamiento eléctrico del sistema de la ecuación 3 promediado en los periodos de conmutación del transistor y otro que sí toma en cuenta los efectos del sistema debido a la conmutación. Tal y como se mencionó anteriormente, el primer caso se obtiene de la ecuación 3 sustituyendo *u* por *d*. A continuación, se presentan los resultados de simulación para ambos casos.

Las condiciones iniciales y los parámetros para el método numérico utilizados se muestran en los cuadros 2 y 3, respectivamente. Los parámetros del subsistema de control utilizados fueron K_P = 0.1 y K_I = 0.75 con una señal de referencia $x_1^* = v_{pv}^* = 24V$.

Cuadro 2. Condiciones iniciales (cuando *t=0*) del sistema descrito por la ecuación (3) para su simulación.

Variable	Valor
$x_1 = v_{pv}$	31.51
$x_2 = i_{out}$	0
W	0

Cuadro 3. Parámetros para el método numérico utilizado para resolver las ecuaciones diferenciales del sistema simulado.

Parámetro	Valor
Máximo error absoluto permitido	$1x10^{-8}$
Máximo error relativo permitido	$1x10^{-8}$
Paso de integración máximo permitido	0.001
Tiempo de simulación	0.6
Cantidad de datos tomados en el tiempo de simulación	$1x10^{5}$

Simulación con Python

Se utilizó la versión 2.7.3 de Python con la extensión Numpy (ver 1.6.2) y las bibliotecas SciPy (ver 0.10.1) y Matplotlib (ver 1.1.1). El programa que describe el sistema a simular consistió en unas pocas líneas de código que utiliza, principalmente, el solucionador de ecuaciones diferenciales incluido en la biblioteca SciPy. Dicho solucionador está tomado de la colección de métodos numéricos descritos en la librería ODEPACK para Fortran. Este solucionador de ecuaciones diferenciales permite resolver numéricamente ecuaciones diferenciales ordinarias de tipo rígidas o *stiff*, que en varias ocasiones están presentes en sistemas dinámicos de convertidores de potencia. Los resultados de simulación del sistema promediado pueden observarse en la figura 6, los cuales se corresponden con el comportamiento esperado.

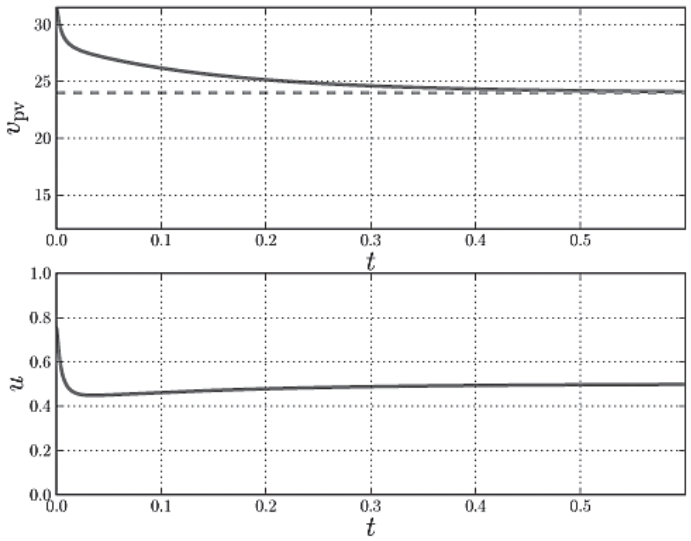

Figura 6. Resultados de simulación del sistema de la Figura 4 descrito por las ecuaciones 4 y 5.

Se pudo comprobar que Python y sus extensiones existentes no permiten de forma sencilla y directa simular sistemas dinámicos que deben realizar funciones guiadas por distintos períodos de tiempo. Este es el caso de la simulación del sistema en estudio tomando en cuenta las conmutaciones del transistor. En este sentido, es importante destacar que, en la mayoría de los casos, el subsistema de control es diseñado a partir del modelo promediado del sistema. Esto ocurre, por ejemplo, cuando se utilizan controles proporcionales e integrales tal y como el que está indicado en la Ecuación 4. Bajo estas condiciones, se parte del supuesto de que la señal generada por el control *d* permanecerá constante durante un ciclo de conmutación del transistor. Más aún, el subsistema de control debería recibir las señales promediadas o muestreadas de tal y como se indica en la figura 7. Si bien es cierto, los mencionados requerimientos no representan mayor problema para el análisis dinámico del sistema o para el diseño del subsistema de control, sí dificultan su implementación en Python. Como se dijo anteriormente, la dificultad radica en la necesidad de definir subsistemas que operan a distintos instantes, a saber, el sistema de ecuaciones diferenciales que es resuelto a un paso de integración dado y el sistema de promediado o muestreo de datos que debe resolver en un período de conmutación del transistor.

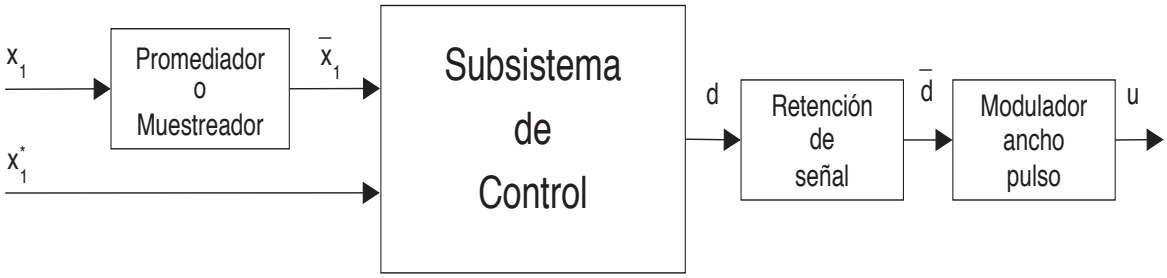

Figura 7. Subsistema de control que genera un ciclo de trabajo *d* para un modulador de anchura de pulsos.

Aunque es posible escribir código en Python para atender el requerimiento anteriormente mencionado, los autores consideran que resulta innecesario dado que, como se indica a continuación, existen otras herramientas que resuelven el anterior problema de forma muy sencilla.

Simulación con Scicos

Para esta simulación se utilizó la versión 4.4.1-1 de Scicoslab y la versión 4.4.1 de Scicos. Al igual que en el caso de Python + SciPy, Scicoslab y Scicos utilizan el paquete ODEPACK para la resolución numérica de ecuaciones diferenciales ordinarias.

Scicos permite definir un sistema dinámico por medio de un diagrama de bloques, con lo cual el caso de prueba se definió tal y como se muestra en las figuras 8 y 9. En la figura 8 se muestra el modelo del sistema promediado que se corresponde con el sistema simulado utilizando Python descrito en la sección precedente. Por otro lado, la figura 9 muestra el diagrama de bloques del sistema con el modulador de anchura de pulsos. Este sistema no se pudo simular en Python por las razones anteriormente expuestas, no obstante, gracias a la flexibilidad que ofrece la definición del sistema con bloques, este sí se pudo realizar en Scicos.

El resultado de la simulación en Scicoslab + Scicos con los parámetros de simulación de el cuadro 3 se muestra en las figuras 10 y 11. Nótese que para el modelo promediado se obtuvo la misma respuesta dinámica en Python y en Scicoslab (Figura 6 - Python y Figura 10 - Scicoslab). Así mismo, en la figura 11 se muestra un comportamiento promedio similar al de las figuras 6 y 10, pero en este caso es posible ver el rizado en la tensión del dispositivo fotovoltaico debido a la conmutación del interruptor (ver figura 12).

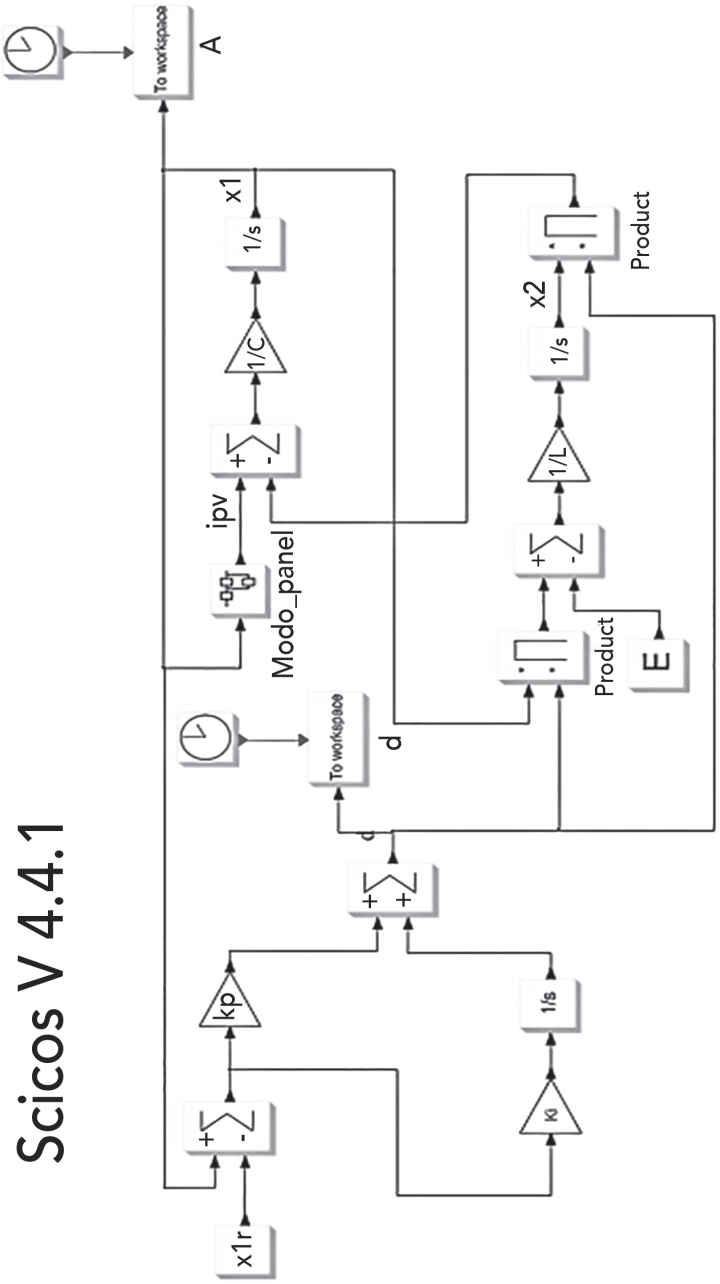

Figura 8. Diagrama de bloques del sistema promediado, equivalente a la simulación realizada con Python.

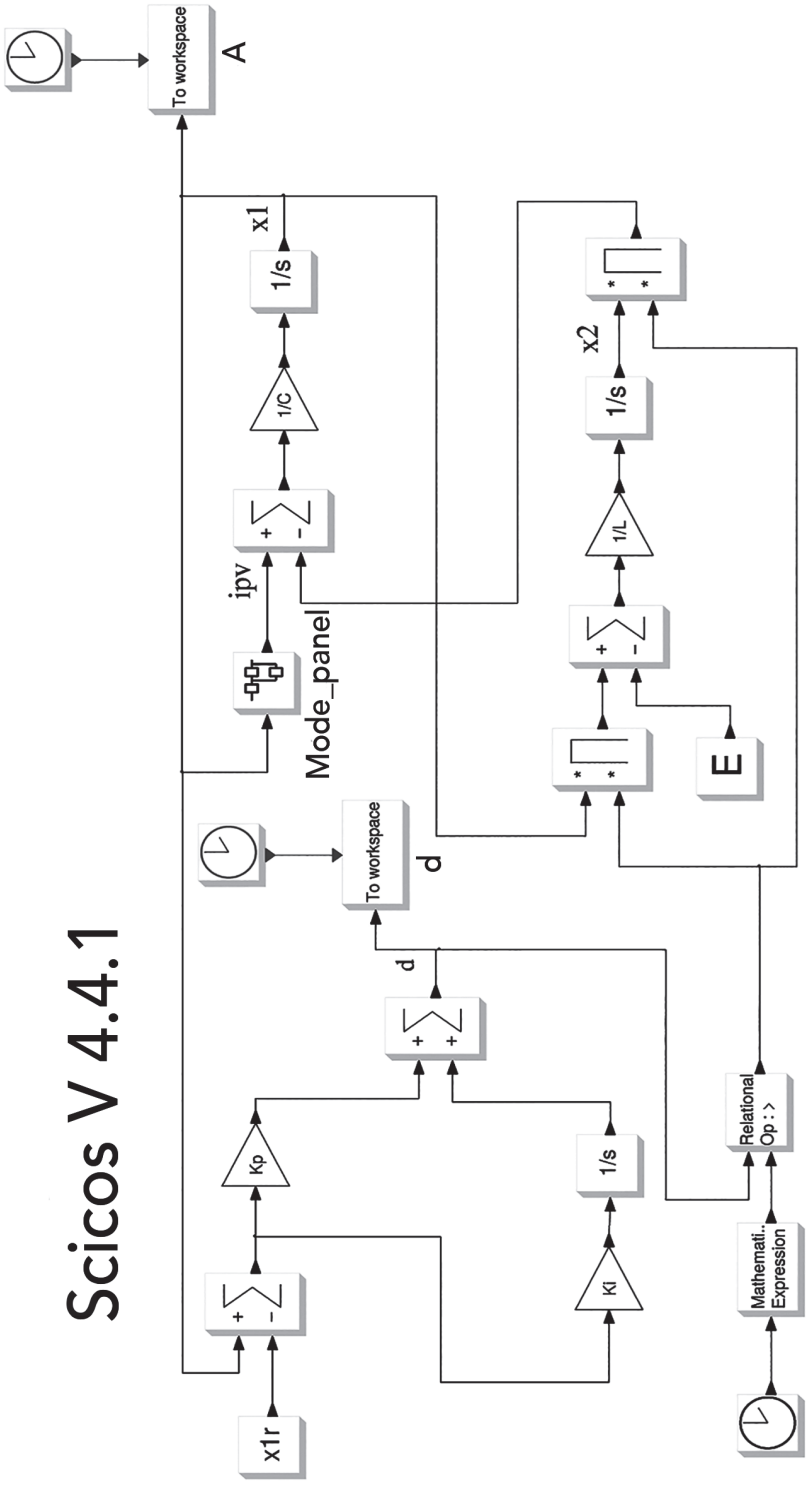

Figura 9. Diagrama de bloques del sistema con el control y el modulador de ancho de pulso.

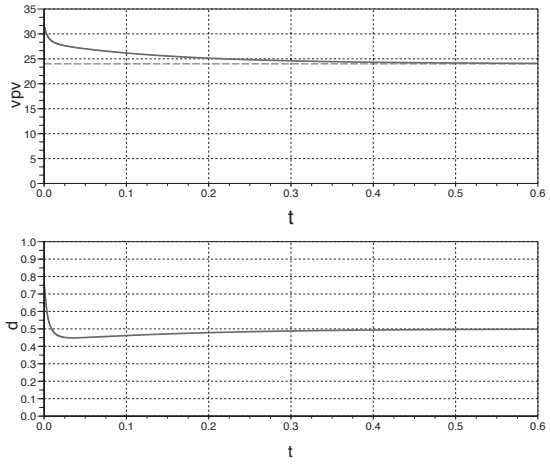

Figura 10. v_{pv} y u obtenidos de la simulación con Scicoslab + Scicos, para el sistema de la Figura 5 con el modelo de la Figura 8.

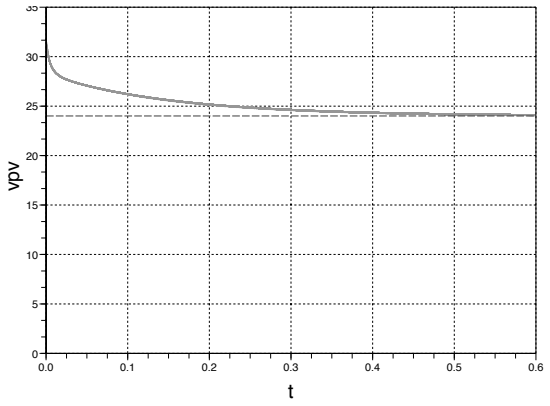

Figura 11. v_{pv} obtenido de la simulación con Scicoslab + Scicos, para el sistema de la Figura 5 con el modelo de la Figura 9.

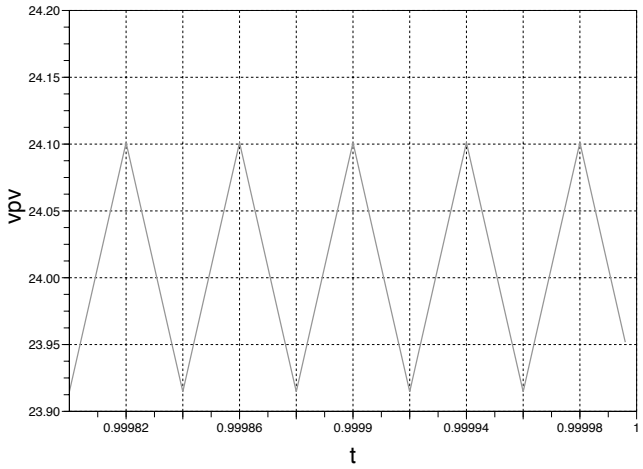

Figura 12. Rizado de la tensión v_{pv} mostrado en la Figura11.

Conclusiones y recomendaciones

En el presente artículo se ha utilizado un sistema fotovoltaico para cargar una batería, como un caso de estudio que permita probar la versatilidad de dos herramientas de simulación de sistemas dinámicos, a saber, Python + SciPy y Scicoslab + Scicos. Dichas herramientas son abiertas y libres y pueden ser utilizadas en las plataformas informáticas más comunes.

Tanto Python como Scicoslab permitieron realizar simulaciones del sistema dinámico promediado, no así del sistema completo conformado por el control y el modulador de ancho de pulso, elementos presentes en los sistemas fotovoltaicos convencionales. En este apartado, el trabajo con Scicoslab se pudo realizar de forma sencilla, debido principalmente a que permite el desarrollo de simulaciones que requieren funciones guiadas por distintos periodos de tiempo. Esto último, si se quisiera desarrollar en Python, exigiría un esfuerzo importante en programación.

Pese a que Python es muy versátil debido a que permite integrar numerosas librerías para el cálculo numérico de manera sencilla, el desarrollo de procesos de simulación con cierto nivel de complejidad exige una inversión importante de tiempo en la etapa de programación. Por otro lado, Scicoslab brinda un ambiente gráfico que facilita el proceso de definición e implementación de sistemas dinámicos complejos, en los cuales es posible manejar diferentes tiempos de procesamiento, como, por ejemplo, para la resolución numérica de una ecuación diferencial ordinaria y el proceso de conmutación del transistor, ambas situaciones presentes en las unidades de procesamiento de potencia de los sistemas fotovoltaicos.

Bibliografía

Boke. U. (septiembre, 2007). *A simple model of photovoltaic module electric characteristics.* European Conference on Power Electronics and Applications, 1-8.

Cereghetti, N., Realini, A., Chianese, D. & Rezzonico, S. (2003). *Power and Energy production of PV modules.* IEEE 3rd World Conference in Photovoltaic Energy Conversion.

Chancelier, J., Cohen, M., Maldinery, M. & Pacard, F. (1996). *Identification of pollution sources in rivers*. IEEE International Symposium on Computer-Aided Control System Design.

Chianese, D., Friesen, G., Pasinelli, P., Pola, I., Realini, A., Cereghetti, N. & Bernasconi, A. (2007). *Direct Performance Comparison of PV Modules*. 22th European Photovoltaic Solar Energy Conference.

Delebecque, F. (2000). *A slicot based control library for Scilab*. IEEE International Symposium on Computer-Aided Control System Design.

Dongping, Q., Dongjie, Z. & Qiang, T. (2007). *Linux/rtai and Scicos in low cost high performance friction testing machine.* International Conference on Electronic Measurement and Instruments.

Friesen, G., Gottschalg, R., Beyer, H. G., Williams, S., Guerin de Montgareuil, A., van der Borg, N., van Sark, W., Huld, T., Müller, B., de Keizer, A. C. & Niu, Y. (2007a). En *Intercomparison of different energy prediction methods within the European project performance – results of the 1nd Round Robin.* 22th European Photovoltaic Solar Energy Conference.

Friesen, G., Chianese, D., Pola, I., Realini, A. & Bernasconi, A. (2007b). En *Energy Rating Measurements and Predicitions at ISAAC.* 22th European Photovoltaic Solar Energy Conference.

Friesen, G., Chianese, D., Dittmann, S., Dominé, D., Burà, E., Strepparava, D., Margna, B., Denicolà, M., Meoli, R. & Pola, I. (2010). En *Performance intercomparison of 13 different PV modules based on indoor and outdoor test.* 25th European Photovoltaic Solar Energy Conference.

Gow, J. A. & Manning, C. D. (marzo, 1999). Development of a photovoltaic array model for use in power-electronics simulation studies. Electric Power Applications. *IEE Proceedings, 146*(2), 193-200.

Kiusalaas, J. (2013). *Numerical Methods in Engineering with Python 3*. Cambridge University Press.

Lasnier, F. (1990). *Photovoltaic Engineering Handbook*. Taylor & Francis.

Liu, S. & Dougal, R. (2002). Dynamic multiphysics model for solar array. *IEEE Transactions on Energy Conversion, 17*, 285-294.

Meza, C., Andrade-Romero, J. A., Alavarez, M. A. & Coelho, A. A. A. (2010). *Improving Control Engineering Education Using Foss Tools.* XVIII Congresso Brasileiro de Automatica, Bonito, Brasil.

Meza, C., Virtuani, V. & Chianese, D. (septiembre, 2010). *Evaluation of models for the internal capacitance of a pvmodule for the design and simulation of power converters.* 25th European Photovoltaic Solar Energy Conference and Exhibition.

Meza, C. & Ortega, R. (2013). *Control and estimation scheme for PV central inverters*. XXIV IEEE International Conference on Information, Communication and Automation Technologies (ICAT).

Olivier, B. G., Rohwer, J. M. & Hofmeyr, J. H. (2005). Modelling cellular systems with PySCeS. *Bioinformatics* 21.4 (2005), 560-561.

Pendharkar, I. (2005) Rltool for Scilab: A public domain tool for SISO system design. *IEEE Control System Magazine, 25*, 23-25.

Sharma, S. & Kapoor, A. (2009). PV Generator Driven First Order Circuit – Transient Analysis using LambertW Function. *The Open Renewable Energy Journal*, *2*, 111-115.

Turcotte, D., Ross, M. & Sheriff, F. (septiembre, 2001). Photovoltaic hybrid system sizing and simulation tools: status and needs. En *PV Horizon: Workshop on Photovoltaic hybrid systems,* Montreal, Canada.

Zinsser, B., Makrides, G., Schmitt, W., Georghiou, G. E. & Werner, J. H. (2007). *Annual energy yield of 13 photovoltaic technologies in Germany and in Cyprus.* 22th European Photovoltaic Solar Energy Conference.

Energy-Balance Control of PV Cascaded Multilevel Grid-Connected Inverters Under Level-Shifted and Phase-Shifted PWMs

Javier Chavarría, Domingo Biel, *Member, IEEE*, Francesc Guinjoan, *Member, IEEE*, Carlos Meza, *Member, IEEE*, and Juan J. Negroni, *Member, IEEE*

***Abstract*—This paper presents an energy-balance control strategy for a cascaded single-phase grid-connected H-bridge multilevel inverter linking n independent photovoltaic (PV) arrays to the grid. The control scheme is based on an energy-sampled data model of the PV system and enables the design of a voltage loop linear discrete controller for each array, ensuring the stability of the system for the whole range of PV array operating conditions. The control design is adapted to phase-shifted and level-shifted carrier pulsewidth modulations to share the control action among the cascade-connected bridges in order to concurrently synthesize a multilevel waveform and to keep each of the PV arrays at its maximum power operating point. Experimental results carried out on a seven-level inverter are included to validate the proposed approach.**

***Index Terms*—Cascaded H-bridge inverters, discrete-time control, grid-connected PV systems, multilevel modulations.**

I. Introduction

A LOW-CARBON society is a current political trend in developed countries which promotes, among others, the connection of photovoltaic (PV) systems to the electrical grid. These systems can contribute to clean electricity production as they are harmless for the environment and reduce the dependence on polluting fossil fuels such as coal, oil, gas, and nuclear. In addition, the power scalability of PV generation facilitates its large-scale penetration and leads to grid-connected applications ranging from few kilowatts of small residential PV systems primarily installed on roofs to several megawatts of large-scale PV power plants.

Nevertheless, since the cost per watt of the PV system is still high compared to other energy sources, current research focuses on both reducing manufacturing costs and increasing the energy production of the overall system. In particular, the power conditioning stage interfacing the PV modules to the grid has caught the attention of researchers since it must account for maximum power extraction from the energy source and an optimal energy transfer to the grid [1]. In this concern, string and multistring power conditioning architectures have been proposed over the last two decades to improve the features of the central-inverter-based one [2]–[6].

Among the power converter topologies adopted in the aforementioned architectures, multilevel inverter ones are being investigated as an interesting option for grid-connected PV systems [7]–[19]. In particular, the cascaded H-bridge multilevel inverter (CHB-MLI) topology, as shown in Fig. 1, is particularly attractive for grid-connected PV applications for the following reasons [2], [8], [10].

1) The output voltage level required for grid power injection can be achieved without the use of a transformer as the voltage boosting is shared between the dc series connection of PV modules and the cascade connection of H-bridge outputs.
2) This topology allows the connection of independent strings of PV modules to the input dc links of the power stage. Since the dc link voltages can be independently controlled, the maximum power extraction of a reduced number of PV modules can be accomplished with the help of maximum power point tracking (MPPT) algorithms. This improves both PV system reliability and energy production when the PV modules operate under mismatching conditions such as in the case of partial shadowing.
3) Like other multilevel inverter topologies, the CHB-MLI allows the synthesis of staircase ac output waveforms with lower total harmonic distortion (THD) compared to those generated by two-level-based inverters, thus releasing output filter requirements for the compliance of grid harmonic standards. Depending on the operation power level, this synthesis can be carried out either at the fundamental frequency [20] or at higher switching frequencies using multicarrier-based modulations [8], [10], [21], [22].

As shown in Fig. 1, the control strategy of the CHB-MLI requires a set of voltage controllers to ensure independent voltage control of each PV array, a current controller driving the injected grid current to assure overall power transfer at

Manuscript received August 17, 2011; revised December 5, 2011; accepted January 14, 2012. Date of publication January 26, 2012; date of current version September 6, 2012. This work was supported in part by the Spanish Ministry of Science and Innovation and EU FEDER funds under Grants DPI2009-14713-C03-03, DPI2010-15110, and RUE CSD2009- 00046 (Consolider-Ingenio 2010 Programme).

J. Chavarría, D. Biel, and F. Guinjoan are with the Department of Electronic Engineering, Universitat Politècnica de Catalunya, 08034 Barcelona, Spain (e-mail: javier.chavarria@upc.edu; domingo.biel@upc.edu; francesc.guinjoan@upc.edu).

C. Meza is with the Department of Electronic Engineering, Instituto Tecnológico de Costa Rica, Cartago 159-7050, Costa Rica (e-mail: cmeza@itcr.ac.cr).

J. Negroni is with the Department of Electronic Engineering, Universidad Tecnológica Metropolitana, Santiago 97279, Chile (e-mail: juan.negroni@utem.cl).

Color versions of one or more of the figures in this paper are available online at http://ieeexplore.ieee.org.

Digital Object Identifier 10.1109/TIE.2012.2186108

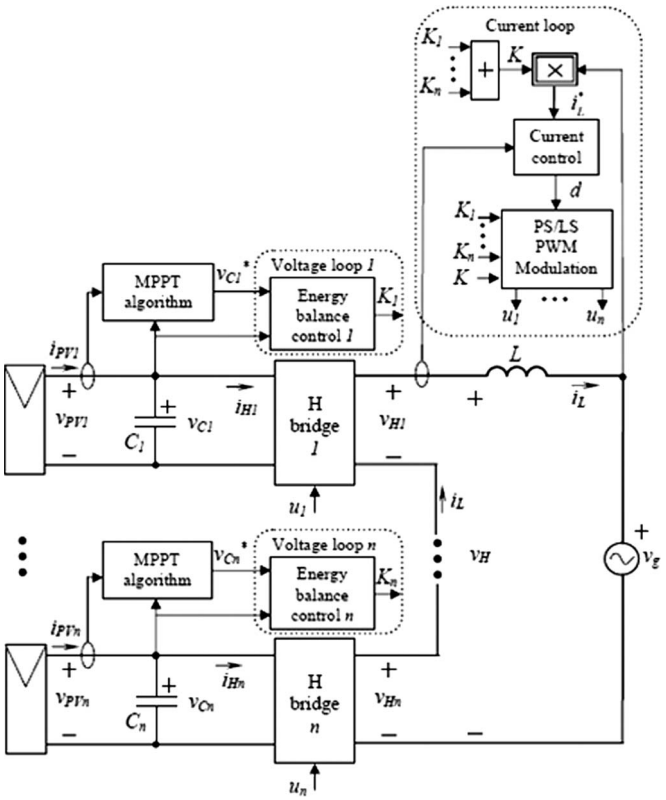

Fig. 1. Grid-connected PV multilevel inverter.

unity power factor, and multilevel modulation to synthesize the staircase output voltage with low THD.

Except in the recent work of Cecati *et al.* [12], which suggests a fuzzy control approach to implement an extended version of this strategy allowing reactive power control, the aforementioned controllers have been typically designed by continuous-time linear control techniques. For instance, continuous-time PI voltage controllers can be found in [15] and, more recently, in [16] whose design follows the guidelines suggested in [23]. However, as pointed out in [24], these designs do not address system stability for the whole irradiance and temperature operating ranges since the nonlinear parametric dependence of the system resulting from the nonlinear current to voltage characteristics of the PV arrays is neglected.

Regarding output current control and multilevel modulation techniques, nonlinear current controllers based on sliding mode control and multiband hysteresis modulations operating at a variable switching frequency have recently been reported [18], [25]. However, linear PI or proportional–resonant (PR) current controllers [26], [27] and fixed-frequency multicarrier-based pulsewidth modulations (PWMs) are preferred in low-power applications to facilitate the design of the reactive components. In this regard and to the author's knowledge, only phase-shifted PWM (PS-PWM) has been applied to the CHB-MLI for grid-connected applications [15], [16], [19].

Collecting previous results [18], [19], [24], the work here reported presents the design of a discrete-time linear voltage controllers for independent voltage control of each PV array, thus ensuring system stability for the whole irradiance operating range. Assuming a linear PR current controller, this paper also describes the design of the control signals driving each H-bridge for PS-PWM to further extend the results to level-shifted carrier PWM (LS-PWM).

This paper is organized as follows. The PV system modeling and the control strategy definition are presented in Section II. Section III focuses on the energy-balance control approach and sets controller design criteria. Section IV addresses the generation of control signals driving the PV inverter switches for PS- and LS-PWMs. Several different tests carried out on a seven-level inverter prototype linking three independent PV arrays to the grid are presented in Section V for both modulations to experimentally verify the proposed approach. Finally, Section VI draws the conclusions of this work.

II. System Modeling and Control Strategy Definition

The grid-connected PV multilevel inverter under study is shown in Fig. 1. It comprises n PV generators and a power conditioning unit, including n full-bridge inverters whose outputs are series connected to the grid. Each PV generator is connected at the input of one full-bridge inverter. This section introduces the formal mathematical modeling of the system and the control strategy to be designed.

A. PV Generators

All PV generators are formed by an array of series-connected PV panels with identical PV cells. The current-to-voltage relationship of the kth PV generator can be extrapolated from the PV cell model of Prince [28] as follows:

$$i_{PVk} = I_{gk} - I_{satk}\left(\mathrm{e}^{\left(\frac{v_{Ck}}{\eta_k V_{Tk}}\right)} - 1\right), \qquad k = 1, \ldots, n \tag{1}$$

where i_{PVk} and v_{Ck} are the output current and voltage, respectively, of the kth PV generator, I_{gk} represents the light-induced current, η_k stands for the emission coefficient, I_{satk} is the reverse saturation current, and V_{Tk} represents the thermal voltage of the semiconductor material. This model assumes that each generator can operate at different irradiance and temperature levels, i.e., each generator can exhibit a different maximum power point (MPP) at any time.

B. Power Conditioning Unit

As for the variables in Fig. 1, the kth cascaded bridge can be modeled as follows if no losses are considered:

$$\begin{cases} v_{Hk} = u_k v_{Ck}, & k = 1, 2, \ldots, n \\ i_{Hk} = u_k i_L, & k = 1, 2, \ldots, n \end{cases} \tag{2}$$

where u_k stands for the control signal of each full-bridge inverter, which is assumed to operate under three-level modulation, thus restricting the values of the control signal to $u_k \in \{-1, 0, 1\}$. The lossless operation of each inverter cell can be derived in terms of instantaneous power since, from (2), the following identity holds:

$$v_{Ck} i_{Hk} = v_{Hk} i_L. \tag{3}$$

The output voltage of the cascaded inverters v_H is given by

$$v_H = \sum_{k=1}^{n} v_{Hk} = \sum_{k=1}^{n} u_k v_{Ck}. \tag{4}$$

Finally, the system dynamics can be modeled by the following set of differential equations:

$$C_k \frac{dv_{Ck}}{dt} = i_{PVk} - u_k i_L, \qquad k = 1, \ldots, n \tag{5a}$$

$$L \frac{di_L}{dt} = \sum_{k=1}^{n} u_k v_{Ck} - v_g(t) \tag{5b}$$

where v_g represents the grid voltage, which is assumed to be purely sinusoidal, i.e.,

$$v_g(t) = A\ \sin(\omega_g t) \tag{6}$$

with ω_g being the grid angular frequency. It is worth noting that the dynamic description of the PV system is given by (1), (5), and (6) and involves the nonlinear i–v relationship of the PV arrays.

C. Control Strategy

The control of the multilevel inverter must achieve the following goals.

1) Operation of each PV generator at its own MPP independently of the ambient conditions to assure the maximum power extraction of each array.
2) Transfer of the overall dc power to the grid. This is performed by the output current $i_L(t)$ which must be injected to the grid with low harmonic distortion at unity power factor.
3) Synthesis of a multilevel steplike ac wave voltage $v_H(t)$ at the output of the cascaded converter.

The following paragraphs summarize the control strategy of the system according to the block diagram in Fig. 1.

The first goal requires the design of a voltage control loop per array which regulates the corresponding capacitor voltage v_{Ck} to a reference value given by the MPPT algorithm (v_{Ck}^* in Fig. 1) at any time. This paper assumes that the aforementioned reference signals come from conventional Perturb & Observe MPPT algorithms [29].

With regard to the second goal, the injection of the dc power in phase with the grid entails the control of the output current i_L (i.e., the design of a current loop) to track, with a fast transient response and zero steady-state error, a current reference i_L^* given by

$$i_L^*(t) = K(t) v_g(t) = K(t) A\ \sin(\omega_g t) \tag{7}$$

where the current amplitude $K(t)A$ must be time varying to deal with the time-varying input dc power. When the output current reaches this reference, the transfer condition of the overall average power over a grid period can be formulated as

$$\frac{1}{T_g} \int_{(m-1)T_g}^{mT_g} \sum_{k=1}^{n} i_{PVk}(\tau) v_{Ck}(\tau)\, d\tau = \frac{1}{T_g} \int_{(m-1)T_g}^{mT_g} K(\tau) \left(A\ \sin(\omega_g \tau)\right)^2 d\tau. \tag{8}$$

However, since the temperature and irradiance vary slowly within a grid period, so does the input dc power. Therefore, the average dc power can be approximated as

$$\frac{1}{T_g} \int_{(m-1)T_g}^{mT_g} \sum_{k=1}^{n} i_{PVk} v_{Ck}\, d\tau \approx \sum_{k=1}^{n} i_{PVk(m-1)} v_{Ck(m-1)}.$$

This assumption allows the value of $K(t)$ to be updated only at the beginning of each grid period, i.e.,

$$K(t) = K_{(m-1)} \quad \text{for} \quad (m-1)T_g \le t \le mT_g;\ m = 1, 2, \ldots.$$

Accordingly, the current reference given in (5) can be rewritten as

$$i_L^* = K_{(m-1)} A\ \sin(\omega_g t). \tag{9}$$

Hence, the transfer condition of the average power given in (8) becomes

$$\sum_{k=1}^{n} i_{PVk(m-1)} v_{Ck(m-1)} = K_{(m-1)} A^2/2. \tag{10}$$

In other words, if the current controller drives the output current to properly track a current reference given by (9) and (10), the overall average dc power is transferred to the grid. In particular, if this power is set to its maximum value by the voltage controllers, the maximum power transfer is achieved. It is worth noting that this approach leads to discrete-time relationships among the system variables sampled at the grid period, as proposed for the control design of high-power-factor preregulators [30]–[32].

Finally, the design of the "modulation" block in Fig. 1 focuses on the last control goal. The block contains the same number of PWM modulators and cascaded inverter cells and delivers the control signals u_k driving each bridge. These signals are built based on both the information of the current loop which is related to the overall power transfer (d in Fig. 1) and the information of the voltage loops ($K_1, \ldots, K_n$ in Fig. 1) which, in turn, is related to the power handled by each inverter. The multilevel steplike ac output voltage v_H is synthesized using PWM techniques based on phase-shifted (PS) and level-shifted (LS) triangular carriers. The details of the generation of these control signals for both modulations are addressed in Section IV.

A direct attempt of control design from the system dynamics given in (1), (5), and (6) is cumbersome due, among others, to

the current-to-voltage nonlinear relationship of the PV generators described in (1). The following approach undertakes this design to ensure at least the local stability of the system.

III. Energy-Balance Control Approach

A. Energy-Balance Linear Modeling

In terms of instantaneous power, the system can be characterized by the following power-balance equation:

$$\sum_{k=1}^{n} i_{PVk} v_{Ck} = \sum_{k=1}^{n} v_{Ck} C_k \frac{dv_{Ck}}{dt} + L i_L \frac{di_L}{dt} + i_L v_g. \quad (11)$$

Assuming that the output current i_L has reached the reference value i_L^* given in (9) and (10) and integrating over a grid period yields

$$\int_{(m-1)T_g}^{mT_g} \sum_{k=1}^{n} i_{PVk} v_{Ck} d\tau = \sum_{k=1}^{n} \frac{C_k}{2} \left[v_{Ckm}^2 - v_{Ck(m-1)}^2 \right] + \frac{K_{(m-1)} A^2 T_g}{2}. \quad (12)$$

If E_{PVkm} stands for the dc energy produced by the kth PV array during the m grid period and E_{Ckm} is the energy stored in the capacitor, namely

$$E_{PVkm} = \int_{(m-1)T_g}^{mT_g} i_{PVk} v_{Ck}\, d\tau \quad (13a)$$

$$E_{Ckm} = 0.5 C_k v_{Ckm}^2 \quad (13b)$$

equation (12) can be rewritten as the following dynamic energy-balance equation:

$$\sum_{k=1}^{n} \left[E_{Ckm} - E_{Ck(m-1)} \right] = \sum_{k=1}^{n} E_{PVkm} = \frac{K_{m-1} A^2 T_g}{2}. \quad (14)$$

However, as pointed out in [24], the aforementioned dynamic description is still not complete since E_{PVkm} and E_{Ckm} are dependent one on another through the current-to-voltage nonlinear characteristic of the PV generator given in (1). From (1) and (13), this nonlinear dependence can be found as

$$E_{PVkm} = \int_{(m-1)T_g}^{mT_g} \sqrt{\frac{2}{C_k} E_{Ck}} \left[I_{gk} - I_{satk} \left(\mathrm{e}^{\frac{\sqrt{(2/C_k) E_{Ck}}}{\eta_k V_{Tk}}} - 1 \right) \right] d\tau. \quad (15)$$

This relationship can be linearized around a reference value E_{Ckm}^*, i.e.,

$$E_{PVkm} \approx E_{PCkm}^* + \delta_k \left(E_{Ckm} - E_{Ckm}^* \right) \quad (16)$$

where

$$E_{PVkm}^* = E_{PVkm}\left(E_{Ckm}^*\right) \quad \delta_k = \left. \frac{dE_{PVkm}}{dE_{Ckm}} \right|_{E_{Ckm} = E_{Ckm}^*} \quad (17a)$$

and the slope δ_k can be expressed as

$$\delta_k = \frac{T_g (I_{gk} + I_{satk})}{\sqrt{2 C_k E_{Ckm}^*}} - \frac{T_g I_{satk}}{\sqrt{2 C_k E_{Ckm}^*}} \exp\left(\sqrt{\frac{2 E_{Ckm}^*}{C_k \eta_k^2 V_{Tk}^2}} \right) \left(1 + \sqrt{\frac{2 E_{Ckm}^*}{C_k \eta_k^2 V_{Tk}^2}} \right). \quad (17b)$$

Replacing (16) into (14) leads to the following relationship which corresponds to a discrete-time linearized model of the grid-connected PV system:

$$\sum_{k=1}^{n} \left[E_{Ckm} - E_{Ck(m-1)} \right] = \sum_{k=1}^{n} \left[E_{PVkm}^* + \delta_k \left(E_{Ckm} - E_{Ckm}^* \right) \right] - \frac{K_{(m-1)} A^2 T_g}{2}. \quad (18)$$

This model demonstrates that if the energy of each capacitor E_{Ckm} is regulated to the reference value E_{Ckm}^* corresponding to the kth PV array, namely

$$E_{Ckm} = E_{Ck(m-1)} = E_{Ckm}^*, \qquad k = 1, 2, \ldots, n \quad (19)$$

then, according to (13a), (18) collapses to (10), i.e.,

$$\sum_{k=1}^{n} E_{PVkm}^* = \sum_{k=1}^{n} i_{PVk(m-1)}^* v_{Ck(m-1)}^* T_g = \frac{K_{(m-1)} A^2 T_g}{2}. \quad (20)$$

The desired power transfer is thus achieved. It must be pointed out that, since the reference current and voltage values of each PV array are set by the irradiance and temperature operating conditions, the only way to force (20) is by controlling the variable $K_{(m-1)}$. To ensure energy control of all capacitors, a set of n auxiliary variables K_k with $k = 1, \ldots, n$ is defined so that

$$\sum_{k=1}^{n} K_{k(m-1)} = K_{(m-1)} \quad (21)$$

and, in this case, (18) becomes

$$\sum_{k=1}^{n} \left[E_{Ckm} - E_{Ck(m-1)} \right] = \sum_{k=1}^{n} E_{PVkm}^* + \sum_{k=1}^{n} \delta_k \left(E_{Ckm} - E_{Ckm}^* \right) - \sum_{k=1}^{n} \frac{K_{k(m-1)} A^2 T_g}{2}. \quad (22)$$

Therefore, if the dynamics of each bridge is modeled as

$$E_{Ckm} - E_{Ck(m-1)} = E_{PVkm}^* + \delta_k \left(E_{Ckm} - E_{Ckm}^* \right) - \frac{K_{k(m-1)} A^2 T_g}{2}, \qquad k = 1, \ldots, n \quad (23)$$

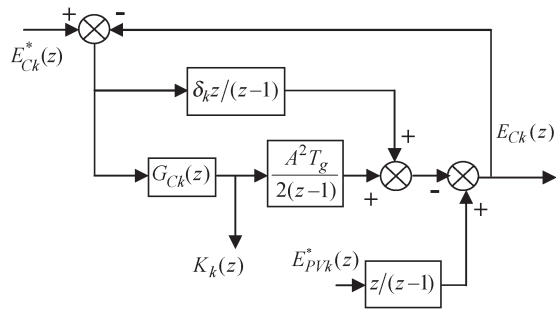

Fig. 2. Block diagram of the energy-balance control for bridge k.

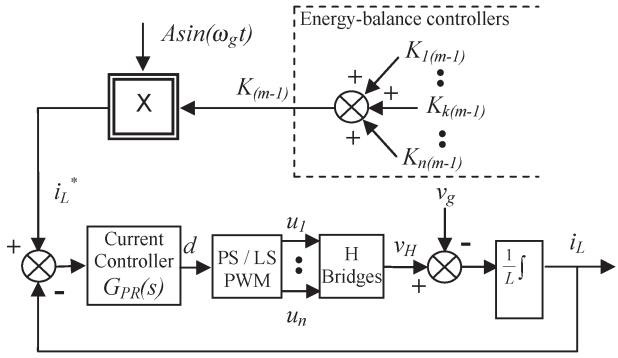

Fig. 3. Block diagram of the current control loop.

the auxiliary variable $K_{k(m-1)}$ can be controlled to set the capacitor energy to its reference value, thus resulting in

$$\frac{K_{k(m-1)}A^2T_g}{2} = E^*_{PVkm}, \qquad k = 1, 2, \ldots, n. \tag{24}$$

It is worth emphasizing that proper control of each auxiliary variable leads to the desired steady state of the overall system given in (20) since, from (21) and (23), it can be written as

$$\sum_{k=1}^{n} \frac{K_{k(m-1)}A^2T_g}{2} = \frac{K_{(m-1)}A^2T_g}{2} = \sum_{k=1}^{n} E^*_{PVkm}. \tag{25}$$

Finally, note that if the reference E^*_{Ckm} is set to the MPP of the PV arrays, the maximum power is transferred to the grid.

One of the main benefits of the previous approach is that a linear discrete-time model of the dynamics of each bridge is obtained. Applying the Z transform to (23) yields

$$E_{Ck}(z) = \left[E^*_{PVk}(z) + \delta_k \left(E_{Ck}(z) - E^*_{Ck}(z)\right)\right] \frac{z}{z-1} - \frac{K_k(z)A^2T_g}{2(z-1)}, \qquad k = 1, 2, \ldots, n. \tag{26}$$

This model allows the design of a linear discrete-time controller $G_{Ck}(z)$ to control the auxiliary variable $K_k(z)$ according to the block diagram derived from (26) and shown in Fig. 2.

This controller is hereafter referred to as the "energy-balance controller" and is designed with the help of the powerful linear control tools in the Z domain to ensure the local stability of the corresponding control loop.

B. Control Design Guidelines for Local Stability

This section presents the main design guidelines for the controllers of the cascaded inverter. A complete design of a laboratory prototype built to experimentally verify the proposed approach is presented in Section V.

1) Energy-Balance Controllers: The energy-balance controller design follows the same approach in [24], which is summarized hereinafter for the sake of completeness.

From the block diagram in Fig. 2, the closed-loop transfer function can be written as

$$E_{Ck}(z) = \frac{zE^*_{PVk}(z) - E^*_{Ck}(z).\left[z\delta_k + 0.5A^2T_gG_{Ck}(z)\right]}{z - 1 - (z\delta_k + 0.5A^2T_gG_{Ck}(z))}.$$

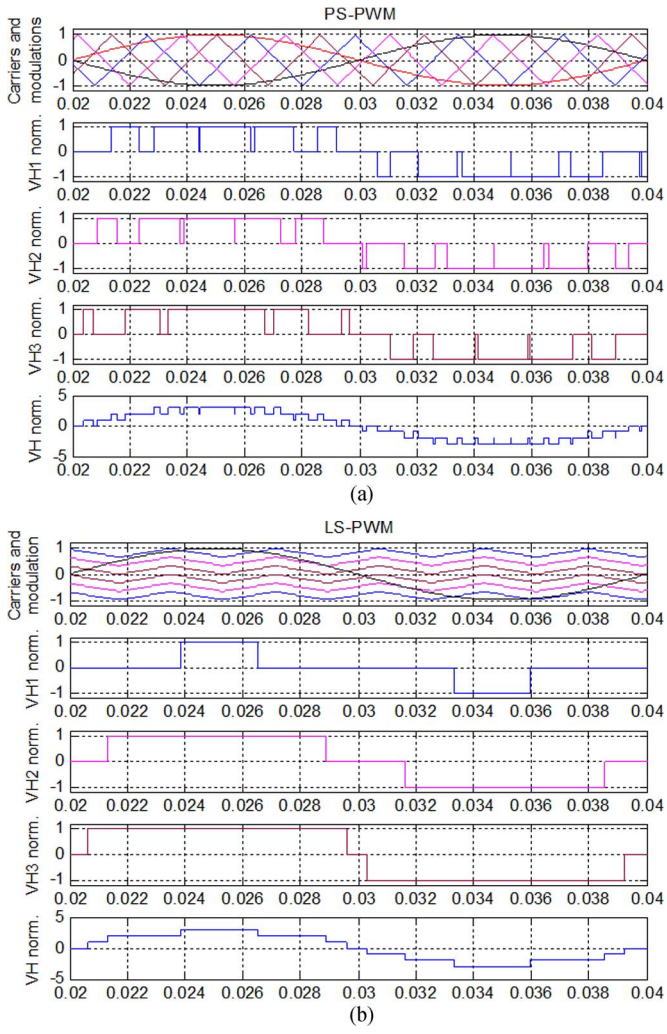

Fig. 4. Resulting voltages for (a) PS-PWM and (b) LS-PWM.

A PI digital controller is chosen to ensure the control of E_{Ck} with zero steady-state error and to fix a desired transient response. Accordingly, $G_{Ck}(z)$ can be written as

$$G_{Ck}(z) = \gamma_k \frac{z - \alpha_k}{z - 1}.$$

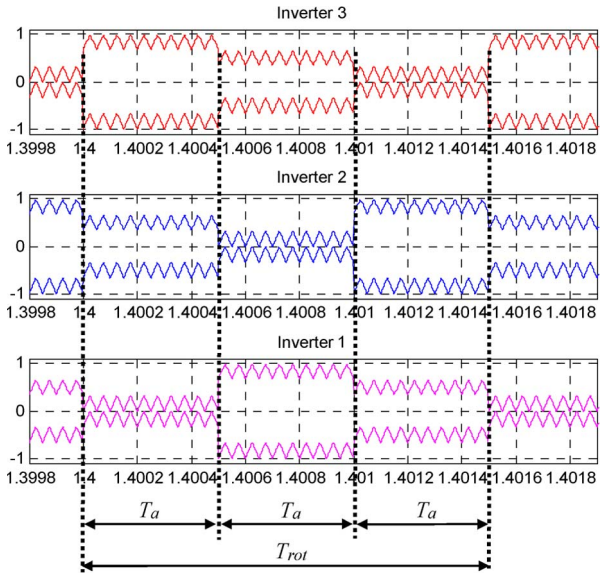

Fig. 5. Inverter rotating carrier assignment for LS-PWM.

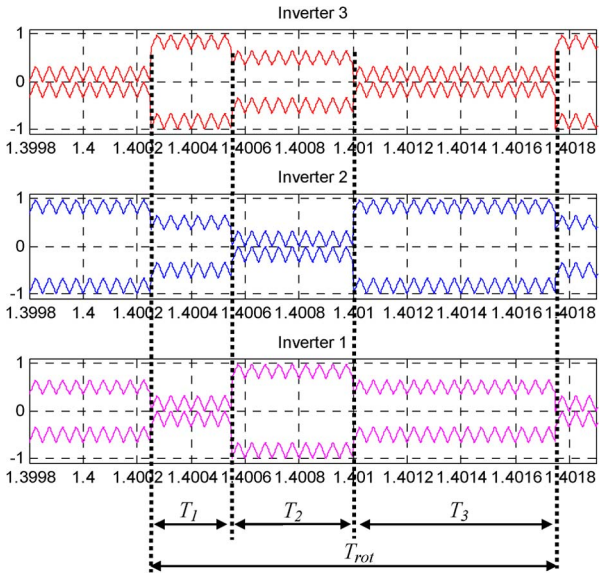

Fig. 7. Modified LS-PWM strategy.

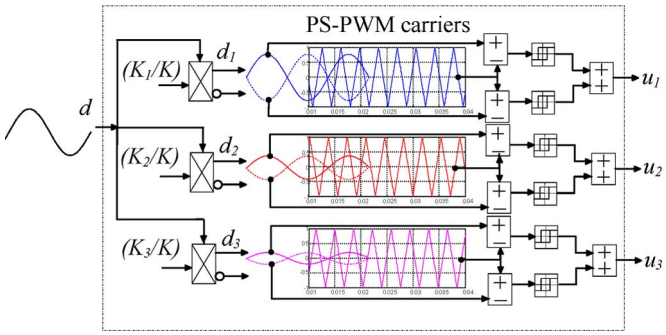

Fig. 6. PS-PWM strategy.

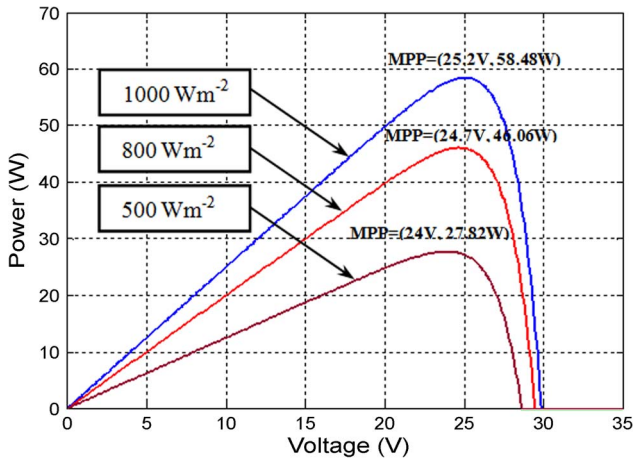

Fig. 8. Power versus voltage curves programmed in the SAS.

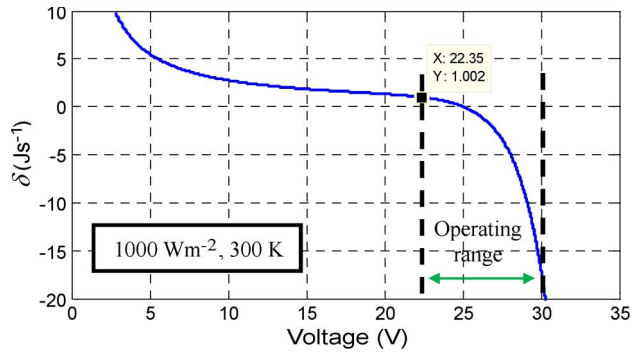

Fig. 9. Evolution of δ_k versus v_{Ck} for a solar irradiance of 1000 W/m^2, $I_g = 3.05$ A, $I_{\rm sat} = 1.35 \cdot 10^{-7}$ A, and $\eta = 1$.

Hence, the closed-loop characteristic equation, noted as $P_k(z)$, results in

$$P_k(z) = (1-\delta_k)z^2 + \left(\delta_k - 2 - \frac{\gamma_k A^2 T_g}{2}\right) z + 1 + \frac{\gamma_k \alpha_k A^2 T_g}{2}. \tag{27}$$

The set of controller parameters γ_k and α_k ensuring the system stability is derived by applying the Jury test to (27), thus yielding the following design restrictions:

$$\begin{cases} \delta_k < 1; \alpha_k < 1; \gamma_k < 0 \\ \frac{4(\delta_k - 2)}{A^2 T_g (1+\alpha_k)} < \gamma_k < \frac{-2\delta_k}{\alpha_k A^2 T_g} \end{cases}. \tag{28}$$

Accordingly, the following design guidelines are adopted.

1) Zero of the controller (α_k) will be located close to the unit circle to compensate the destabilizing effect of the integral action.
2) Controller gain (γ_k) will be adjusted to ensure the stability conditions given in (28).

These restrictions involve the operating conditions of the PV arrays through the parameter δ_k defined in (17b).

2) Current Controller: The energy-balance control approach assumes that the output current i_L has reached the reference i_L^*. This assumption requires the design of a current controller to ensure that i_L tracks the sinusoidal current reference i_L^* given in (9) with a fast transient response and zero steady-state error. The closed-loop dynamics of the inverter can be represented by the block diagram in Fig. 3.

As extensively reported in [26] and [27], a linear PR controller is particularly suitable to track a sinusoidal current

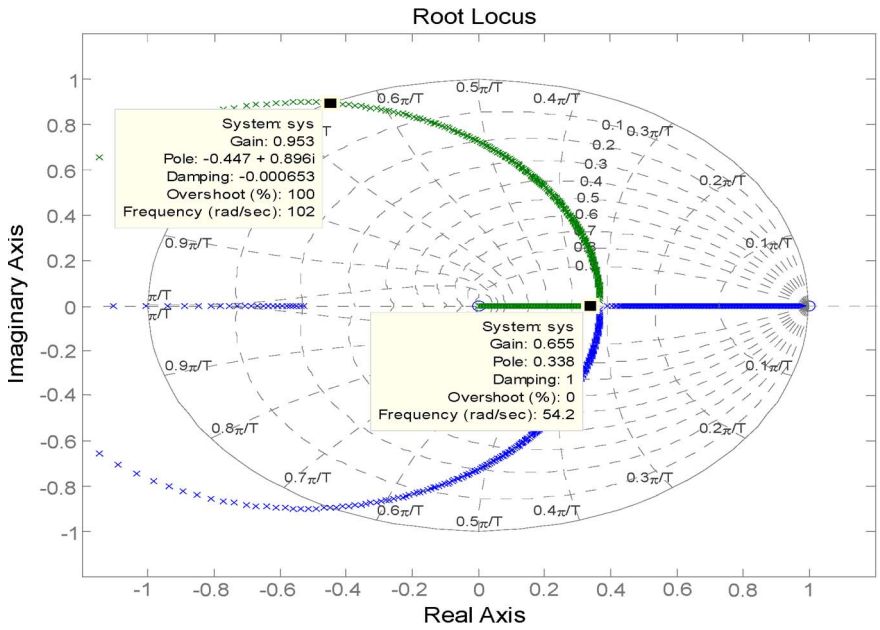

Fig. 10. Root locus for different values of δ_k when $\gamma_k = -0.05$. Variable δ_k is referred to as "gain" in the root locus.

reference. The transfer function of this controller $G_{PR}(s)$ is given by

$$G_{PR}(s) = K_p + \frac{K_i s}{s^2 + \omega_g^2}. \tag{29}$$

By following the design guidelines in [26] and [27], the controller concurrently ensures fast dynamics, zero steady-state error at the tracking frequency, and local stability.

IV. Control Signals for PS-PWM and LS-PWM

The proper operation of the current loop leads to a duty cycle d ensuring the transfer of the overall average dc power to the grid. The last step of the control design is the generation of the control signal of each modulator u_k from the duty cycle d to drive the power handled by each bridge according to the energy balance control. This generation depends on the modulation technique used to build the multilevel output voltage v_H. To show this dependence, Fig. 4 shows the voltages of a three full-bridge cascaded inverter for the particular case of the same input normalized dc voltages when a sinusoidal signal of normalized amplitude is applied to PS-PWM [Fig. 4(a)] and LS-PWM [Fig. 4(b)] modulators operating at the same carrier frequency.

As previously reported in [8], PS-PWM leads to an even power distribution among the inverters but to an uneven distribution if LS-PWM is applied, as it can be seen from the output voltage plot of each bridge [v_{H1}, v_{H2}, and v_{H3} in Fig. 4(a) and (b)]. However, the work of Angulo *et al.* [33] modifies the LS-PWM strategy by introducing the concept of "rotating carrier" which allows the power balance by modifying the carrier assigned to each inverter over time. This concept periodically assigns to each inverter (with a period $T_{\rm rot}$) the carriers of different shifted levels according to the sequence in Fig. 5, during the same time interval T_a. It is worth noting that achieving power balance requires both the sequence in Fig. 5 and the same time interval assignment.

TABLE I
Design Parameters of the PV Inverter

Power stage	*MOSFET/drivers*	*IRFP240 /IR21084*
	C1 = C2 = C3	*2.2 mF*
	L	*950 μH*
Grid Voltage	*Transf. (20:3)*	*33V_{RMS} / 50 Hz*
Panels	*SAS Agilent*	*E4350B#J02*
Energy-balance controllers(FPGA)	*γ_k*	*-0.05*
	α_k	*0.875*
Current controller (FPGA)	*K_p*	*140*
	K_i	*50000*
Carrier frequency	*f_c*	*19.5 kHz*
Rotating period(LS-PWM)	*T_{rot}*	*2.15 ms*

In contrast, the case under study requires an unbalanced power distribution among the inverters to deal with different operating conditions of the PV arrays: The previous strategies must therefore be modified to make sure that each inverter handles the power of its corresponding PV array.

This modification is based on the fact that both the overall power handled by the cascaded inverter and its distribution among the inverter cells can be known from the auxiliary control variables K_k applying (23) and (25). Accordingly, the PS- and LS-PWM strategies are modified as follows.

1) PS-PWM: The duty cycle d_k of inverter k is computed as

$$d_k = \frac{K_k}{\sum_{k=1}^{n} K_k} d = \frac{K_k}{K} d. \tag{30}$$

The PS-PWM and the corresponding control signals are shown in Fig. 6 for the case of three inverters.

2) LS-PWM: For level-shifted modulation, the control design takes advantage of the rotating carrier concept and applies the same rotating carrier assignment to each

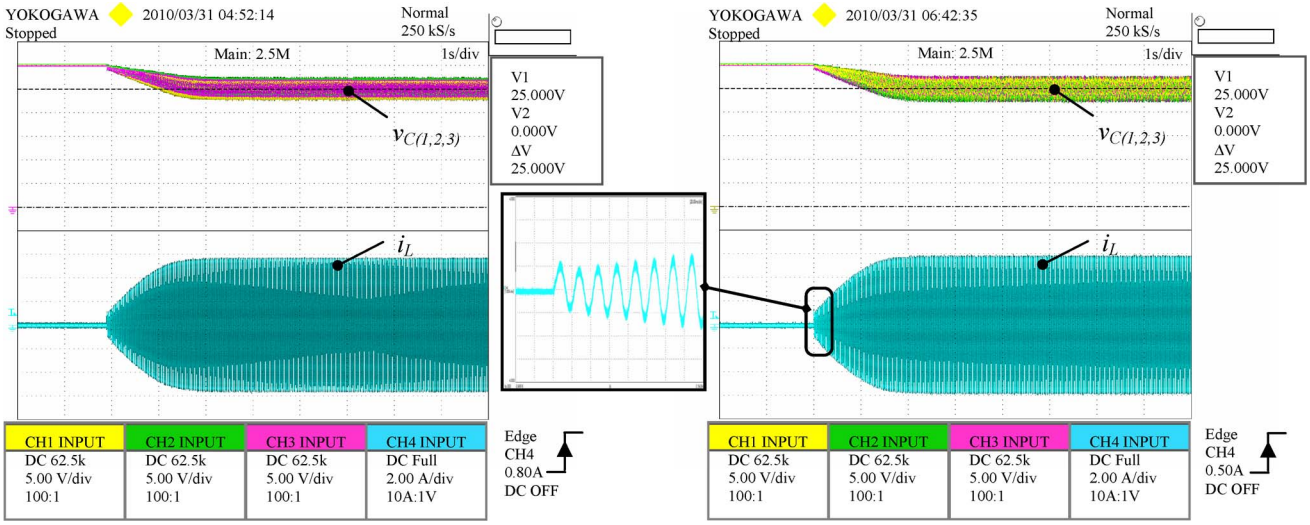

Fig. 11. Start-up behavior of inductor current (i_L) and capacitor voltages (v_{C1}, v_{C2}, and v_{C3}) for both (left) PS-PWM and (right) LS-PWM.

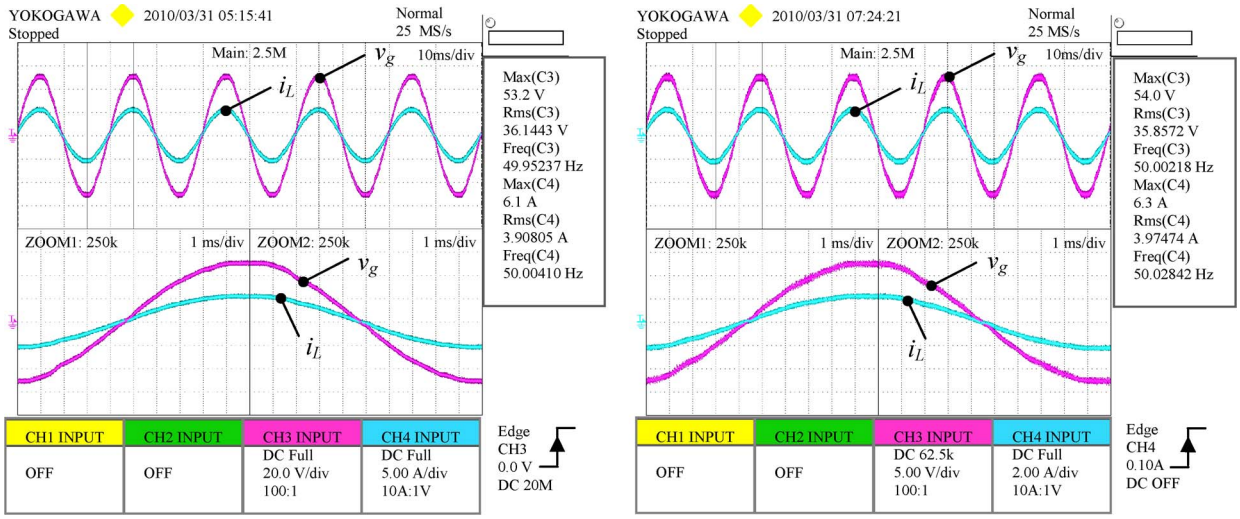

Fig. 12. Steady-state primary transformer voltage and injected current (i_L) for both (left) PS-PWM and (right) LS-PWM.

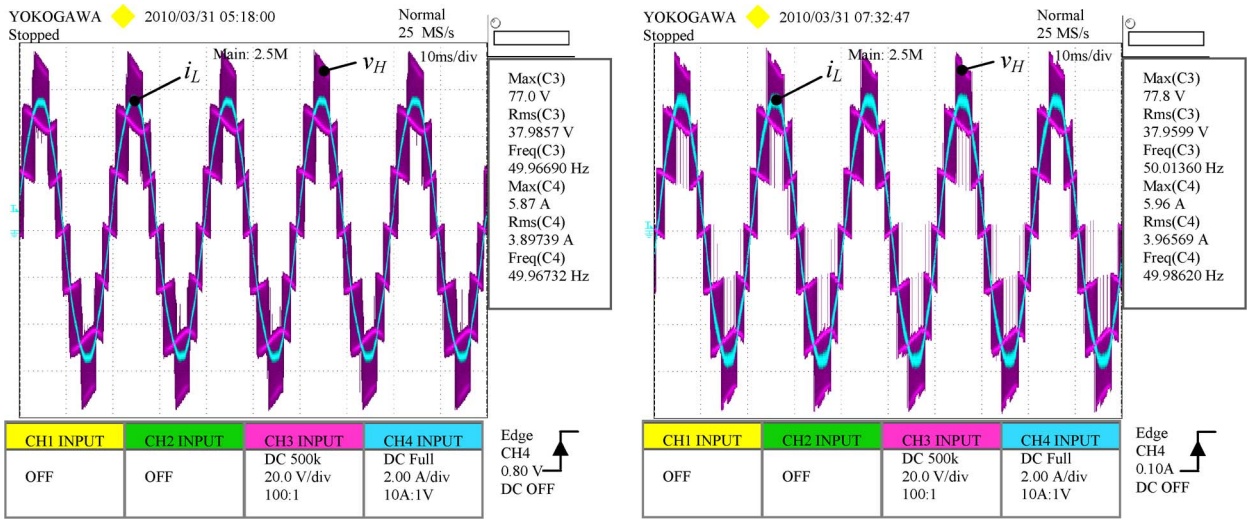

Fig. 13. Steady-state output voltage of the multilevel converter (v_H) and injected current (i_L) for both (left) PS-PWM and (right) LS-PWM.

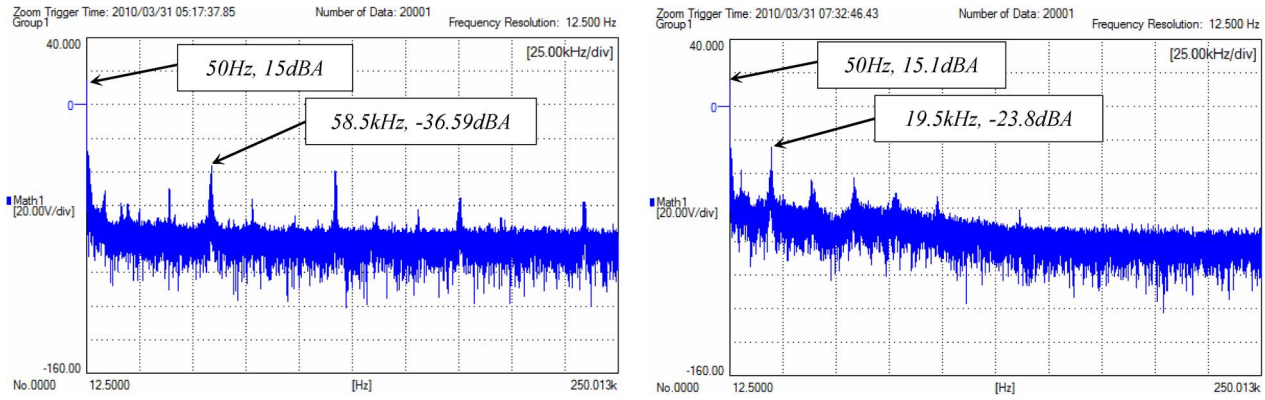

Fig. 14. Spectrum of the inductor current of the multilevel converter. (Left) PS-PWM. (Right) LS-PWM.

inverter as in Fig. 5, but the time during which this assignment prevails is modified as

$$T_k = \frac{K_k}{\sum_{k=1}^{n} K_k} T_{\rm rot} = \frac{K_k}{K} T_{\rm rot}. \tag{31}$$

The resulting assignment is shown in Fig. 7 for the case of three inverters.

V. Experimental Validation

A laboratory prototype of a grid-connected PV multilevel inverter, including three cascaded inverter cells, was built to experimentally verify the proposed approach. The energy-balance and current controllers described in Section III were implemented in a field-programmable gate array (FPGA, Xilinx Spartan 3). The FPGA was used to generate the PS-PWM carriers and the rotating carriers of the LS-PWM addressed in Section IV. It must be pointed out that the voltage references v_{Ck}^* (see Fig. 1) were externally set since no MPPT algorithm was implemented because of its slow dynamics compared to that of the PV inverter. Nevertheless, an MPPT algorithm emulation was included in the tests. The experimental setup is described in the following sections.

A. Power Stage and PV Arrays

All the full-bridge switches were built by means of IRFP240 MOSFETs controlled by IR21084 drivers. The reactive components of the power stage were set to $C_1 = C_2 = C_3 = 2.2$ mF for the input capacitors and to $L = 950$ μH for the output filter inductance. Three solar array simulators (SASs) (Agilent E4350B #J02) were also used to emulate the electrical behavior of the PV arrays. The power versus voltage curves programmed in each SAS, which correspond to three different solar incident irradiances, are shown in Fig. 8. The SASs were controlled through a GPIB bus using auxiliary software to allow the emulation of step irradiance changes.

Since the maximum SAS open circuit voltage is of 86 V, the multilevel inverter prototype was connected to the single-phase grid through a step-up power transformer of 20:3 turns ratio. This resulted in a grid voltage amplitude of 33 $V_{\rm RMS}$ and a frequency of 50 Hz at the transformer primary side. Therefore, the values of A and T_g were set to $A = 33\sqrt{2}$ V and $T_g = 20$ ms.

TABLE II
Quality Indices for PS- and LS-PWMs

INDEX	PS-PWM	LS-PWM
THD (%)	1,79%	1,95%
Efficiency (η%)	≈ 86%	≈ 86,8%
Cos(φ)	≈ 1	≈ 1

B. Control Design

1) Energy-Balance Controllers: The same energy-balance controller, referred to as $G_C(z)$, was designed for the three arrays. The following design procedure assumes the worst operating case to ensure system stability over a wide range of operation.

As pointed out in Section III-B1, parameter α_k must be set to a value close to one to mitigate the instability effect of the integral component of G_C. Therefore, to focus on the selection of the parameter γ_k, α_k is fixed to 0.875.

The design of the controller gains (γ_k) is constrained by the stability conditions of (28) which depend on parameter δ_k. Moreover, the expression of δ_k given in (17b) must fulfill the stability restriction $\delta_k < 1$ for the whole range of irradiances under which the PV array operates. The worst case corresponds to the maximum irradiance value. Note from (17b) that this restriction leads to the operating range of the array voltage (v_{Ck}) (i.e., of the capacitor stored energy E_{Ck}) ensuring the system stability under this irradiance. This range can be evaluated by a numerical simulation of δ_k versus v_{Ck}, as shown in Fig. 9, for an irradiance of 1000 W/m^2 and the parameters previously defined. As can be seen, the lower voltage limit of 22.35 V is reached when $\delta_k = 1$, while the upper one of 30 V corresponds to the open circuit voltage of the PV array.

In addition, (28) constrains the values of γ_k in terms of the parameter δ_k. Setting $\delta_k = 0.9$ to ensure the condition $\delta_k < 1$, the values of parameter γ_k ensuring system stability are constrained to $-0.053 < \gamma_k < -0.047$. It can be proved that a value of $\gamma_k = -0.05$ assures system stability for a sufficiently wide operating range.

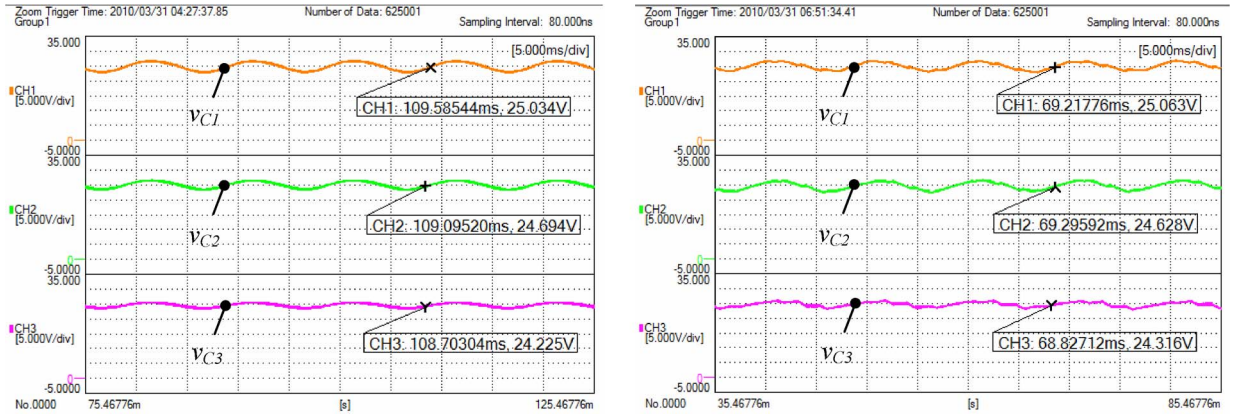

Fig. 15. Zoom of the capacitor voltages. (Left) PS-PWM. (Right) LS-PWM.

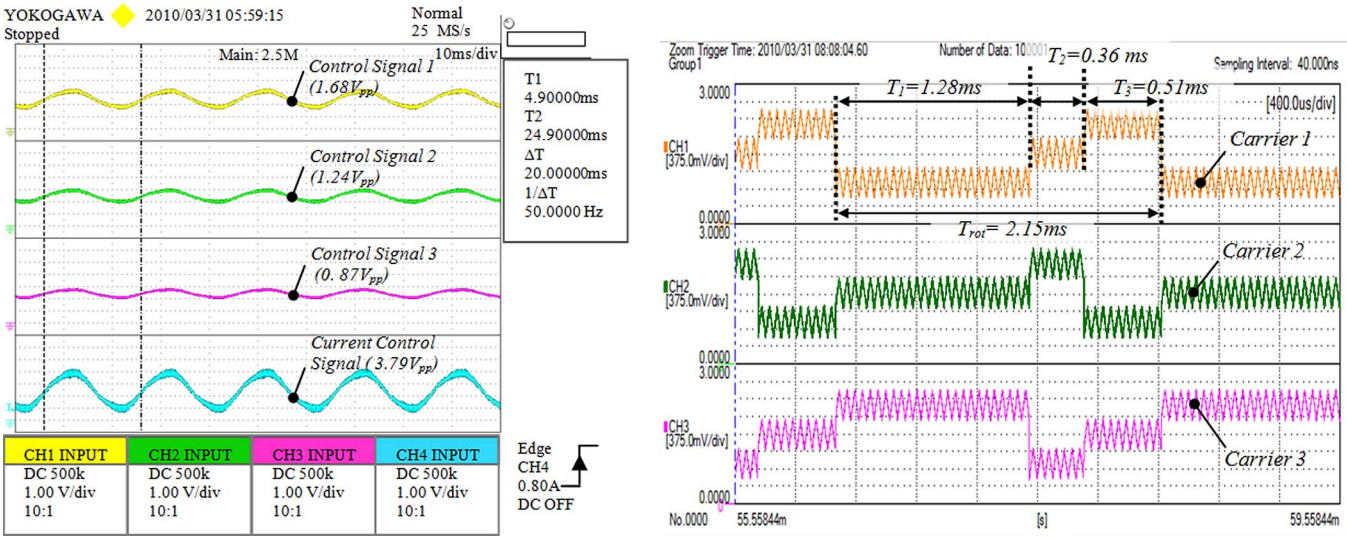

Fig. 16. (Left) Steady-state PS-PWM control signals. (Right) Zoom of steady-state LS-PWM sequence assignation.

Fig. 10 shows the root locus of the system in terms of δ_k [see (27)] for a fixed controller gain of $\gamma_k = -0.05$ and an irradiance of 1000 W/m^2. The plot confirms the stability prediction, and the system response is stable for $\delta_k < 0.953$ (or, equivalently, for a voltage $v_{Ck} > 22.59$ V). This stability condition requires that both capacitor voltage and voltage reference given by the MPPT algorithm remain within these limits at any time. Otherwise, the capacitor is precharged near the open circuit voltage of the PV array and regulated to an arbitrary voltage value falling within the stability limits. A partially or totally shaded panel will operate at the voltage arbitrarily fixed by the reference value if its natural operation falls out of the stability limits, as in the case of PV array voltage drop when bypass diodes are turned on.

2) Current Controller: Following the design procedure given in [26] and [27], the PR-controller parameters were fixed to $K_p = 140$ and $K_i = 50000$ to obtain a fast transient response and zero tracking error at the grid frequency.

3) Modulation Parameters: This paper assumed the same value of the carrier frequencies in order to further make a coherent comparison in terms of harmonic distortion and overall efficiency for both modulations. The choice of the carrier frequency must take into account that the energy-balance control design is valid as long as the capacitor voltage remains within the validity range of the PV array linearized model. Note that, since the number of switching events per grid period is higher in PS-PWM (see Fig. 4), the capacitor voltage dynamics is better controlled under this modulation. Accordingly, the carrier frequency must be designed for the LS-PWM case to ensure a number of switching events high enough to control the capacitor voltage within the validity range of the PV array linearized model. In this concern, the following criteria have been adopted.

1) A proper energy balance between the different inverter cells and the power delivered to the grid requires a minimum number of carrier rotations per grid period. The case under study has considered nine rotations per grid period, with this number being a multiple of the number

TABLE III
IRRADIANCE PATTERNS FOR EACH ARRAY

Irradiance (W/m^2)	*Time interval (s)*			
	0 ≤t<1.6	*1.6 ≤t<5.2*	*5.2 ≤t<7.2*	*7.2 ≤t<10*
Irrad$_1$	*1000*	*800*	*800*	*800*
Irrad$_2$	*1000*	*1000*	*800*	*800*
Irrad$_3$	*1000*	*1000*	*1000*	*800*

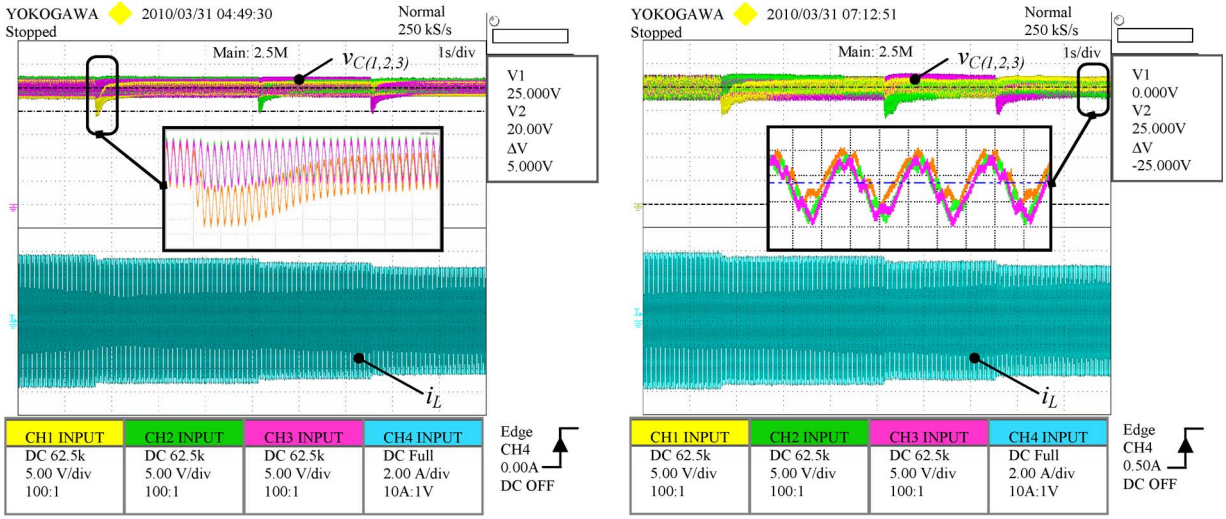

Fig. 17. Irradiance change. Inductor current (i_L) and capacitor voltages (v_{C1}, v_{C2}, and v_{C3}) for both (left) PS-PWM and (right) LS-PWM.

of inverter cells. Hence, the rotating carrier period is $T_{\rm rot} = 2.2$ ms, which has been finally adjusted to $T_{\rm rot} = 2.15$ ms.

2) The number of carrier cycles during a rotation period must be high enough to preserve an acceptable resolution of the control action (i.e., the number of switching events) for any operating conditions of the PV arrays. In particular, as evidenced in Figs. 7 and 16, the resolution is compromised when, according to (31), the lowest number of carrier cycles is assigned to the cell handling the lowest power. The case under study has adopted 42 carrier cycles per rotating period to ensure an acceptable control action resolution for irradiances ranging from 500 to 1000 W/m^2. Moreover, since this value is a multiple of the number of inverter cells, when all the PV arrays operate under the same irradiance, the same number of cycles, namely, $42/3 = 14$ cycles, is assigned to each inverter cell. On the other hand, each of the six carriers required in LS-PWM for the present design has been implemented into the FPGA by means of 512 levels, thus finally leading to the following carrier frequency value:

$$f_{\rm carrier} = \frac{1}{2 \cdot A_{\rm carrier} \cdot div_{\rm clk} \cdot T_{\rm clk200\ MHz}} = \frac{1}{2 \cdot 512 \cdot 10 \cdot 5 \cdot 10^{-9}} = 19\,531\ \text{Hz}$$

where

$A_{\rm carrier}$ number of levels/carrier $= 512$;
$div_{\rm clk}$ scaling factor of the FPGA clock signal $= 10$;
$T_{\rm clk200\ MHz}$ FPGA clock period $= 5$ ns.

C. Experimental Results

A series of experimental tests was carried out to validate the proposed control approach. The design parameters of the experimental setup are presented in Table I.

TABLE IV
VOLTAGE PATTERNS FOR MPPT EMULATION

	Reference Voltage (V)		
	0s ≤t<1.8s	*1.8s ≤t<6.4s*	*6.4s ≤t<10s*
v_{C1}^*	25	28	25
v_{C2}^*	25	28	25
v_{C3}^*	25	28	25

TABLE V
VOLTAGE PATTERNS FOR MPPT EMULATION

	Reference Voltage (V)	
	0s ≤t<3s	*3s ≤t<10s*
v_{C1}^*	25	28
v_{C2}^*	25	25
v_{C3}^*	25	23

Test 1—Start-Up and Steady-State Behavior Under Uniform Irradiance: The same power versus voltage curve corresponding to an irradiance of 1000 W/m^2 (see Fig. 8) was programmed in the three SASs, and the reference voltages were set to $v_{C1}^* = v_{C2}^* = v_{C3}^* = 25$ V. Fig. 11 shows the start-up behavior of the inductor current (i_L) and the capacitor voltages (v_{C1}, v_{C2}, and v_{C3}) for PS-PWM (left) and LS-PWM (right). As can be seen, the voltages evolve from the PV array open circuit voltages (30 V) to the reference ones, and the transient response of the injected current is smooth. Fig. 12 shows the primary transformer voltage and the injected current (i_L) in steady state. Note that the output current is always in phase with the grid voltage. Fig. 13 shows the output voltage of the multilevel converter (v_H) and confirms that both modulations operate with seven levels, as expected. Fig. 13 also shows the injected current (i_L) and evidences a greater current amplitude ripple for LS-PWM. This is due to the different switching patterns of PS and LS modulations as confirmed by the spectrum of the injected current in Fig. 14: Note how the first harmonic is located either at the carrier frequency (19.5 kHz) for LS-PWM or at three times the carrier frequency (58.5 kHz) for PS-PWM.

Moreover, THD, efficiency, and displacement factor (i.e., phase shift φ between grid current and voltage) can also be extracted from these experimental results and are reported in Table II for both modulations.

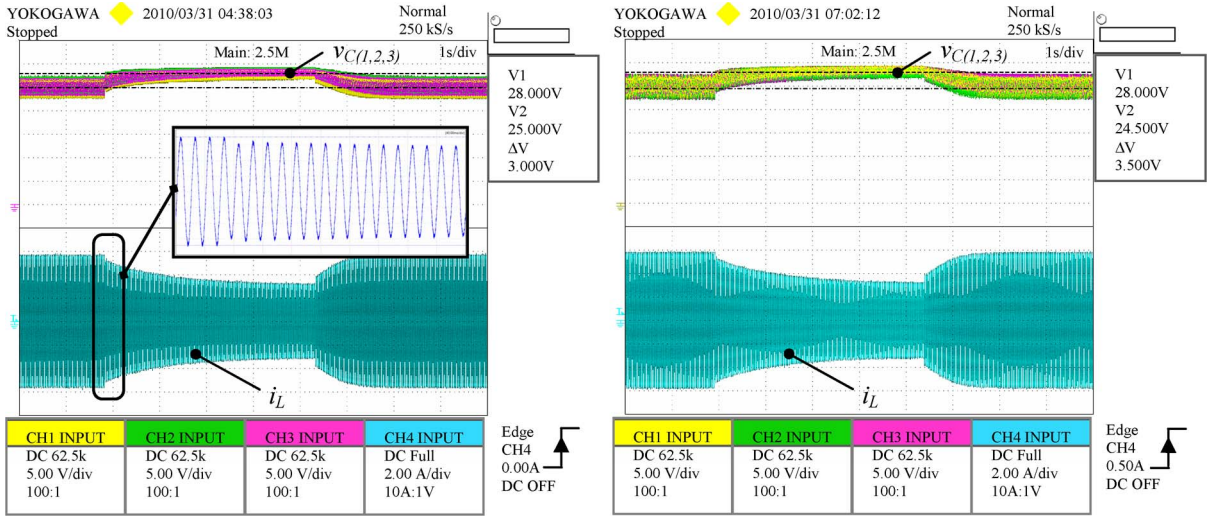

Fig. 18. Capacitor voltage regulation. Inductor current (i_L) and capacitor voltages (v_{C1}, v_{C2}, and v_{C3}) for both (left) PS-PWM and (right) LS-PWM.

These results suggest that, under the same carrier frequency operation, both modulations exhibit an excellent displacement factor, thus confirming the proper operation of the PR current controller. In addition, LS-PWM leads to better efficiency but worse THD than PS-PWM, thus being attributable to the different switching patterns of both modulations. On the other hand, an FPGA-based design operating at a lower switching frequency to reduce switching losses would be envisaged for the PS-PWM case but would result more difficult if LS-PWM is adopted since the lowest switching frequency is limited by both the ratio rotating frequency/grid frequency and the control action resolution supported by the FPGA platform, as detailed in Section V-B3.

Test 2—Steady-State Behavior Under Nonuniform Irradiance: In this test, the SASs were programmed to emulate a system operation under three different irradiances, namely, 1000, 800, and 500 W/m^2, and the reference voltages were set to their MPP values, i.e., $v^*_{C1} = 25.2$ V, $v^*_{C2} = 24.7$ V, and $v^*_{C3} = 24$ V (see Fig. 8). Fig. 15 shows a zoom of the steady-state capacitor voltages and confirms that they have reached their reference values. Since each inverter handles a different power, the control values delivered by the energy-balance controllers (K_k) were different, thus leading to different duty cycles in PS-PWM [see (30)] or different time interval assignation in LS-PWM [see (31)]. Fig. 16 shows a scaled version of the control signals internally generated by the FPGA for both modulations. As it can be seen in Fig. 16 (left), inverters handling higher input power are driven by control signals of higher amplitude, in accordance with (30). Similarly, in Fig. 16 (right), higher time intervals are assigned to inverters handling higher power, in accordance with (31).

Test 3—Robustness to Irradiance Changes: As can be deduced from Fig. 2, the input E^*_{PVk} (i.e., the energy of the PV array k) can be considered as a perturbation of E_{Ck} (i.e., the voltage of capacitor C_k). To check the robustness of the energy-balance control, the SASs were programmed to emulate an abrupt irradiance change according to the pattern in Table III, and the reference voltage values were held at $v^*_{C1} = v^*_{C2} = v^*_{C3} = 25$ V. Fig. 17 shows the evolution of the capacitor voltages (v_{C1}, v_{C2}, and v_{C3}) and the injected current (i_L). Note that, after a small transient response, the voltage across the capacitors maintains its reference value, thus confirming a proper voltage regulation in the presence of irradiance changes.

Test 4—MPPT Emulation: The following two tests aimed to emulate an MPPT algorithm by varying the reference capacitor voltages. In the first test, all reference voltages were fixed at the same value which changed according to the pattern in Table IV. In the second one, the reference voltages simultaneously varied to different reference values following the pattern in Table V.

Figs. 18 and 19 show the output current and the capacitor voltages for both tests and both modulations. As it can be seen, the capacitor voltages follow their respective voltage references after a short transient response, validating the proposed control approach.

VI. Conclusion

This paper has addressed the control design of a CHB-MLI grid-connected PV system which can operate under PS- or LS-PWM. The energy-balance model of the system and the linearization of the PV array electrical characteristics allow the design of discrete-time PI linear voltage controllers ensuring independent control of PV arrays operation. This design, which can be easily carried out by conventional discrete-time linear control techniques, takes into account the stability restrictions given by the Jury test which depend on the operating points of the PV arrays. In contrast to other works, the obtained criteria to choose the parameters of the controllers are one of the features of the proposed approach, since they ensure system stability for the whole operating range of the PV arrays in terms of irradiance and temperature. Furthermore, the definition of a set of auxiliary control variables allows the synthesis of the control signals driving each bridge not only for PS-PWM but also for LS-PWM by modifying the rotating carrier concept.

A set of laboratory tests carried out on a seven-level CHB-MLI grid-connected PV system has experimentally validated the proper operation of the energy-balance control for both modulations under uniform and nonuniform irradiances as well

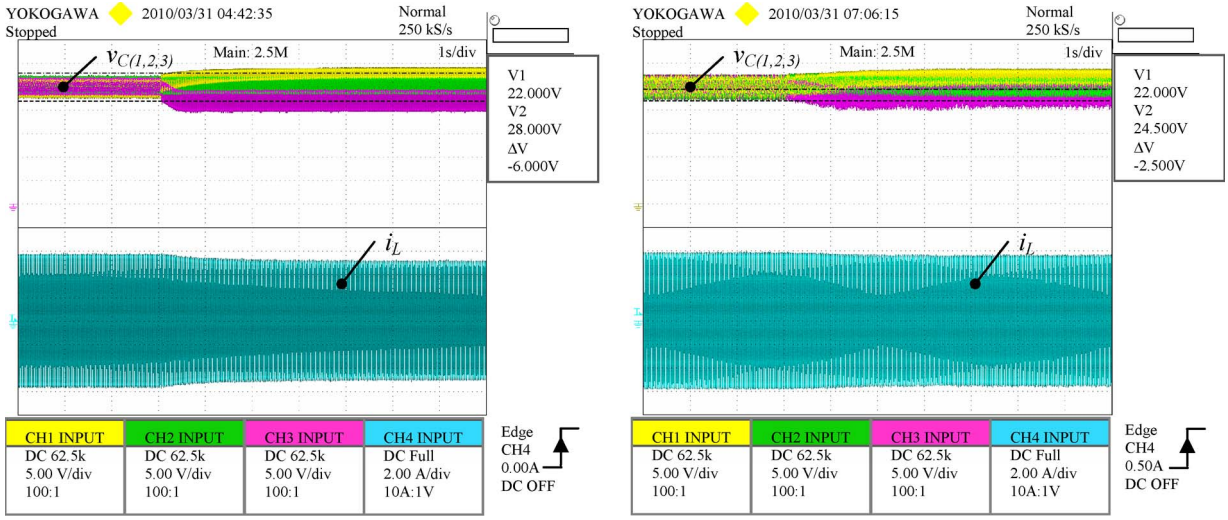

Fig. 19. Capacitor voltage regulation. Inductor current (i_L) and capacitor voltages (v_{C1}, v_{C2}, and v_{C3}) for both (left) PS-PWM and (right) LS-PWM.

as under abrupt irradiance and MPPT algorithm changes. Moreover, these results have also shown that LS-PWM leads to worse THD but better efficiency than PS-PWM. In this regard, an FPGA-based design operating at a lower switching frequency to reduce switching losses would be envisaged for the PS-PWM case but would result more difficult if LS-PWM is adopted since the lowest switching frequency is limited by both the ratio rotating frequency/grid frequency and the control action resolution supported by the FPGA platform.

REFERENCES

[1] G. Petrone, G. Spagnuolo, R. Teodorescu, M. Veerachary, and M. Vitelli, "Reliability issues in photovoltaic power processing systems," *IEEE Trans. Ind. Electron.*, vol. 55, no. 7, pp. 2569–2580, Jul. 2008.

[2] M. Calais, J. Myrzik, T. Spooner, and V. G. Agelidis, "Inverter for single-phase grid connected photovoltaic systems—An overview," in *Proc. Power Electron. Spec. Conf.*, Feb. 2002, vol. 4, pp. 1995–2000.

[3] S. B. Kjaer, J. K. Pedersen, and F. Blaabjerg, "A review of single-phase grid-connected inverters for photovoltaic modules," *IEEE Trans. Ind. Appl.*, vol. 41, no. 5, pp. 1292–1306, Sep./Oct. 2005.

[4] M. Meinhardt and G. Cramer, "Multi-string converter: The next step in evolution of string-converter technology," in *Proc. 9th Eur. Conf. Power Electron. Appl.*, Graz, Austria, 2001.

[5] G. R. Walker and P. C. Sernia, "Cascaded dc/dc converter connection of photovoltaic modules," *IEEE Trans. Power Electron.*, vol. 19, no. 4, pp. 1130–1139, Jul. 2004.

[6] J.-M. Kwon, B.-H. Kwon, and K.-H. Nam, "Grid-connected photovoltaic multistring PCS With PV current variation reduction control," *IEEE Trans. Ind. Electron.*, vol. 56, no. 11, pp. 4381–4388, Nov. 2009.

[7] S. Daher, J. Schmid, and F. L. M. Antunes, "Multilevel inverter topologies for stand-alone PV systems," *IEEE Trans. Ind. Electron.*, vol. 55, no. 7, pp. 2703–2712, Jul. 2008.

[8] M. Malinowski, K. Gopakumar, J. Rodriguez, and M. A. Pérez, "A survey on cascaded multilevel inverters," *IEEE Trans. Ind. Electron.*, vol. 57, no. 7, pp. 2197–2206, Jul. 2010.

[9] M. Calais, V. G. Agelidis, and M. Meinhardt, "Multilevel converter for single-phase grid-connected photovoltaic systems: An overview," *Sol. Energy*, vol. 66, no. 5, pp. 325–335, Aug. 1999.

[10] J. Rodríguez, J. S. Lai, and F. Z. Peng, "Multilevel inverters: A survey of topologies, controls and applications," *IEEE Trans. Ind. Electron.*, vol. 49, no. 4, pp. 724–738, Aug. 2002.

[11] L. G. Franquelo, J. Rodriguez, J. I. Leon, S. Kouro, R. Portillo, and M. A. M. Prats, "The age of multilevel converters arrives," *IEEE Ind. Electron. Mag.*, vol. 2, no. 2, pp. 28–39, Jun. 2008.

[12] C. Cecati, F. Ciancetta, and P. Siano, "A multilevel inverter for photovoltaic systems with fuzzy logic control," *IEEE Trans. Ind. Electron.*, vol. 57, no. 12, pp. 4115–4125, Dec. 2010.

[13] S. Busquets-Monge, J. Rocabert, P. Rodriguez, S. Alepuz, and J. Bordonau, "Multilevel diode-clamped converter for photovoltaic generators with independent voltage control of each solar array," *IEEE Trans. Ind. Electron.*, vol. 55, no. 7, pp. 2713–2723, Jul. 2008.

[14] G. Grandi, C. Rossi, D. Ostojic, and D. Casadei, "A new multilevel conversion structure for grid-connected PV applications," *IEEE Trans. Ind. Electron.*, vol. 56, no. 11, pp. 4416–4426, Nov. 2009.

[15] O. Alonso, P. Sanchis, E. Gubía, and L. Marroyo, "Cascade H-bridge multilevel converter for grid connected photovoltaic generators with independent maximum power point tracking of each solar array," in *Proc. IEEE Power Electron. Spec. Conf.*, 2003, pp. 731–735.

[16] E. Villanueva, P. Correa, J. Rodríguez, and M. Pacas, "Control of a single-phase cascaded H-bridge multilevel inverter for grid-connected photovoltaic systems," *IEEE Trans. Ind. Electron.*, vol. 56, no. 11, pp. 4399–4406, Nov. 2009.

[17] J. Selvaraj and N. A. Rahim, "Multilevel inverter for grid-connected PV system employing digital PI controller," *IEEE Trans. Ind. Electron.*, vol. 56, no. 1, pp. 149–158, Jan. 2009.

[18] J. J. Negroni, D. Biel, F. Guinjoan, and C. Meza, "Energy-balance and sliding mode control strategies of a cascade H-bridge multilevel converter for grid-connected PV systems," in *Proc. IEEE Int. Conf. Ind. Technol.*, 2010, pp. 1155–1160.

[19] J. J. Negroni, F. Guinjoan, C. Meza, D. Biel, and P. Sanchis, "Energy-sampled data modeling of a cascade H-bridge multilevel converter for grid-connected PV systems," in *Proc. 10th IEEE Int. Power Electron. Congr.*, 2006, pp. 1–6.

[20] Y. Liu, H. Hong, and A. Q. Huang, "Real-time algorithm for minimizing THD in multilevel inverters with unequal or varying voltage steps under staircase modulation," *IEEE Trans. Ind. Electron.*, vol. 56, no. 6, pp. 2249–2258, Jun. 2009.

[21] B. P. McGrath and D. G. Holmes, "Multicarrier PWM strategies for multilevel inverters," *IEEE Trans. Ind. Electron.*, vol. 49, no. 4, pp. 858–867, Aug. 2002.

[22] W. H. Lau, B. Zhou, and H. S. H. Chung, "Compact analytical solutions for determining the spectral characteristics of multicarrier-based multilevel PWM," *IEEE Trans. Circuits Syst. I, Reg. Papers*, vol. 51, no. 8, pp. 1577–1585, Aug. 2004.

[23] A. Dell'Aquila, M. Liserre, V. Monopoli, and P. Rotondo, "Overview of pi-based solutions for the control of dc buses of a single-phase H-bridge multilevel active rectifier," *IEEE Trans. Ind. Appl.*, vol. 44, no. 3, pp. 857–866, May/Jun. 2008.

[24] C. Meza, J. J. Negroni, D. Biel, and F. Guinjoan, "Energy-balance modeling and discrete control for single-phase grid-connected PV central inverters," *IEEE Trans. Ind. Electron.*, vol. 55, no. 7, pp. 2734–2743, Jul. 2008.

[25] R. Gupta, A. Ghosh, and A. Joshi, "Multiband hysteresis modulation and switching characterization for sliding-mode-controlled cascaded multilevel inverter," *IEEE Trans. Ind. Electron.*, vol. 57, no. 7, pp. 2344–2353, Jul. 2010.

[26] R. Teodorescu, F. Blaabjerg, M. Liserre, and P. C. Loh, "Proportional-resonant controllers and filters for grid-connected voltage source

converters," *Proc. Inst. Elect. Eng.—Elect. Appl.*, vol. 153, no. 5, pp. 750–762, Sep. 2006.
[27] D. N. Zmood and D. G. Holmes, "Stationary frame current regulation of PWM inverters with zero steady-state error," *IEEE Trans. Power Electron.*, vol. 18, no. 3, pp. 814–822, May 2003.
[28] M. B. Prince, "Silicon solar energy converters," *J. Appl. Phys.*, vol. 26, no. 5, pp. 534–540, May 1955.
[29] G. Petrone, G. Spagnuolo, and M. Vitelli, "A multivariable perturb-and-observe maximum power point tracking technique applied to a single-stage photovoltaic inverter," *IEEE Trans. Ind. Electron.*, vol. 58, no. 1, pp. 76–84, Jan. 2011.
[30] J. Kassakian, M. Schlecht, and G. Verghese, *Principles of Power Electronics*. Norwell, MA: Addison-Wesley, 1991, pp. 395–399.
[31] K. Mahabir, G. Verghese, V. J. Thottuvelli, and A. Heyman, "Linear averaged and sampled data models for large signal control of high power factor ac-dc converters," in *Power Electron. Spec. Conf. Rec.*, 1990, pp. 291–299.
[32] A. H. Mitwalli, S. B. Leeb, G. C. Verghese, and V. J. Thottuvelil, "An adaptive digital controller for a unity power factor converter," *IEEE Trans. Power Electron.*, vol. 11, no. 2, pp. 374–382, Mar. 1996.
[33] M. Angulo, P. Lezana, S. Kouro, J. Rodriguez, and B. Wu, "Level-shifted PWM for cascaded multilevel inverters with even power distribution," in *Proc. IEEE Power Electron. Spec. Conf.*, 2007, pp. 2373–2378.

Javier Chavarría was born in Tortosa, Spain, in 1978. He received the B.S. degree in technical telecommunications engineering and the M.S. and Master degrees in electronics engineering from the Universitat Politècnica de Catalunya (UPC), Barcelona, Spain, in 2001 and 2010, respectively, where he is currently working toward the Ph.D. degree with research on power electronics.

He was a Researcher with the Department of Electronic Engineering, Escola Politècnica Superior d'Enginyeria de Vilanova i la Geltrú, Spain. From 2001 to 2002, he was with CITCEA, UPC. From 2002 to 2011, he was a Hardware Engineer with SONY design department, Barcelona. Since 2011, he has been an R&D Senior Electrical Engineer with Idneo Technologies S.L., Barcelona.

Mr. Chavarria is a collegiate member of the Spanish Official College of Technical Telecommunications Engineers (COITT), from which he won two prizes in 2001 and 2002, respectively.

Domingo Biel (S'97–M'99) received the B.S., M.S., and Ph.D. degrees in telecommunications engineering from the Technical University of Catalonia, Barcelona, Spain, in 1990, 1994, and 1999, respectively.

Since 2001, he has been an Associate Professor with the Department of Electronic Engineering, Technical University of Catalonia, where he teaches power electronics and control theory. He is the coauthor of 10 papers in international journals and more than 50 communications in international conferences. His research fields are related to nonlinear control and its application to renewable energy systems and power electronics.

Francesc Guinjoan (M'92) received the Ingeniero de Telecomunicación and Doctor Ingeniero de Telecomunicación degrees from the Universitat Politecnica de Catalunya (UPC), Barcelona, Spain, in 1984 and 1990, respectively, and the Docteur es Sciences degree from the Université Paul Sabatier, Toulouse, France, in 1992.

He is currently an Associate Professor with the Departamento de Ingenieria Electrónica, Escuela Técnica Superior de Ingenieros de Telecomunicación Barcelona, UPC, where he teaches courses on power electronics. He has coauthored more than 80 papers in international journals and conferences. His research interests include power electronics modeling and control for renewable energy systems

Dr. Guinjoan was a guest Coeditor of the Special Issue on "Smart Devices for Renewable Energy Systems" of the IEEE TRANSACTIONS ON INDUSTRIAL ELECTRONICS in 2011.

Carlos Meza (S'00–M'07) received the B.S. degree in electronic engineering from the Costa Rica Institute of Technology, Cartago, Costa Rica, in 2001, the M.Eng. degree in embedded systems design from the ALaRI Institute, University of Lugano, Lugano, Switzerland, in 2003, and the Ph.D. degree in advanced automation and robotics from the Technical University of Catalonia, Barcelona, Spain, in 2007.

He has been a Visiting Researcher with the University of Groningen, Groningen, The Netherlands. From 2007 to 2009, he was with the Institute of Applied Sustainability for the Built Environment, SUPSI, Cannobio, Switzerland. Currently, he is a Professor and Researcher with the Department of Electronic Engineering, Costa Rica Institute of Technology, where he is the Coordinator of the Laboratory of Electronic Systems for the Sustainability (SESLab). His main research interests include nonlinear dynamics, nonlinear control, and renewable energy systems.

Juan J. Negroni (M'04) received the degree in electronics engineering from the Universidad Tecnológica Metropolitana del Estado de Chile, Santiago, Chile, and the Ph.D. degree in electronics engineering from the Universitat Politecnica de Catalunya, Barcelona, Spain, in 2007.

Since 1999, he has been an Associate Professor with the Department of Electronic Engineering, Universidad Tecnológica Metropolitana del Estado de Chile, where he teaches courses on power electronics. He is the Project Leader of "Chilectra-UTEM" dealing with photovoltaic grid-connected systems, and he also participates in research and innovation for the EU-LA group and for the R&D group "Proteinlab-UTEM." His research interests include power electronics for renewable energy systems.

Lyapunov-Based Control Scheme for Single-Phase Grid-Connected PV Central Inverters

C. Meza, *Member, IEEE*, D. Biel, *Member, IEEE*, D. Jeltsema, *Member, IEEE*, and J. M. A. Scherpen, *Senior Member, IEEE*

***Abstract*—A Lyapunov-based control scheme for single-phase single-stage grid-connected photovoltaic central inverters is presented. Besides rendering the closed-loop system globally stable, the designed controller is able to deal with the system uncertainty that depends on the solar irradiance. A laboratory prototype has been built as a proof of concept for the proposed control technique. A nonlinear passive adaptive controller has been programmed in a field-programmable gate array.**

I. Introduction

THE inconveniences related to conventional energy generation have motivated the introduction of new regulations created to stimulate the usage of photovoltaic (PV) systems. The success of these policies relies on the cost-per-watt reduction of PV systems in order to make PV energy more competitive with respect to traditional energy sources. In general, current research to reduce the cost-per-watt of PV systems includes the following:

1) improving the efficiency of PV cells/modules;
2) reducing the manufacturing costs of PV cells/modules;
3) increasing the overall PV system efficiency by focusing on the power conditioning elements.

During the last years a lot of effort has been devoted to the first two aforementioned activities, yielding high-efficient and cheaper PV panels based on new PV cell material and manufacturing technologies. An alternative way to reduce the cost-per-watt of existing PV systems is by increasing the efficiency of the overall system using a suitable designed power conditioning stage. The power conditioning stage is an essential part of the PV system since it must account for an optimal energy transfer from the energy source to the load. Improving the quality of the power conditioning stage is one of the key issues of future PV applications [1].

Manuscript received September 01, 2010; accepted December 01, 2010. Manuscript received in final form February 07, 2011. Date of publication March 07, 2011; date of current version February 01, 2012. Recommended by Associate Editor A. Loria. This work was supported in part by the Spanish Ministry of Sciences and Innovation under Grant DPI2007-62582, Grant DPI2009-14713-CO3-03, and Grant DPI2010-15110.

C. Meza is with the Instituto Tecnologico de Costa Rica, Cartago 30101, Costa Rica (e-mail: cmeza@itcr.ac.cr).

D. Biel is with the Institute of Industrial and Control Engineering, University of Catalonia, Barcelona 08034, Spain (e-mail: biel@eel.upc.edu).

D. Jeltsema is with Delft Institute of Applied Mathematics, Delft University of Technology, 2628 CD Delft, The Netherlands (e-mail: d.jeltsema@tudelft.nl).

J. M. A. Scherpen is with Discrete Technology and Production Automation, University of Groningen, 9747 AG Groningen, The Netherlands (e-mail: j.m.a.scherpen@rug.nl).

Digital Object Identifier 10.1109/TCST.2011.2114348

The design of a PV power conditioning system generally consists of a two step procedure, namely: 1) a proper selection of the circuit topology and the elements of the power converter and 2) the design of an adequate control strategy for the chosen power conditioning stage. The latter task is important when aiming at a stable non-oscillatory dynamical behavior of the PV system.

Regarding the design of control strategies for power converters it is evident that there is a long tradition of using linear design techniques. Linear controllers are found suitable in those cases where the power converter operates about a fixed operating point and the disturbances are small. The control of power inverters and rectifiers in order to obtain a sinusoidal current in phase with the grid voltage have mainly been done by means of the so-called "P+Resonant" controllers. For a linear system, e.g., a battery inverter, it is possible to show by means of the internal mode principle that there exists a linear transfer function capable of eliminating the steady-state error [2], [3].

For PV power inverters, the control requirements have been generally carried out by means of a strategy based on two cascaded control loops using a pulse-width modulation (PWM) scheme [4], [5], where the inner control loop is in charge to establish the duty ratio for the generation of a sinusoidal output current that is in phase with the grid voltage. In turn, the outer control loop has to settle the PV array operating point at its maximum power value for any temperature and irradiance variation, with the help of a maximum power point algorithm such as Perturb and Observer [6] or more advanced ones [7], [8]. The outer loop delivers to the inner control the current reference amplitude corresponding to the PV array maximum power point, thereby ensuring the power transfer to the grid [2], [3]. P+Resonant controller have mainly been used as inner controller specially in the output inverter stage of multi-stage grid-connected PV systems. In this case, the adequate dimensioning of the dc link capacitor allows to approximate the output inverter stage as a linear system independent of the PV array nonlinear characteristics, and therefore allowing to apply the "P+Resonant" controller design procedure [3], [9].

Nevertheless, for single-phase grid-connected PV inverters the use of linear techniques, such as Laplace transformations or frequency-based analysis, require of a previous linearization step, which constitutes an approximation of the complete dynamical behavior of the overall system since: 1) the PV source exhibits a strongly nonlinear electrical behavior that affects all the variables of the system and 2) the electrical characteristics of the PV source are time-varying and therefore the system is not linearizable around a unique operating point or trajectory. These difficulties have motivated us to proceed with a different approach than the usual "classical" control techniques. Moreover, for similar reasons as discussed above, there is a growing

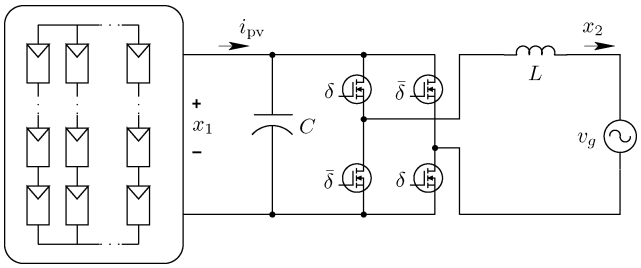

Fig. 1. Full-bridge GPV inverter schematic.

interest in the context of nonlinear control of power converters from researchers of both the power electronics and the control community, see, e.g., [10]–[12] and [13]. Of special interest is the Lyapunov-based nonlinear controller technique for power converters proposed in [14] that renders the closed-loop system globally asymptotically stable. This technique has been proved useful for dc-dc converters (e.g., [15]) and ac-dc converters (e.g., [16]). In the context of PV power systems, [17] presents a globally stable closed-loop system for a single-stage full-bridge grid-connected power inverter using a similar controller design technique than that of [14]. Some disadvantages of nonlinear controllers for power converters that may be encountered during the practical implementation are the computational complexity and its dependency on the system's parameters. Nevertheless, the high processing power normally required by nonlinear controllers is not a serious problem given the recent development of new processors with increase performance at reasonable prices. On the other hand, there are cases (e.g., [18] and [19]) in which the parameter dependency of the nonlinear controllers has been circumvented adding an adaptive functionality to the control scheme.

This paper introduces a nonlinear and adaptive control scheme for a single-phase single-stage grid-connected PV inverter. It is shown by means of an analytical and experimental study that the proposed controller provides a satisfactory closed-loop behavior without neglecting the nonlinear electrical characteristics of the system. The main contribution of this paper consists in extending the robustness of the controller proposed in [17] by estimating the value of the parameter that changes with the unknown solar irradiance. Additionally, the practical validity of the proposed control scheme is evaluated using an experimental laboratory prototype.

II. Grid-Connected PV (GPV) System: Modeling and Assumptions

The GPV system that is considered in the present paper is shown in Fig. 1. The system consists of an array of PV panels connected to the utility grid by means of a full-bridge inverter. GPV systems, unlike standalone ones, are designed to transfer the PV panels' energy to the utility grid, thus being the main requirement of the system to deliver a sinusoidal current in phase with the utility grid voltage. Standalone PV systems transfer the PV panels' energy to a load; in this case it is necessary to output a sinusoidal voltage.

This paper deals only with GPV systems, and more specifically with the GPV configuration in which all the PV panels are linked to a unique power inverter unit, known as "central inverter". A GPV central inverter is one of the most prevailing configurations since, under uniform irradiance conditions of the PV panels, it represents a good tradeoff between the extracted energy and the design complexity of the power inverter [20]–[22]. Moreover, the full-bridge power inverter stage is a typical output stage present in other GPV configurations such as the widely used two-stage boost-buck configuration (e.g., [23], [24]) or the multilevel configuration (e.g., [25]). As stated in [26], this common output stage enables to extrapolate the central inverter's control scheme to other configurations.

A. PV Generator

The typical electrical behavior of a crystalline silicon (c-Si) PV cell can be modeled in the following way:

$$i_{\rm pv_{cell}} = I_{g_{\rm cell}}(G) - I_{\rm sat_{cell}}(T)\left[\exp\left(\frac{v_{\rm pv_{cell}}(T)}{\eta v_{T_{\rm cell}}(T)}\right) - 1\right] \quad (1)$$

where $i_{\rm pv_{cell}}$ and $v_{\rm pv_{cell}}$ are the cell current and voltage, respectively, and as follows:

- $I_{g_{\rm cell}}(G)$ is the generated current due to the incident solar irradiance G;
- η is the PV cell emission coefficient;
- $I_{\rm sat_{cell}}(T)$ is the reverse saturation current of the PV cell p-n junction that varies with the temperature T;
- $v_{T_{\rm cell}}(T)$ is the p-n junction thermal voltage which also changes with the temperature.

Given that PV cells are usually located in an uncontrolled atmospheric environment, they are exposed to temperature (T) and solar irradiance (G) variations and rigorously $I_{g_{\rm cell}}(t)$, $I_{\rm sat_{cell}}(t)$, and $v_{T_{\rm cell}}(t)$ should be considered as time-varying signals. Nevertheless, these variations are slow compared to the dynamics of practical power inverters which are designed with transient response times much smaller than an utility grid period, T_g, (20 ms for the European utility grid). Thus, it can be assumed that both the temperature and solar irradiance do not change significantly in one T_g. Note also that, for the case of c-Si solar cells, it is possible to derive mathematical expressions to accurately obtain its parameters at any moment providing temperature and solar irradiance measurements [27]–[29]. Nonetheless, differently from temperature sensors, solar irradiance sensors are costly and difficult to calibrate properly. Accordingly, in the present paper we assume that the parameters that depend on temperature are known.

For analytical convenience, we assume that the electrical behavior of a PV array is defined as follows:

$$i_{\rm pv} = \Lambda - \rho(v_{\rm pv}) \quad (2)$$

where $v_{\rm pv}$ and $i_{\rm pv}$ are the PV array voltage and current, respectively, and Λ represents the part of the photovoltaic generator current that depends on the solar irradiance. The last term of (2) denotes the direct link between the voltage of the photovoltaic generator and the associated current, i.e.,

$$\rho(v_{\rm pv}) = \Psi \exp\left(\alpha\, v_{\rm pv}\right) \quad (3)$$

where Ψ and α represent positive parameters of the photovoltaic generator. Referring to the equation of the PV cell (1), the pa-

rameters of this model can be defined as $\Lambda = (I_{g_{\rm cell}} + I_{{\rm sat}_{\rm cell}})n_p$, $\Psi = I_{{\rm sat}_{\rm cell}}\, n_p$, and $\alpha = (n_s)/(\eta v_{T_{\rm cell}})$, where n_s and n_p are the number of PV cells connected in series and parallel, respectively.

B. Power Conditioning System

The schematic diagram of the full-bridge central inverter configuration is shown in Fig. 1. Here x_1 and x_2 are the average values of the input capacitor voltage and the output inductor current, respectively. The utility grid voltage v_g is assumed to be sinusoidal with a constant amplitude A and a constant frequency ω, i.e., $v_g = A\sin(\omega t)$. The full-bridge inverter consists of four switches controlled by the signals δ and $\bar{\delta}$ which take values in the discrete set $\{0, 1\}$ (i.e., OFF or ON, respectively). The switch control signals are generated via a PWM scheme with a duty ratio function $u \in [-1, 1]$ generated by the controller. This means that if the switching frequency is sufficiently high, the dynamical behavior of the GPV system can be approximated by the following set of differential equations:

$$C\dot{x}_1 = -u\, x_2 + \Lambda - \rho(x_1) \tag{4}$$

$$L\dot{x}_2 = u\, x_1 - v_g. \tag{5}$$

The latter equations will be used to design a controller for the system, where we assume that the only unknown parameter is Λ. The controller should be able to deal with this parameter uncertainty.

III. Controller Design

A. Control Objectives

The GPV inverter of Fig. 1 should be able to transfer efficiently the maximum amount of PV energy to the utility grid. In order to accomplish that the following is required.

- C1) to deliver a sinusoidal current in phase with the utility voltage of the power grid;
- C2) to regulate the input capacitor voltage to a value that assures maximum power extraction from the PV array.

With respect to C2, it should be mentioned that it is assumed that the reference capacitor voltage value is given by an external maximum power point tracking (MPPT) algorithm. MPPT algorithms operate based on the changes of temperature and solar irradiance and therefore change very slowly compared to the dynamics of the power inverter. For instance, slow varying MPPTs (variation time >20 ms), such as an extremum-seeking [30] or others based on heuristic approaches [31] may be added to this scheme without affecting the dynamic behavior of the analyzed closed-loop system.

Based on (4) and the notation presented in Section II, objectives C1 and C2 translate into $\{x_1, x_2\} = \{x_{1r}, x_{2r}\}$, where

$$x_{2r} = A_{\rm Ir}\sin\omega t \tag{6}$$

and x_{1r} is the value of x_1 such that $P_{\rm pv}(x_1)$ is maximum. The power generated by the PV panels equals $P_{\rm pv}(x_1) = x_1 i_{\rm pv}$.

Ideally, x_{1r} should be a constant in order to assure that the PV array operating point remains always in its maximum power point. However, due to the intrinsic nature of the inverter structure used it is not possible to have a sinusoidal output current and a constant input voltage. This impossibility can be seen assuming that $[x_1, x_2] = [x_{1r}, x_{2r}]$ and obtaining the energy-balance equation of the system from (4)

$$x_{1r}C\dot{x}_{1r} + x_{2r}L\dot{x}_{2r} = \Lambda x_{1r} - x_{1r}\rho(x_{1r}) - v_g x_{2r}. \tag{7}$$

Notice that this expression is independent from the control signal u. Substituting (6) into (7) yields

$$C\dot{x}_{1r} = \frac{P_{\rm pv}(x_{1r})}{x_{1r}} + \frac{AA_{Ir}}{2x_{1r}}\left(\cos(2\omega t) - \frac{A_{Ir}}{A}L\omega\sin(2\omega t) - 1\right) \tag{8}$$

where we recall that $P_{\rm pv}(x_{1r}) = x_{1r}\Lambda - x_{1r}\Psi\exp(\alpha x_{1r})$.

From (8) it is clear that x_{1r} has to be time-varying. Nevertheless, a time-varying x_{1r} is an undesired effect because it will move the PV array operating point from its maximum power point. A practical solution for this problem, widely used in the design of Central PV inverters, is to make C sufficiently large to reduce the oscillations towards the PV array maximum power point. Indeed, as is shown next, $x_{1r}(t)$ obtained from (8) is a periodic signal with an offset value $\bar{x}_{1r}$, such that $x_{1r} \approx \bar{x}_{1r}$ when C is sufficiently large[1].

For analysis convenience instead of x_{1r} consider the energy stored in the capacitor, i.e., $\mathcal{E}^* = (1)/(2)Cx_{1r}^2$ and substitute it in (8) obtaining

$$\dot{\mathcal{E}}^* = P_{\rm pv}(\mathcal{E}^*) + \frac{AA_{1r}}{2}\left(\cos(2\omega t) - \frac{A_{\rm Ir}}{A}L\omega\sin(2\omega t) - 1\right). \tag{9}$$

Instead of obtaining the exact analytical solution of (9) we will solve its linearized version. Given that we will have a sufficiently large C the linearization of (9) is a very good approximation as it will be shown.[2] Linearizing the nonlinear function $P_{\rm pv}(\mathcal{E}^*)$ around the dc value of $\mathcal{E}^*$ (denoted as $\overline{\mathcal{E}^*}$) yields

$$\mathcal{P}(\mathcal{E}^*) \approx P_{\rm pv}(\overline{\mathcal{E}^*}) + m\left(\mathcal{E}^* - \overline{\mathcal{E}^*}\right) \tag{10}$$

where

$$\begin{aligned} m &= \left.\frac{dP_{\rm pv}(\mathcal{E}^*)}{d\mathcal{E}^*}\right|_{\mathcal{E}}^{*} = \overline{\mathcal{E}^*} \\ &= \frac{\left(\Lambda - \Psi\exp\left(\alpha\sqrt{\frac{2\overline{\mathcal{E}^*}}{C}}\right)\left(1 + \alpha\sqrt{\frac{2\overline{\mathcal{E}^*}}{C}}\right)\right)}{C\sqrt{\frac{2\overline{\mathcal{E}^*}}{C}}}. \end{aligned} \tag{11}$$

Hence, (9) reduces to

$$\begin{aligned} \dot{\mathcal{E}} = {} & P_{\rm pv}(\overline{\mathcal{E}^*}) + m\left(\mathcal{E}^* - \overline{\mathcal{E}^*}\right) - \frac{1}{2}(A_{\rm Ir})^2 L\omega\sin(2\omega t) \\ & - \frac{1}{2}AA_{\rm Ir} + \frac{1}{2}AA_{\rm Ir}\cos(2\omega t). \end{aligned} \tag{12}$$

[1]Notice that having a C sufficiently large is a requirement for this type of power inverters, given that smaller values of C may reduce considerable the amount of energy extracted from the PV array.

[2]Take into account that this linearization process is only done in order to estimate the waveform of the desired steady-state value x_{1r} and to verify that it is periodic. In the remainder of the article we will be working with the nonlinear dynamics of the system.

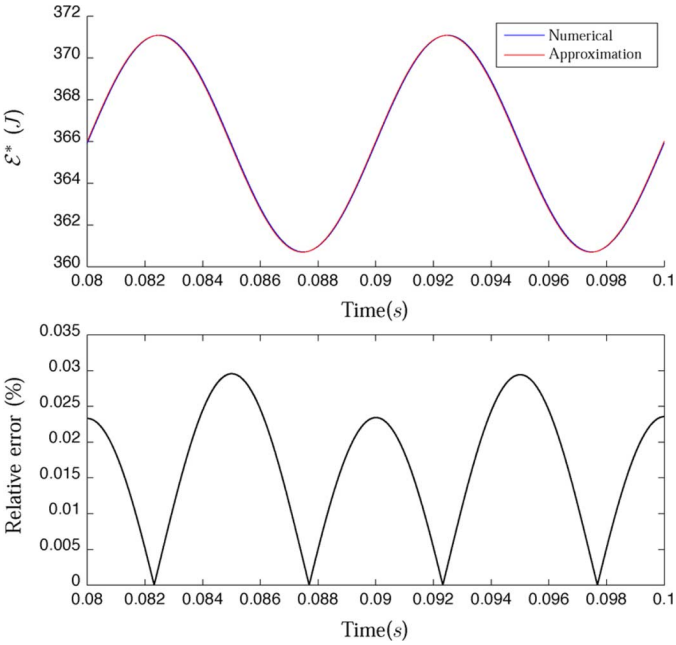

Fig. 2. Comparison between the approximated $\mathcal{E}^*$ and the signal obtain solving numerically the differential equation for $\mathcal{E}^*$ with no approximation.

From the previous equation it is evident that $\mathcal{E}^*$ presents sinusoidal components. Moreover, if

$$\mathcal{E}^* = \overline{\mathcal{E}^*} + a_1 \cos(2\omega t) + b_1 \sin(2\omega t) \tag{13}$$

is a solution of (12) the following equality holds:

$$-2a_1\omega \sin(2\omega t) + 2b_1\omega \cos(2\omega t) = P_{\rm pv}(\overline{\mathcal{E}^*}) - 0.5AA_{\rm Ir} - (0.5AA_{\rm Ir} + ma_1)\cos(2\omega t)$$

from which the expressions for $A_{\rm Ir}$, a_1, and b_1 are obtained as

$$A_{\rm Ir} = \frac{2P_{\rm pv}(\overline{\mathcal{E}^*})}{A} = \frac{2P_{\rm pv}(\overline{x_{1r}})}{A} \tag{14}$$

$$a_1 = \frac{0.5AA_{\rm Ir}(2k\omega L - m)}{4\omega^2 + m^2} \tag{15}$$

$$b_1 = \frac{0.5AA_{\rm Ir}\omega(2 + mkL)}{4\omega^2 + m^2}. \tag{16}$$

Notice that if $\mathcal{E}^*$ is described as (13) the reference value of the output current amplitude, $A_{\rm Ir}$, depends only on the dc value of the reference voltage $\bar{x}_{1r}$. Consequently, $A_{\rm Ir}$ will vary every time $\bar{x}_{\rm Ir}$ varies, that is, when the external MPPT algorithm provides a new value of $\bar{x}_{1r}$.

In order to validate the approximation of expression of $\mathcal{E}^*$ two simulations are performed. The first simulation solves numerically the equation of $\mathcal{E}^*$ with no approximation [i.e., (8)]. In the second simulation signal $\mathcal{E}^*$ is obtained using the parameters of (14)–(16). The two calculated values of $\mathcal{E}$ are generated with the same value of $A_{\rm Ir}$ corresponding to the PV array maximum power point voltage. The parameters of the full-bridge inverter are the following: $L = 1$ mH, $C = 2.2$ mF. The results are shown in Fig. 2. It is seen that the two signal are very alike with a maximum relative error of 0.03%.

B. Proposed Controller

In order to obtain an implementable nonlinear control law, the controller design methodology is divided in two parts, namely, as follows.

P1) An *analytical* control design stage in which a globally-stable closed-loop system is obtained based on the nonlinear model of the system.

P2) A *practical* control design stage in which practical aspects of the system are considered, e.g., the controller derived is adapted to be implemented experimentally, and a robustness analysis is performed to assure the adequate closed-loop behavior under parameter uncertainties.

The proposed control scheme is based on the work of [14]. This controller design technique is successfully applied to power converters with constant energy sources under the assumption that all the system parameters are known (see, e.g., [15] for dc-dc power converter applications and [16] for ac-dc power converter applications). The novelty of the control scheme presented in this paper lies in the extension of the control strategy of [14] in order to deal with the PV inverter's nonlinear energy source characteristics and the uncertainty of the time-varying parameter Λ. Additionally, the robustness of the proposed control scheme to various parameter uncertainties in the system is considered.

Following [14], we will start the control scheme design by defining an adequate reference system for the GPV inverter under consideration, i.e.,

$$\begin{aligned} C\dot{x}_{1r} &= -u_r\, x_{2r} + \hat{\Lambda} - \rho(x_{1r}) \\ L\dot{x}_{2r} &= u_r\, x_{1r} - v_g \end{aligned} \tag{17}$$

where ideally x_{1r} and x_{2r} are the desired capacitor voltage and the output current, respectively, and $\hat{\Lambda}$ is the estimated value of Λ. For the moment, assume that x_{1r} and x_{2r} are taken from (4) and (6), in Section IV these expressions are discussed with more detail. Accordingly, signal u_r is

$$u_r = \frac{L\dot{x}_{2r} + v_g}{x_{1r}}. \tag{18}$$

Let e_1, e_2, e_u, and e_Λ represent the errors between the actual measured variables and their reference counterparts, i.e., $e_1 = x_1 - x_{1r}$, $e_2 = x_2 - x_{2r}$, $e_u = u - u_r$, and $e_\Lambda = \Lambda - \hat{\Lambda}$, respectively, then the system dynamics can be written as

$$\begin{aligned} C(\dot{e}_1 + \dot{x}_{1r}) &= -(e_u + u_r)(e_2 + x_{2r}), \\ &\quad + e_\Lambda + \hat{\Lambda} - \rho(x_{1r}) - e_\rho(e_1, x_{1r}) \\ L(\dot{e}_2 + \dot{x}_{2r}) &= (e_u + u_r)(e_1 + x_{1r}) - v_g \end{aligned} \tag{19}$$

where $\rho(x_1)$ is decomposed into $\rho(x_1) = \rho(x_{1r}) + e_\rho(e_1, x_{1r})$, with $e_\rho(e_1, x_{1r}) = \Psi[\exp(\alpha e_1 + \alpha x_{1r}) - \exp(\alpha x_{1r})]$.

According to [14], it is possible to synthesize a control signal that yields the desired closed loop behavior from the system error dynamics. In this regard, the control signal u is composed of two elements, namely, a control u_r defined according to (18) and a control e_u designed such that the system error dynamics

vanishes. The error dynamics are obtained by substituting (17) in (19), i.e.,

$$\begin{aligned} C\dot{e}_1 &= -u_r\, e_2 - e_u\,(x_{2r} + e_2) \\ &\quad + e_\Lambda - e_\rho(e_1, x_{1r}) \\ L\dot{e}_2 &= u_r\, e_1 + e_u\,(x_{1r} + e_1). \end{aligned} \tag{20}$$

Notice that in our case we do not only have to synthesize the control e_u that renders the error dynamics (20) stable, but we should derive an additional mechanism to estimate parameter Λ, i.e., to make $\hat{\Lambda} = \Lambda$. In order to proof the validity of our control scheme the final stability analysis should take into account the designed signal e_u and the dynamics associated to the estimation of Λ.

In order to estimate $\hat{\Lambda}$, the following adaptive law, taken from [19], is used:

$$\dot{\hat{\Lambda}} = \mathsf{Prj}\{\gamma\, e_1\} = \begin{cases} \gamma e_1, & \text{if } \hat{\Lambda} > \epsilon \\ 0, & \text{otherwise} \end{cases} \tag{21}$$

where $\gamma \in \mathbb{R}^+$ is the adaptive gain and $\mathsf{Prj}\{\cdot\}$ is a projection operator that ensures $\hat{\Lambda} \geq \epsilon > 0$, with ϵ an arbitrary small constant.

The stability of the error dynamics (20) can be proved by means of the following Lyapunov function

$$H = \frac{1}{2}Ce_1^2 + \frac{1}{2}Le_2^2 + \frac{1}{2\gamma}e_\Lambda^2 \tag{22}$$

for which the time derivative along the system trajectories of (20) yields

$$\dot{H} = e_u\,(x_{1r}e_2 - x_{2r}e_1) - e_1 e_\rho(e_1, x_{1r}) + e_\Lambda e_1 + \frac{1}{\gamma}e_\Lambda \dot{e}_\Lambda. \tag{23}$$

The closed-loop system will be globally asymptotically stable if the aforementioned expression is negative definite, i.e., if $\dot{H} < 0$ for all values of e_1, e_2, e_Λ different from zero. Defining e_u as

$$e_u = -K(x_{1r}\, e_2 - x_{2r}\, e_1) \tag{24}$$

where $K > 0$ is a control parameter, the first term of (23) remains always non-positive, i.e.,

$$\dot{H} = -K(x_{1r}e_2 - x_{2r}e_1)^2 - e_1 e_\rho(e_1, x_{1r}) + e_\Lambda e_1 + \frac{1}{\gamma}e_\Lambda \dot{e}_\Lambda. \tag{25}$$

On the other hand, considering Λ "locally constant", yields $\dot{e}_\Lambda = -\dot{\hat{\Lambda}}$, and according to (21), $\dot{e}_\Lambda = -\gamma\, e_1$, and thus, the derivative of the Lyapunov function (25) can be written as

$$\dot{H} = -K(x_{1r}e_2 - x_{2r}e_1)^2 - e_1 e_\rho(e_1, x_{1r}). \tag{26}$$

Notice that the product $e_1 e_\rho(e_1, x_{1r})$ is always positive given that function $\rho(\cdot)$ is strictly increasing, i.e., the function $e_\rho(e_1, x_{1r})$ is positive when $e_1 = x_1 - x_{1r} > 0$ and negative when $e_1 < 0$. Thus, the closed-loop system (19), using the control signal (18), (24) and the adaptive control law (21), is globally asymptotically stable.

IV. Practical Considerations

In this section, some practical considerations regarding the previously derived control law are discussed.

A. Reference Computation

The control scheme derived in the previous section comprises expressions (7), (18), (21), and (24). From these expressions the most difficult to implement is (7), not only because it is a nonlinear differential equation that requires to be solved numerically. Recall that (7) is needed in order to obtain the reference current amplitude, A_{IR}, from the dc value of x_{1r} provided by and external MPPT algorithm. Nevertheless, as it was mentioned in Section III, for large values of C, (7) can be approximated as (13) yielding a simple expression to derive A_{Ir}, i.e., (14). In this way, we end up with a $x_{2r}(t)$ which depends only on the dc value of x_{1r} provided by the external MPPT algorithm, i.e., $x_{2r} = A_{\mathrm{Ir}} \sin(\omega t)$, where

$$A_{\mathrm{Ir}} = \frac{2P_{\mathrm{pv}}\bar{x}_{1r}}{A} = \frac{2\bar{x}_{1r}(\hat{\Lambda} - \rho(\bar{x}_{1r}))}{A}. \tag{27}$$

B. Unconsidered Parameter Variation

The robustness of the controller proposed in Section II has been only proved for slow variations of parameter Λ. In this regard, the effect of the variation of the parameters considered known in the derived control law is analyzed next.

Initially, consider the case in which the inductance L is unknown and assume that $\hat{L} \neq L$ is the inductance used by the controller. With the reference system

$$\begin{aligned} C\dot{x}_{1r} &= -u_r\, x_{2r} + \hat{\Lambda} - \rho(x_{1r}) \\ \hat{L}\dot{x}_{2r} &= u_r\, x_{1r} - v_g \end{aligned} \tag{28}$$

the error dynamics (20) are modified as

$$\begin{aligned} C\dot{e}_1 &= -u_r\, e_2 - e_u\,(x_{2r} + e_2) + e_\Lambda - e_\rho(e_1, x_{1r}) \\ L\dot{e}_2 - e_L\dot{x}_{2r} &= u_r\, e_1 + e_u\,(x_{1r} + e_1) \end{aligned} \tag{29}$$

where $e_L = L - \hat{L}$. Using the controllers defined by (18), (21), and (24), and using the Lyapunov function (22), yields the Lyapunov derivative

$$\dot{H} = -K(x_{1r}e_2 - x_{2r}e_1)^2 - e_1 e_\rho(\cdot) - e_2 e_L \dot{x}_{2r} \tag{30}$$

which is the same as expression (26) but with an additional term depending on L, $\hat{L}$, x_2, and x_{2r}. Thus, in order to assure that the controller will not be affected by variations of L the controller parameter K should be sufficiently large in order to dominate the last term of (26). Besides, notice that in steady-state e_2 is T_g-periodic and thus the last adding term of (26) is bounded and the system remains BIBO (i.e., bounded-input bounded-output) stable.

Notice also that the contribution of the controller expression that contains the inductance in (18) can be neglected when $L\omega A_{\mathrm{Ir}}|_{\max(P_{\mathrm{pv}})} \ll A$, where $A_{\mathrm{Ir}}|_{\max(P_{\mathrm{pv}})}$ is the output current reference amplitude when the power generated by the PV array (P_{pv}) is maximum. Take into account that the maximum

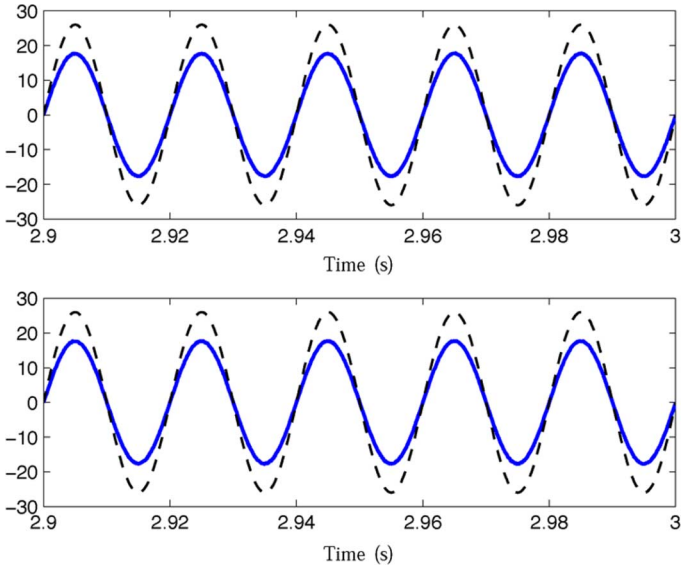

Fig. 3. Numerical simulation results of the output current for a 3.25 kW$_p$ GPV system using the proposed controller with (top figure) and without (bottom figure) the term containing L. The scaled grid voltage, $v_g/12$, is shown with dashed lines and its scale is in volts, the other curve corresponds to x_2 in (a).

value of $A_{\rm Ir}$ will occur when the PV panels produce its maximum power. Using (27), the aforementioned condition can be rewritten as $\max(P_{\rm pv}) \ll (A^2)/(2L\omega)$, which is valid in those cases where single-phase PV inverters are normally used, e.g., residential grid connected PV systems. For example, in the case of a 3 kW$_p$ residential PV system connected to an European grid (i.e., $A = 312$ V) the expression with the inductance in (18) can be neglected if $L \ll 51$ mH. Fig. 3 shows the numerical simulation results of the output current of a 3.25 kW$_p$ GPV system using the single-phase inverter of Fig. 1 ($L = 2$ mH, $C = 2.2$ mF, $v_g = 312\ \sin(100\,\pi t)$) and the proposed control scheme. Two cases have been simulated: one in which the complete expression of the controller is used and another one in which the term containing the inductance is neglected. Notice how the difference between both currents is unnoticeable.

Even though we do not consider any uncertainties in other system parameters, such as α and Ψ, in the theoretical analysis and derivation of the controller, the appearance of the integral term included for the estimation of Λ, i.e., the adaptive law (21), allows to achieve the control objectives C1 and C2 although α and ϕ values change in a certain percentage of variation.

A series of numerical simulations have been performed in order to verify the robustness of our proposed controller in front of non-considered uncertainties, i.e., variations of α and Ψ. For the simulation we considered the system of Fig. 1 with $C = 2.2$ mF, $L = 2$ mH, $v_g = 312\ \sin(\,100\pi t)$ V and a PV array with a peak power of 3.3 kW, a short circuit current of 6.1 A, and a open circuit voltage of 678 V at 1000 W/m^2 ($\Lambda = 6.1, \alpha = 0.026, \Psi = 1.35 \times 10^{-7}$). The simulation tests consisted of two step-wise variations of α and Ψ of $+5\%$ and -5% at $t = 4$ s, where the average voltage reference value was set to 587.8 V. The simulation results are shown in Figs. 4 and 5, notice how in both cases the system is able to keep the commanded voltage value while maintaining at all time a sinusoidal current in phase with the grid voltage.

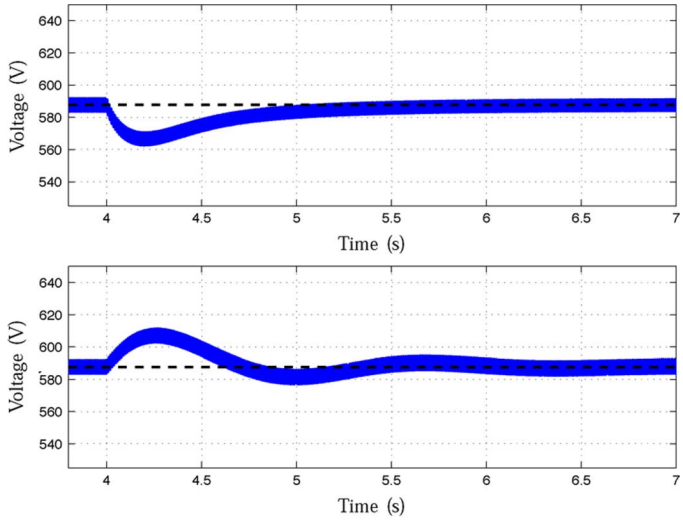

Fig. 4. Capacitor voltage: numerical simulation results of a $+5\%$ (top figure) and -5% (bottom figure) variation of α and Ψ. The variation of α and Ψ is done at $t = 4$ s. The dashed line represents the reference value.

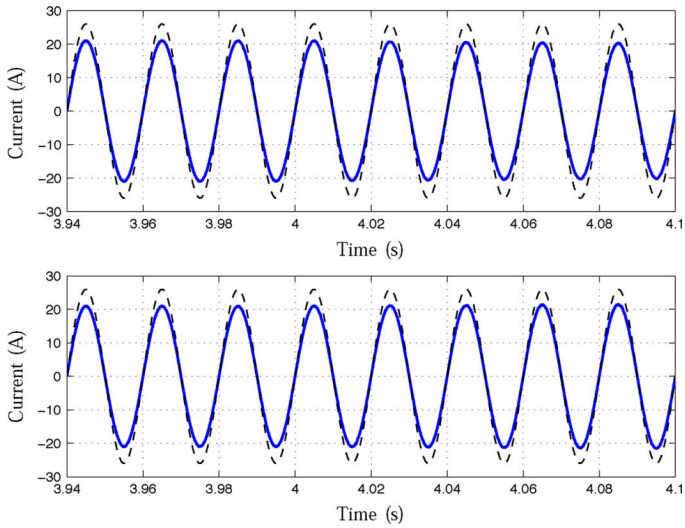

Fig. 5. Output current: numerical simulation results of a $+5\%$ (top figure) and -5% (bottom figure) variation of α and Ψ. The variation of α and Ψ is done at $t = 4$ s. The dashed line represents the scaled grid voltage $(v_g/12)$.

V. Experimental Tests

In order to test the designed control scheme under realistic conditions and further study its robustness in front of unmodeled dynamics a laboratory prototype was built. The schematic circuitry of the experimental prototype is shown in Fig. 6, where the signals x_1, x_2, and v_g enclosed in squares represent the measured capacitor voltage, inductor current and utility grid voltage, respectively. The values of the circuit's parameters have been chosen according to the criteria described in Section III, that is, to guarantee a low ripple voltage in the PV array's terminals ($C = 2.2$ mF) and to minimize the effects of the unconsidered parameters variation ($L = 500\ \mu$H). As an input energy source we used an Agilent E4350B solar array simulator (SAS). This device enables to program different $i - v$ curves, which for experimental validation turns out to be very useful since it allows

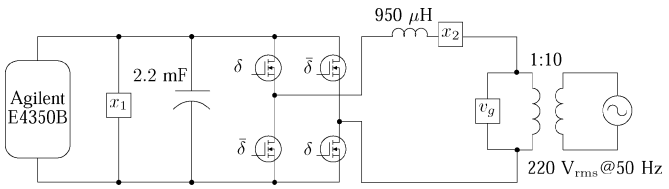

Fig. 6. Experimental prototype schematic circuitry.

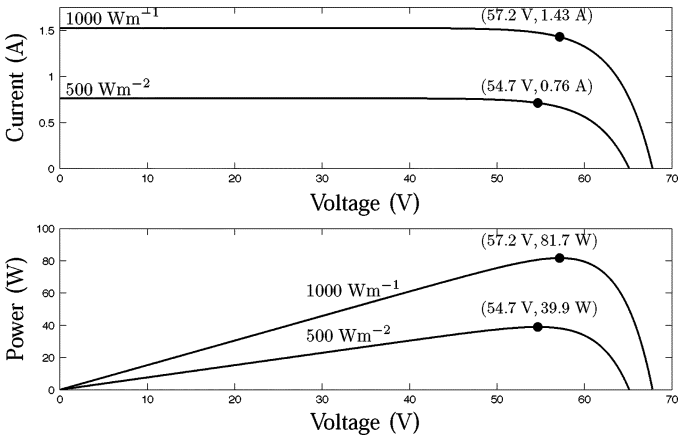

Fig. 7. PV array electrical curves used the experimental tests.

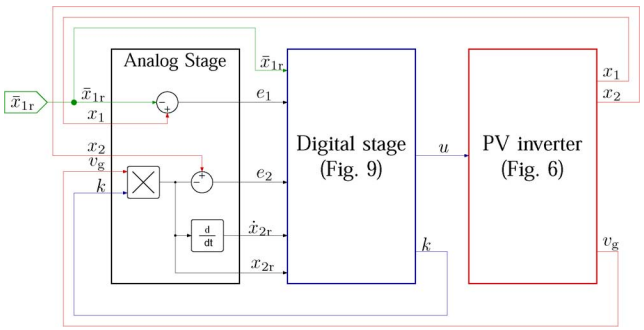

Fig. 8. Experimental prototype block diagram. Here k is a signal proportional to A_{Ir}, i.e., $k = (A_{\mathrm{I_r}})/(A)$, see Fig. 9.

to generate fast changes in the PV array electrical characteristics. The $i - v$ curves programmed in the SAS for the experimental tests performed are shown in Fig. 7. Due to the solar array simulator low output voltage level (it has a maximum voltage of 80 V) a transformer was required to connect the GPV inverter prototype to the grid. As it can be seen in Fig. 6 all the measurements where done in the low-voltage side of the transformer which exhibits a voltage amplitude of 31.4 V at 50 Hz, and thus the transformer dynamics was not considered in the model. Thus, for this experiment we considered the low-voltage side of the transformer as the grid-voltage and measured the power factor in this side. In a larger version of this prototype (with higher PV array's voltage) the transformer can be removed. A primary objective pursued when implementing the controller was to obtain a simple, economical circuit. That is why we decided to divide the controller implementation in an analog and digital stage. The analog stage has been designed to

[3]Even though we use a medium size, medium cost FPGA, the implemented algorithm can be easily migrated to a cheaper PLD, e.g., CPLD or similar.

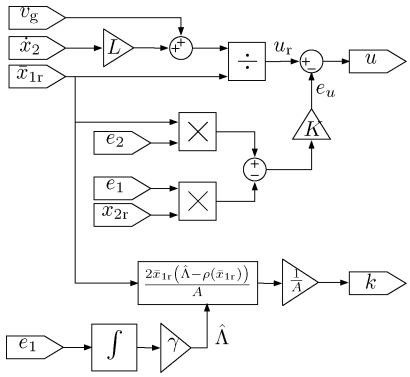

Fig. 9. Functions implemented in the FPGA.

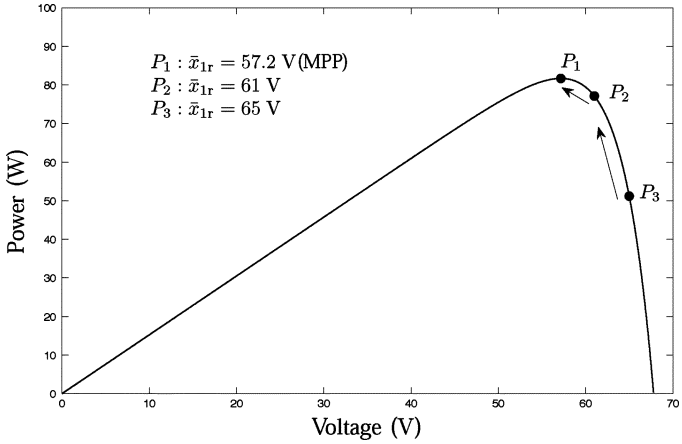

Fig. 10. Experimental Test 1.

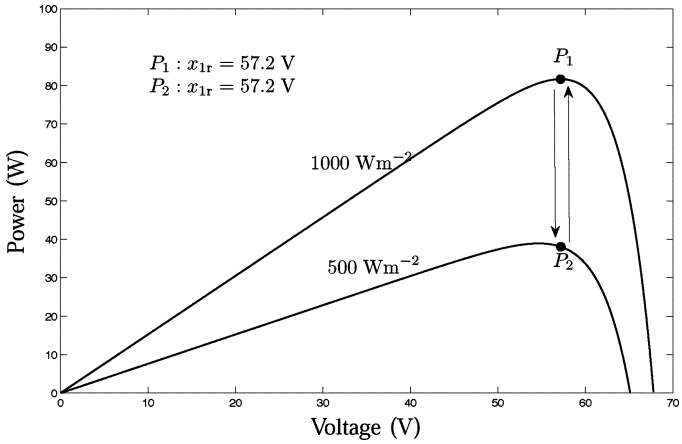

Fig. 11. Experimental Test 2.

generate the error signals, $\tilde{x}_1$ and $\tilde{x}_2$, and the derivative of x_2 allowing a wider dynamic range than in most digital systems. The rest of the controller was implemented in a hardwired circuit, more specifically, a Xilinx Spartan three field-programmable gate array (FPGA). A hardwired programmable device is normally more economical and faster than the equivalent microcontroller or DSP.[3] The output signals of the analog module are then quantized by means of ADC converters (ADC AD9525 of 12 bits and 25 MSPS). The quantized signals are then inputted to a digital processing stage implemented in a hardwired device, namely a Xilinx Spartan 3 FPGA. The hardwired algorithms implemented in the FPGA operates synchronously with a clock

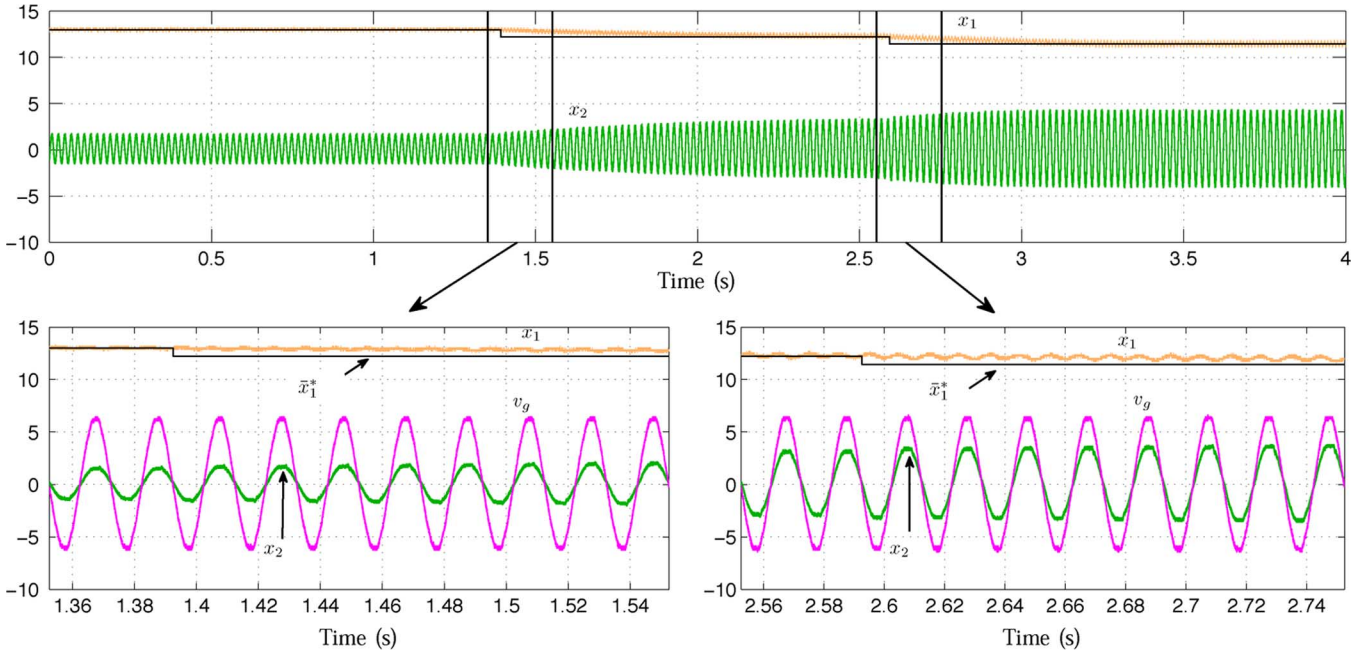

Fig. 12. Experimental Test 1. x_1, $\bar{x}_1^*$ and v_g at 5 V/div; x_2 at 1 A/div.

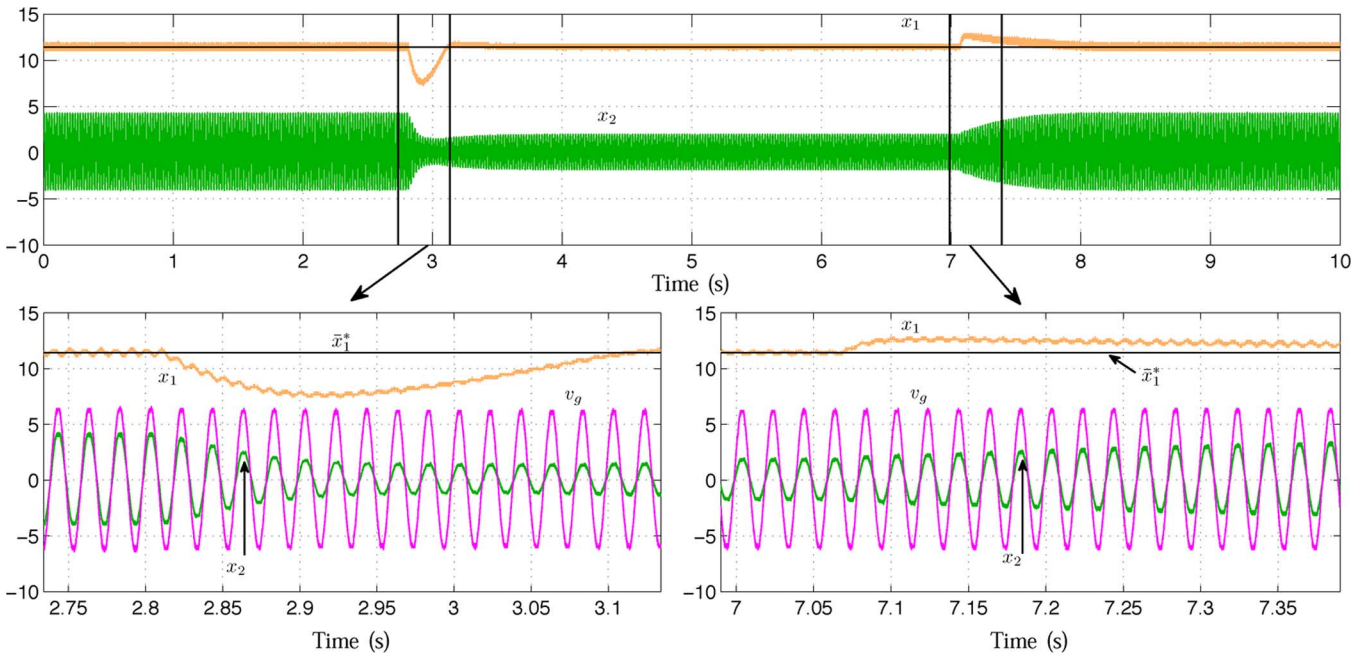

Fig. 13. Experimental Test 2. x_1, $\bar{x}_1^*$ and v_g at 5 V/div; x_2 at 1 A/div.

period of 4 ns. Additionally, the digital PWM that generates the signals δ and $\overline{\delta}$ is implemented within the FPGA using a sawtooth carrier waveform with a period of 40.96 μs. Fig. 8 shows a block diagram of the experimental setup implemented, notice that as discussed in the previous section in order to simplify the controller $\bar{x}_{1r}$ is used instead of x_{1r}. Signal $\bar{x}_{1r}$ is assumed to be given by an external MPPT. Fig. 9 shows the functions implemented in the FPGA. The following two different experimental tests were performed.

T1) *Experimental Test 1:* This experimental test deals with the regulation of $\bar{x}_1$. The T_g-averaged reference value of the PV voltage, $\bar{x}_{1r}$, is changed from 65 to 61 V and finally arriving to the PV array maximum power point value (57.2 V), as it is graphically shown in Fig. 10. The reference value transitions were programmed to occur every 60 grid cycles, i.e., 1.2 s.

T2) *Experimental Test 2:* This test was designed to show the adequate behavior of the closed-loop GPV inverter when abrupt changes in the electrical characteristics of the solar array simulator occur, emulating sudden irradiance changes in the PV array. The solar array simulator has been programmed with two set of electrical

characteristics, one corresponding to an irradiance of 1000 Wm^{-2} and another corresponding to an irradiance of 500 Wm^{-2}. The experimental test consisted in the sudden change of the 1000 Wm^{-2} electrical characteristics set to the 500 Wm^{-2} and then restoring the 1000 Wm^{-2} electrical characteristics set after a given time. This operation is shown in Fig. 11. This test is equivalent to an improvable worst case scenario and therefore it is a good way to validate the robustness of the designed controller.

The values of the tunable parameters of the controller, i.e., gains K and γ, have been defined mainly to avoid numerical problems (e.g., saturation of the signals, quantization problems). Therefore the gain K has been chosen as large as possible but avoiding saturation of signal u. The adaptive gain γ has been chosen such that a smooth non-oscillating x_1 dynamics is obtained. The final values of gains used were $K = 2.4$ and $\gamma = 0.05$.

Figs. 12 and 13 show the results of the aforementioned experimental tests. In the case of Experimental Test 1 (see Fig. 12) it can be seen that the output current is always in phase with the grid voltage and that the capacitor voltage eventually reaches its desired steady-state value. The controller parameters have been intentionally set such that a smooth closed-loop voltage dynamics is obtained in order to avoid the introduction of unwanted harmonics in the output current, i.e., in single-phase PV power inverters the effects of the voltage dynamics directly affects the output current.

Fig. 13 shows the electrical behavior of the full-bridge inverter prototype with the designed control scheme for Experimental Test 2. Notice that when the abrupt step-down irradiance change occurs ($t = 2.8$ s), after a settling time approximately equal to 0.3 s, the system is able to reach the desired steady state. A similar settling time is obtained when the step-up irradiance change occurs ($t = 7.05$ s). Note that during the complete experimental test the current injected to the utility grid is always in phase with the grid voltage. It should be remarked that the difference in the response of x_2 during the step-down and step-up irradiance change is due to the nonlinear behavior of the system. The nonlinear behavior becomes more apparent in the presence of large set-point changes, disturbances, or errors that cause the system to deviate from its nominal point of operation.

VI. Conclusion

A novel approach to the controller design for single-phase single-stage grid-connected power inverters is presented. Instead of linearizing the system, the control design approach aims to derive a global asymptotically stable closed-loop system that takes into account the nonlinear time-varying characteristics of the system. The robustness of the controller has been improved by adding an adaptive control law. A further theoretical analysis of the closed-loop system supported by means of numerical simulations allows to simplify the implementation of the controller. A laboratory prototype was built in order to test the closed-loop performance of the controlled system. The experimental test performed consisted of an abrupt change of the PV array irradiance. Even though such sudden and large change is not likely to occur in reality, it serves to underscore the robustness and effectiveness of the proposed controller. The experimental results showed that the implemented controller was able to meet the desired control requirements, i.e., to extract a given amount of power from the PV array (solar array simulator, in the case of the experimental prototype) and to inject to the utility grid a current in phase with the grid voltage even under extreme changes in the system parameters.

The results of this paper should be considered as a proof of principle. It is expected that the proposed controller provides a similar performance as those obtained using standard linear controller design techniques. Moreover, the inclusion of the nonlinear characteristics guarantees the closed-loop system to operate robustly and reliable, even in the presence of large set-point changes, disturbances, or errors that cause the system to deviate from its nominal point of operation. It is our believe that further research in the design and analysis of PV power systems considering and respecting their nonlinear nature may help to obtain more efficient and reliable management and control algorithms than the ones currently available.

References

[1] G. Petrone, G. Spagnuolo, R. Teodorescu, M. Veerachary, and M. Vitelli, "Reliability issues in photovoltaic power processing systems," *IEEE Trans. Ind. Electron.*, vol. 55, no. 7, pp. 2569–2580, Jul. 2008.

[2] D. Zmood and D. Holmes, "Stationary frame current regulation of PWM inverters with zero steady-state error," *IEEE Trans. Power Electron.*, vol. 18, no. 3, pp. 814–822, May 2003.

[3] R. Teodorescu, F. Blaabjerg, M. Liserre, and P. C. Loh, "Proportional-resonant controllers and filters for grid-connected voltage-source converters," *IEE Trans. Power Appl.*, vol. 153, no. 5, pp. 750–762, Sep. 2006, 2006.

[4] F. Blaabjerg, R. Teodorescu, M. Liserre, and A. V. Timubs, "Overview of control and grid synchronization for distributed power generation systems," *IEEE Trans. Ind. Electron.*, vol. 53, no. 5, pp. 1398–1409, Oct. 2006.

[5] M. Ciobotaru, R. Teodorescu, and F. Blaabjerg, "Control of single-stage single-phase pv inverter," in *Proc. Eur. Conf. Power Electron. Appl.*, 2005, pp. 1–10.

[6] C. Hua, J. Lin, and C. Shen, "Implementation of a dsp-controlled photovoltaic system with peak power tracking," *IEEE Trans. Ind. Electron.*, vol. 45, no. 1, pp. 99–107, Feb. 1998.

[7] M. Veerachary, T. Senjyu, and K. Uezato, "Voltage-based maximum power point tracking control of PV system," *IEEE Trans. Aerosp. Electron. Syst.*, vol. 38, no. 1, pp. 262–270, Jan. 2002.

[8] N. Femia, G. Petrone, G. Spagnuolo, and M. Vitelli, "Optimization of perturb and observe maximum power point tracking method," *IEEE Trans. Power Electron.*, vol. 20, no. 4, pp. 963–973, Jul. 2005.

[9] R. Teodorescu, F. Blaabjerg, U. Borup, and M. Liserre, "A new control structure for grid-connected LCL PV inverters with zero steady-state error and selective harmonic compensation," in *Proc. Appl. Power Electron. Conf. Expo.*, 2004, pp. 580–586.

[10] C.-Y. Chan, "A nonlinear control for DC-DC power converters," *IEEE Trans. Power Electron.*, vol. 22, no. 1, pp. 216–222, Jan. 2007.

[11] M. M. J. de Vries, M. J. Kransse, M. Liserre, V. G. Monopoli, and J. M. A. Scherpen, "Passivity-based harmonic control through series/parallel damping of an h-bridge rectifier," in *Proc. Int. Symp. Ind. Electron.*, 2007, pp. 3385–3390.

[12] D. Jeltsema and J. M. A. Scherpen, "A power-based perspective in modeling and control of switched power converters [past and present]," *IEEE Ind. Electron. Mag.*, vol. 1, no. 1, pp. 7–54, May 2007.

[13] A. Gensior, H. Sira-Ramirez, J. Rudolph, and H. Guldner, "On some nonlinear current controllers for three-phase boost rectifiers," *IEEE Trans. Ind. Electron.*, vol. 56, no. 2, pp. 360–370, Feb. 2009.

[14] S. Sanders and G. Verghese, "Lyapunov-based control for switched power converters," *IEEE Trans. Power Electron.*, vol. 7, no. 1, pp. 17–24, Jan. 1992.

[15] R. Leyva, A. Cid-Pastor, C. Alonso, I. Queinnec, S. Tarbouriech, and L. Martinez-Salamero, "Passivity-based integral control of a boost converter for large-signal stability," *IEE Proc. Control Theor. Appl.*, vol. 153, no. 2, pp. 139–146, 2006.

[16] H. Komurcugil and O. Kukrer, "A new control strategy for single-phase shunt active power filters using a lyapunov function," *IEEE Trans. Ind. Electron.*, vol. 53, no. 1, pp. 305–312, Feb. 2006.

[17] C. Meza, D. Jeltsema, D. Biel, and J. M. A. Scherpen, "Passive p-control for grid-connected PV systems," in *Proc. 17th IFAC World Congr.*, 2008, pp. 5575–5580.

[18] G. Escobar, A. Stankovic, P. Mattavelli, F. Gordillo, and J. Aracil, "From adaptive PBC to PI nested control for SATCOM," in *Proc. IFAC Workshop Digit. Control*, 2000, pp. 459–464.

[19] G. Escobar, D. Chevreau, R. Ortega, and E. Mendes, "An adaptive passivity-based controller for a unity power factor rectifier," *IEEE Trans. Control Syst. Technol.*, vol. 9, no. 4, pp. 637–644, Jul. 2001.

[20] M. Calais, J. Myrzik, T. Spooner, and V. Agelidis, "Inverter for single-phase grid connected photovoltaic systems—an overview," in *Proc. Power Electron. Specialists Conf.*, Feb. 2002, vol. 4, pp. 1995–2000.

[21] S. B. Kjaer, J. K. Pedersen, and F. Blaabjerg, "A review of single-phase grid-connected inverters for photovoltaic modules," *IEEE Trans. Ind. Appl.*, vol. 41, no. 5, pp. 1292–1306, Sep./Oct. 2005.

[22] M. Meinhardt, "Past, present and future of grid connected photovoltaic and hybrid power systems," in *Proc. Power Eng. Soc. Summer Meet.*, Jul. 2000, vol. 2, pp. 1283–1288.

[23] S. Chiang, K. Chang, and Y. Yen, "Residential photovoltaic energy storage system," *IEEE Trans. Ind. Electron.*, vol. 45, no. 3, pp. 385–394, Jun 1998.

[24] D. Cruz-Martins and R. Demonti, "Photovoltaic energy processing for utility connected system," in *Proc. 27th Annu. Conf. IEEE Ind. Electron. Soc.*, 2001, pp. 1292–1296.

[25] S. Busquets-Monge, J. Rocabert, P. Rodriguez, S. Alepuz, and J. Bordonau, "Multilevel diode-clamped converter for photovoltaic generators with independent voltage control of each solar array," *IEEE Trans. Ind. Electron.*, vol. 55, no. 7, pp. 2713–2723, Jul. 2008.

[26] C. Meza, J. Negroni, D. Biel, and F. Guinjoan, "Inverter configuration comparative for residential pv-grid connected systems," in *Proc. Int. Conf. Ind. Electron. IEEE*, Nov. 2006, pp. 4361–4366.

[27] J. A. Gow and C. D. Manning, "Development of a photovoltaic array model for use in power-electronics simulation studies," *IEE Proceedings—Electr. Power Appl.*, vol. 146, no. 2, pp. 193–200, Mar. 1999.

[28] S. Liu and R. Dougal, "Dynamic multi-physics model for solar array," *IEEE Trans. Ind. Electron.*, vol. 17, no. 2, pp. 285–294, Jun. 2002.

[29] U. Boke, "A simple model of photovoltaic module electric characteristics," in *Proc. Eur. Conf. Power Electron. Appl.*, Sep. 2007, pp. 1–8.

[30] R. Leyva, C. Alonso, I. Queinnec, A. Cid-Pastor, D. Lagrange, and L. Martinez-Salamero, "MPPT of photovoltaic systems using extremum - seeking control," *IEEE Trans. Aerosp. Electron. Syst.*, vol. 42, no. 1, pp. 249–258, Jan. 2006.

[31] S. Jain and V. Agarwal, "Comparison of the performance of maximum power point tracking schemes applied to single-stage grid-connected photovoltaic systems," *IET Electr. Power Appl.*, vol. 1, no. 5, pp. 753–762, Sep. 2007.